Cryogenic hyperspectroscopy of nanoemitters and atomically thin semiconductors

Andre Neumann

München 2017

Cryogenic hyperspectroscopy of nanoemitters and atomically thin semiconductors

Dissertation
an der Fakultät für Physik
der Ludwig-Maximilians-Universität
München

vorgelegt von
Andre Neumann
aus Moskau, Russland

München, den 29. Juni 2017

Erstgutachter: Prof. Dr. Alexander Högele
Zweitgutachter: Prof. Dr. Thomas Weitz
Tag der mündlichen Prüfung: 27. Juli 2017

Zusammenfassung

Eine der modernsten Entwicklungen auf dem Gebiet der Festkörperphysik befasst sich mit der Herstellung elektronischer und optischer Hochleistungskomponenten auf Grundlage atomar dünner zweidimensionaler Materialien. Zu dieser Gruppe der Dünnschichtmaterialien gehören neben Graphen die Übergangsmetalldichalkogenide, die im Grenzfall einer Monolage Halbleiter mit direkter Bandlücke repräsentieren. Sie zeigen starke Licht-Materie-Wechselwirkung und weisen Elektronen mit gekoppelten Spin- und Valley-Quantenfreiheitsgraden auf, wobei sich der Begriff Valley auf energieentartete Bandextrema an den inequivalenten Randpunkten K und K' des reziproken Gitters bezieht. Diese Eigenschaften sind Kernbestandteile neuartiger opto-valleytronischer Technologien, welche auf der Grundlage valleyspezifischer optischer Anregungen die Kontrolle von Strömen topologischer Elektronen oder Exzitonen erlauben. Der Erfolg derartiger Konzepte, basierend auf der optischen Erzeugung von Valley-Polarisation oder Valley-Kohärenz, wird dabei entscheidend von der Materialqualität bestimmt.

Im Rahmen dieser Arbeit wurde die Valley-Pseudospin-Optik von monolagigem Molybdändisulfid stellvertretend für die Klasse der Übergangsmetalldichalkogenide mit Tieftemperatur-Spektropolarimetrie untersucht. Im Ergebnis wurde eine neue Technik zur zweidimensionalen polarimetrischen Bildgebung und Visualisierung von Valley-Polarisations- und Valley-Kohärenzprofilen in lateral ausgedehnten, durch chemische Gasphasenabscheidung hergestellten, monolagigen Kristallen entwickelt. Die erarbeitete hyperspektrale Konfokal- und Weitfeldpolarimetrie ermöglichte direkten Zugang zur Identifizierung und Untersuchung unordnungsinduzierter Valley-Dekohärenz an unterschiedlichen Klassen von Kristalldefekten wie Kanten, Korngrenzen oder Oberflächenverunreinigungen. Die Skalierbarkeit dieser Technik auf makroskopische Dimensionen bietet innovative Möglichkeiten für die schnelle Analyse opto-elektronischer Komponenten in Wafergröße. Darüber hinaus wurde die Bildgebung im externen magnetischen Feld für quantitative Untersuchungen optischer Valley-Orientierung und Valley-Depolarisation eingesetzt. Die experimentellen Methoden wurden zusätzlich zur Analyse lokaler Ladungsvariationen von monolagigen Systemen in unkontrollierten elektrostatischen Umgebungen verwendet.

Der zweite Teil der Arbeit konzentrierte sich auf nanoskalige Quantenemitter in Form von fluoreszierenden Nanodiamanten, Halbleiter-Nanokristallen und einzelnen Farbstoffmolekülen. Blinkende Fluoreszenz und spektrale Diffusion sind nachteilige und häufig auftretende Eigenschaften vieler solcher Quantenemitter in unkontrollierten Systemen. Das Einbetten von Nanoemittern in Polymermatrizen wie Polymethylmethacrylat bietet eine einfache und oft verwendete Methode zur Entfernung naher Ladungsfallen, welche optische Emission nachteilig beeinflussen. Gleichzeitig

dient dieses Verfahren der Verhinderung von Aggregation der Nanoemitter. Im Falle einer optischen Kontamination der Polymermatrizen konkurriert deren Emission jedoch mit der Fluoreszenz von Nanoemittern mit geringer Quantenausbeute. Die umfangreichen spektroskopischen Studien dieser Arbeit identifizierten lösungsmittelspezifische organische Fluorophore als Hauptquelle optischer Kontamination in Polymeren, welche andererseits als stabile nichtklassische Lichtquellen durch einfache Fabrikation zur Anwendung gebracht werden können.

Abstract

The past few years have witnessed the emergence of a new paradigm in condensed matter physics that aims to build high performance electronic and optical devices using atomically thin two-dimensional materials. Alongside graphene, layered materials include the class of transition metal dichalcogenides, which represent direct band gap semiconductors if thinned down to a single layer. They exhibit strong light-matter interaction and host electrons with coupled spin and valley quantum degrees of freedom as key ingredients for novel opto-valleytronic technologies, where valley selective optical excitations facilitate control of topological electron or exciton currents. The successful implementation of concepts featuring such functionalities will crucially rely on the material quality to support the optical generation of valley polarization or valley coherence.

In the framework of this thesis, valley pseudospin optics of monolayer molybdenum disulfide, as a representative transition metal dichalcogenide, have been explored using cryogenic spectropolarimetry. To this end, a novel technique of two-dimensional polarimetric imaging was pioneered to visualize landscapes of valley polarization and valley coherence in extended monolayer crystals grown by chemical vapor deposition. The developed hyperspectral confocal and wide-field polarimetry provided direct capabilities to identify and inspect disorder-induced valley decoherence at various classes of crystal defects such as edges, grain boundaries, or surface contaminants. The scalability of the technique to macroscopic lengths provides an innovative means for rapid inspection of wafer-sized opto-valleytronic devices. Moreover, image analysis in the presence of external magnetic fields was used for quantitative studies of optical valley orientation and valley depolarization. The hyperspectral methods were additionally applied to probe local charge variations of monolayer systems in uncontrolled electrostatic surroundings.

The second part of this thesis focused on nanoscale quantum emitters in the form of fluorescent nanodiamonds, semiconductor nanocrystals, and single dye molecules. Fluorescence intermittency and spectral diffusion are detrimental features common to many quantum emitters with an uncontrolled environment. Embedding the nanoemitters in polymer matrices such as polymethylmethacrylate is a simple and often used approach to remove proximal charge trapping sites which inhibit optical emission, and at the same time to prevent aggregation. However, the possible occurrence of light emission by contaminants in polymer matrices can compete with the fluorescence of nanoemitters with low quantum yields. The comprehensive spectroscopic studies of this thesis identified solvent-specific organic fluorophores as the main source of optical contamination in polymers, which on the other hand proved to be simple and reliable quantum light sources.

Contents

List of publications

A full list of publications by the author is provided below. Publications related to this dissertation are labeled P1–P3.

[P1] **A. Neumann***, J. Lindlau*, and A. Högele. *Contamination of polymethylmethacrylate by organic quantum emitters*. ArXiv e-prints (2017). arXiv:1706.08341.

* These authors contributed equally to this work.

[P2] **A. Neumann**, J. Lindlau, L. Colombier, M. Nutz, S. Najmaei, J. Lou, A. D. Mohite, H. Yamaguchi, and A. Högele. *Opto-valleytronic imaging of atomically thin semiconductors*. Nat. Nanotechnol. **12**, 329–334 (2017).

[P3] T. Zhang, **A. Neumann**, J. Lindlau, Y. Wu, G. Pramanik, B. Naydenov, F. Jelezko, F. Schüder, S. Huber, M. Huber, F. Stehr, A. Högele, T. Weil, and T. Liedl. *DNA-Based Self-Assembly of Fluorescent Nanodiamonds*. J. Am. Chem. Soc. **137**, 9776–9779 (2015).

[P4] A. Laucht, N. Hauke, **A. Neumann**, T. Günthner, F. Hofbauer, A. Mohtashami, K. Müller, G. Böhm, M. Bichler, M.-C. Amann, M. Kaniber, and J. J. Finley. *Nonresonant feeding of photonic crystal nanocavity modes by quantum dots*. J. Appl. Phys. **109**, 102404 (2011).

[P5] U. Hohenester, A. Laucht, M. Kaniber, N. Hauke, **A. Neumann**, A. Mohtashami, M. Seliger, M. Bichler, and J. J. Finley. *Phonon-assisted transitions from quantum dot excitons to cavity photons*. Phys. Rev. B **80**, 201311 (2009).

[P6] M. Kaniber, **A. Neumann**, A. Laucht, M. F. Huck, M. Bichler, M.-C. Amann, and J. J. Finley. *Efficient and selective cavity-resonant excitation for single photon generation*. New J. Phys. **11**, 013031 (2009).

[P7] M. Kaniber, A. Laucht, **A. Neumann**, M. Bichler, M.-C. Amann, and J. J. Finley. *Tunable single quantum dot nanocavities for cavity QED experiments*. J. Phys. Condens. Matter **20**, 454209 (2008).

[P8] M. Kaniber, A. Laucht, **A. Neumann**, J. M. Villas-Bôas, M. Bichler, M.-C. Amann, and J. J. Finley. *Investigation of the nonresonant dot-cavity coupling in two-dimensional photonic crystal nanocavities*. Phys. Rev. B **77**, 161303 (2008).

List of abbreviations

AFM	atomic force microscopy
APD	avalanche photodiode
CCD	charge-coupled device
CVD	chemical vapor deposition
CW	continuous-wave
FL	fluorescence
FND	fluorescent nanodiamond
FWHM	full-width at half-maximum
NA	numerical aperture
NV	nitrogen-vacancy
OPO	optical parametric oscillator
PL	photoluminescence
PMMA	polymethylmethacrylate
QD	quantum dot
TMD	transition metal dichalcogenide
ZPL	zero-phonon line

Chapter 1

Introduction

Visual perception, combined with cognitive image interpretation, provides insight into the most fundamental aspects of nature. Complementary information about the state of matter can be retrieved from its interaction with the primary degrees of freedom of light such as intensity, wavelength, or polarization. The combined measurement of all three properties has been successfully applied for structural diagnostics of matter across disciplines as diverse as medicine and astronomy [1]. In condensed matter physics, complete and detailed analysis of light often provides valuable data to the advancement of novel materials with unconventional opto-electronic properties. In turn, the photonic materials contribute innovative functionalities to tailored architectures and future optical devices. It is with this ambition and motivation, that this thesis explores low-dimensional photonic systems by means of fluorescence (FL) and photoluminescence (PL) spectroscopy, as well as innovative imaging methods. Hereby, the emphasis is given to two specific topics and materials.

The main part of this work is directed towards atomically thin two-dimensional materials. Largely fueled by the seminal success story of graphene [2, 3], experiments on other chemically stable single-layer crystals revealed a plethora of properties and exciting prospects [4, 5]. These include the promising future direction to stack individual monolayers in a deterministic sequence into vertical structures, known as van der Waals heterostructures, for technologies beyond conventional opto-electronics [6, 7]. Among the most notable examples of the elementary units of such artificial structures are the insulating hexagonal boron nitride [8] and the class of transition metal dichalcogenides (TMDs), which includes MoS_2, WS_2, $MoSe_2$, WSe_2, and $MoTe_2$. In the form of a single layer, the latter group represents atomically thin direct band gap semiconductors as was first verified for MoS_2 [9, 10]. Similar to the original isolation of graphene [11], monolayer crystals can be obtained from their bulk counterparts by mechanical exfoliation. For scalable growth, atomic layers are

alternatively synthesized using chemical vapor deposition (CVD) or molecular beam epitaxy [12–14].

Due to the truly two-dimensional geometry, Coulomb interactions between photogenerated charge carriers play a dominant role in the optical response of TMD monolayers. These interactions call forth the formation of robust excitons [15–19] and more exotic quasi-particles, for instance trions [20, 21], biexcitons [22, 23], and Fermi polarons [24]. Furthermore, for a thickness of less than a nanometer the light-matter coupling in the semiconducting materials is remarkably strong with resonant excitonic absorption as large as 10–20% [10]. As a further unique aspect, monolayer TMDs host charge carriers with optically accessible and interlocked spin and valley pseudospin degrees of freedom, which can be used to encode or process quantum information [25, 26]. This opens the promising avenue to coupled opto-spintronics and opto-valleytronics based on polarized photons interacting with spin and valley-polarized electron-hole pairs. The observation of the valley Hall effect in monolayer MoS_2 is one example of such functionalities, where optical polarization is converted to electrical information [27]. The reciprocal concept, where electrical information is transformed into optical polarization, has also been demonstrated in the form of chiral light emitting diodes [28, 29].

In both cases, the efficiency of the conversion processes is to a large extent determined by the crystal quality. Utilizing this sensitivity, the novel two-dimensional polarimetry pioneered in this work was used to identify disorder-induced valley decoherence at various classes of crystal defects such as edges, grain boundaries or surface contaminants. This imaging technique furthermore provides a direct means for opto-valleytronic inspection of macroscopic devices on microscopic scales. In addition, the reported experiments visualize exciton and trion specific profiles for imaging of charge doping in extended monolayer crystals.

The other part of this thesis addresses zero-dimensional nanomaterials on dielectric substrates as well as in polymer matrices consisting of polymethylmethacrylate (PMMA). Nanosized emitters, such as molecules, color centers in nanocrystals, or semiconductor nanocolloids find wide application as basic photoactive elements in fields of research ranging from super-resolution imaging in biology [30] to solid-state based quantum information science and technology [31, 32]. Many of the related experiments and fundamental studies rely on the temporal and spectral stability of the individual emitters [33]. To ensure the desired stability, polymer matrices are often employed as inert environments to suppress emission intermittency and spectral diffusion as commonly encountered by nanoemitters [34, 35]. However, this generic experimental setting for basic studies with optical spectroscopy can be compromised by fluorescent organic contaminants residing either on the surface of ill-prepared dielectric supports or within the polymer matrix used to embed the nanoemitters

in question. The studies herein raise the awareness of possible misconceptions and erroneous assignments of spectral features to various classes of nanoemitters, and provide the framework for correct interpretation of related experiments in the future.

1.1 Outline of the thesis

The presentation of the main experimental results achieved within this thesis is based on manuscripts that are either published or in preparation for publication. The organization of the thesis can be found in the brief outline below.

Chapter 1 This current chapter provides an introduction to the thesis.

Chapter 2 This chapter describes the experimental setup used for the confocal measurements of this thesis. As examples, optical properties of two different types of nanoemitters are characterized using this instrumentation.

Chapter 3 The focus of this chapter is directed towards spectroscopic studies of optical contamination in polymer matrices and dielectric substrates. Both the origin of the contaminants and their emission properties are discussed.

Chapter 4 Theoretical aspects of atomically thin transition metal dichalcogenides, with the emphasis set on their spin and valley physics, are presented in this chapter.

Chapter 5 Spectropolarimetric imaging is introduced as a method to reveal crystal quality and opto-valleytronic properties of two-dimensional transition metal dichalcogenides such as molybdenum disulfide monolayers. The results presented in this chapter include spatially, spectrally, and polarization-resolved photoluminescence measurements at cryogenic temperatures and high magnetic fields.

Chapter 6 The cryogenic photophysics of electrostatically tunable and a chemically doped molybdenum disulfide monolayers are discussed in this chapter. Two-dimensional hyperspectroscopy is employed to construct exciton and trion profiles, and to compute charge doping images.

Chapter 7 This last chapter summarizes the main findings of the thesis and provides perspectives for possible future research.

Chapter 2

Confocal hyperspectroscopy of nanoemitters

This chapter introduces confocal hyperspectroscopy as a method for optical characterization of nanoemitters. To begin with, the confocal microscope used for the experimental studies of this thesis is briefly discussed. On the basis of this setup, the photophysics of two different nanosized structures are addressed. As one of the presented examples, self-assembled dimers of fluorescent nanodiamonds anchored to DNA origami are visualized by means of confocal imaging at ambient conditions. Next, optical properties of semiconductor nanocolloids are studied using cryogenic spectroscopy.

2.1 Microscope for confocal hyperspectroscopy

A home-built confocal microscope coupled to single-mode fibers as illustrated in Fig. 2.1a formed the basis for hyperspectroscopic and spectropolarimetric experiments of this thesis. The microscope was operated either at room temperature or, for cryogenic experiments, in a closed-cycle cryostat[1] equipped with a superconducting magnet with fields up to ±9 T and a base temperature of 3.1 K. Critical parts of the setup were mounted in a home-built titanium module as shown in Fig. 2.1b to ensure long-term stability even at high magnetic fields.

Stepping x, y, z nanopositioners[2] and an x, y piezo-scanner[3] provided spatial positioning of the samples in the focal plane of an apochromatic objective with diffraction-limited confocal excitation and detection spots. Unless stated otherwise, the slip-stick motion of the nanopositioners was used for confocal raster-scan imaging. Cryogenic measurements were mainly performed using a low-temperature apochromat[4] with a numerical aperture (NA) of 0.65 and a full-width at half-maximum (FWHM) spot diameter of 0.7 µm. Room-temperature experiments on the other hand were conducted with higher NA objectives with spot diameters of less than 0.4 µm. Continuous-wave (CW) or pulsed laser[5] illumination from a single-mode fiber was fed into the microscope via Fresnel reflection from a plate beam splitter, a second cross-aligned beam splitter secured an unmodified polarization of the luminescence in the detection path. A set of optional linear polarizers[6], half- and quarter-waveplates[7] mounted on piezo-rotators[8] was used to control and analyze the photon polarization in excitation and emission. Spectral filtering was achieved with short-pass, long-pass, and tunable band-pass filters[9]. Moreover, in some cases the cross-aligned beam splitters were replaced by dichroic mirrors[10] to increase the excitation power.

For hyperspectroscopic studies, luminescence from the sample was dispersed in a standard grating spectrometer[11] and detected with a nitrogen-cooled silicon charge-coupled device (CCD) camera[12]. Alternatively, fiber-coupled luminescence was de-

[1] attocube systems, attoDRY1000
[2] attocube systems, ANP101 series
[3] attocube systems, ANSxy100lr
[4] attocube systems, LT-APO/VIS/0.65
[5] Information on laser systems is provided at the according experimental sections.
[6] Thorlabs, LPVIS and LPVISB series
[7] B. Halle, RAC 3 series
[8] attocube systems, ANR240/RES
[9] Semrock, RazorEdge and VersaChrome series
[10] Semrock, BrightLine series
[11] PI, Acton SP-2558
[12] PI, Spec-10:100BR/LN operated with gain setting of 4 e^-/count

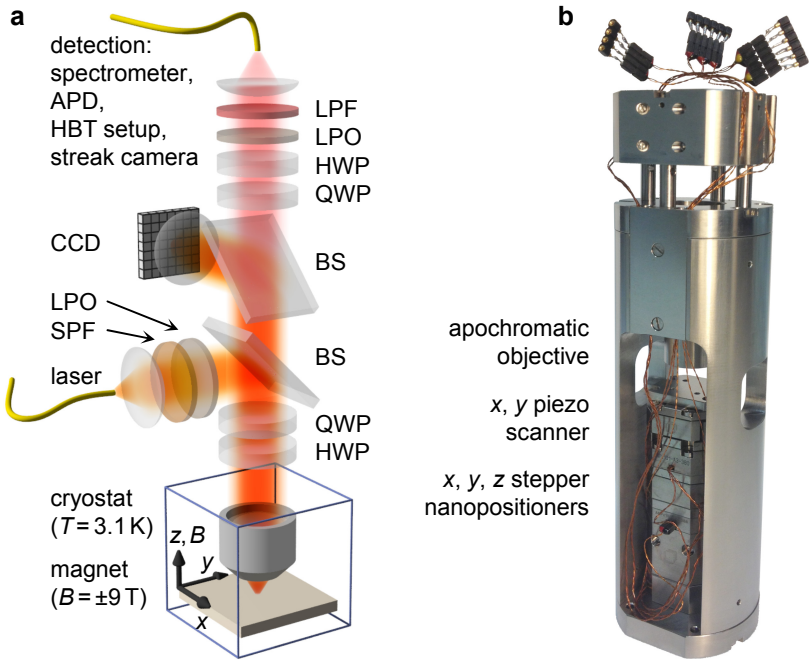

Figure 2.1: a, Schematic of the confocal setup used for hyperspectral and spectropolarimetric experiments at cryogenic temperatures or high magnetic fields. Laser excitation was fed into the microscope through a single-mode fiber, which after passing through a short-pass filter (SPF) and a linear polarizer (LPO), was reflected off a plate beam splitter (BS) and guided towards the sample. An arbitrary excitation polarization was defined using the combination of achromatic quarter- and half-waveplates (QWP and HWP). The sample was mounted on a set of nanopositioning units below a focusing apochromatic objective in a rigid titanium housing as shown in **b**. This entity was optionally cooled down to 3.1 K in a closed-cycle cryostat, which was equipped with a superconducting magnet capable of fields up to ±9 T along the light propagation axis. The luminescence from the sample was collected by the microscope objective and transmitted through two cross-aligned BSs for unaltered polarization analysis by the optional upper QWP, HWP, and LPO, which also corrected the polarization modifications by the lower HWP and QWP. A long-pass filter (LPF) was used to eliminate reflected laser light from the luminescence signal, which was coupled into a single-mode fiber. The laser light, reflected off the upper BS and focused onto a charge-coupled device (CCD), was used for sample orientation. The measurement systems used for detection of the luminescence were either a grating spectrometer, an avalanche photodiode (APD), an APD-based Hanbury Brown and Twiss (HBT) setup, or a streak camera.

tected with a single-photon counting avalanche photodiode[13] (APD). To test single-photon sources two identical APDs were employed in a Hanbury Brown and Twiss arrangement. A streak camera[14] was used for lifetime measurements with high temporal resolution.

[13]PicoQuant, τ-SPAD with dark count rate of 35 cts/s
[14]Hamamatsu, C5680-24S

2.2 Optical characterization of fluorescent nanodiamond dimers

This section is adapted with permission from Ref. P3:
T. Zhang, A. Neumann, J. Lindlau, Y. Wu, G. Pramanik, B. Naydenov, F. Jelezko, F. Schüder, S. Huber, M. Huber, F. Stehr, A. Högele, T. Weil, and T. Liedl. *DNA-Based Self-Assembly of Fluorescent Nanodiamonds*. J. Am. Chem. Soc. **137**, 9776–9779 (2015).
Copyright 2015 American Chemical Society.

In the following we address the room temperature confocal FL of fluorescent nanodiamond (FND) dimer architectures containing optical defects in the form of nitrogen-vacancy (NV) centers. As nanosized chemically robust crystals, FNDs constitute a class of fluorescent markers suitable for a wide range of biocompatible applications including thermometry [36], or imaging and tracking [37]. The further development of these applications and novel photonic functionalities relies on the precise spatial organization of FNDs. For this purpose, DNA-based nanostructuring [38] provides a powerful method for the deterministic bottom-up assembly of such functional structures.

Two representative examples of the optically studied FND dimer structures are shown in the transmission electron micrographs of Fig. 2.2a and b. The dimers were self-assembled with nanometer precision on functionalized DNA origami helix bundles[15]. A color-coded FL intensity map of spatially dispersed FND dimer nanostructures on quartz is shown in Fig. 2.2c. The map was recorded with diffraction-limited confocal laser[16] excitation at 532 nm and collection above 575 nm by raster-scanning the sample with respect to the focal spot[17] with a FWHM diameter of $\sim$ 370 nm. Several FND dimer assemblies appear as pairs of FL hotspots in the map. Other assemblies are not clearly resolvable or represent single-labeled DNA origamis. Fig. 2.2d and e depicts two high-resolution maps of FND dimers exhibiting a separation of 451 and 406 nm, which is well within the limits of an expected maximum center-to-center distance of $\sim$ 476 nm, given by the sum of the length of the origami helix bundle of 428 nm and the average diameter of a functionalized FND of 48 nm. Fig. 2.2f shows a typical spectrum of a FND assembled on DNA origami (red trace). It exhibits spectral characteristics of negatively charged NV color centers in diamond with a noticeable zero-phonon line (ZPL) at $\sim$ 637 nm (labeled NV^-) accompanied by Stokes and anti-Stokes phonon sidebands. For comparison Fig. 2.2f also shows a typical spectrum of a bare FND (gray trace), which

[15] Details on sample preparation are given in the original publication P3.
[16] CNI, MLL-III-532-50-1
[17] Measured using an apochromat (Olympus, UMPlanFl 100x/0.90 BD) with NA of 0.90.

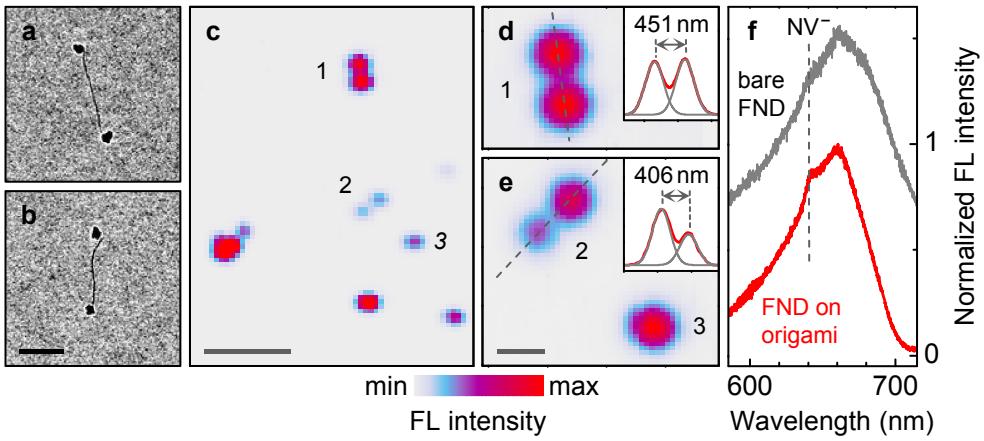

Figure 2.2: **a**, **b**, Transmission electron micrographs of two representative DNA origami-assembled fluorescent nanodiamond (FND) dimers; scale bar is 200 nm. **c**, Color-coded confocal fluorescence map of nanodiamond dimers, the assemblies appear as pairs or individual fluorescent hotspots; scale bar is 2 μm. **d**, **e**, Zoom-in on nanodiamond dimers (labeled 1, 2, and 3 in **c**) with corresponding line-scans fitted with two Gaussians; scale bar is 400 nm. **f**, Normalized fluorescence intensity of a nanodiamond assembled on DNA origami (red trace) and a typical bare nanodiamond (gray trace). The spectra were vertically offset for clarity to highlight the characteristics of negatively charged nitrogen-vacancy center fluorescence (NV^-). All fluorescence data were obtained at room temperature with laser excitation at 532 nm.

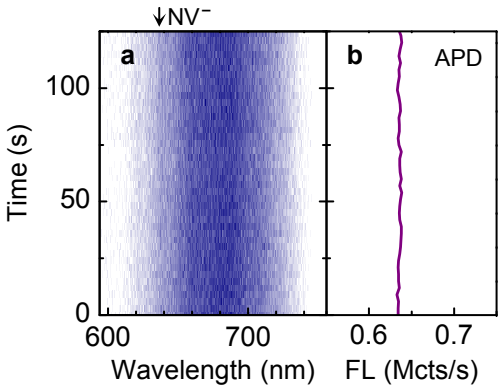

Figure 2.3: **a**, Temporal evolution of the fluorescence from a nanodiamond assembled on DNA origami. The time trace exhibited a pronounced NV^- zero-phonon line and showed no significant fluctuations in the fluorescence intensity or in the spectral profile. **b**, Consistently, the integrated fluorescence intensity of the same emission spot detected with an avalanche photodiode (APD) remained constant at ~ 0.64 Mcts/s over the course of measurement. All data were recorded at room temperature with excitation at 532 nm.

exhibits the same spectral features indicating that the FL properties of FNDs are robust against the DNA assembly procedures.

This is also reflected by the fact that the FNDs on DNA origami were photostable in time, as presented in Fig. 2.3a and b. For the course of measurement of over 100 s, we did not observe significant blinking, bleaching or spectral wandering of the DNA-modified FNDs. In contrast to our measurements, smaller FNDs with diameters in the range of 5 nm and single NV centers are known to exhibit FL intermittency in uncontrolled environments [34].

2.3 Optical characterization of semiconductor nanocolloids

The focus of this section is directed towards confocal PL studies of semiconductor nanocolloids as another type of nanosized emitter. Colloidal semiconductor quantum dots (QDs) feature opto-electronic properties that are a sensitive function of size, shape, and material composition [39, 40]. The potential of tailoring the color of optical transitions through the interplay of material-specific band gap and geometry-dependent quantum confinement renders colloidal QDs attractive for a wealth of applications, ranging from FL markers in biological systems [41] to photovoltaics [42]. Related research has been fueled even more by recent progress in the understanding of both intrinsic and extrinsic parameters that govern the optical quality of nanocrystal QDs.

In our studies we focused on two types of colloidal QD heterostructures[18] — core-shell CdTe-CdSe[19] and core-shell-shell CdSe-CdS-ZnS[20] QDs. Fig. 2.4 presents the spectral characteristics of the two materials for 532 nm CW laser[21] excitation. The spectrally-resolved PL of individual CdTe-CdSe QDs exhibited several excitonic bands with energy separations ranging from 17 to 21 meV in the main complex of four peaks (Fig. 2.4a), which is in good agreement with previous assignments to multiexcitonic transitions for comparable samples [43]. In contrast, single CdSe-CdS-ZnS showed only two dominant peaks separated by $\sim$ 27 meV (Fig. 2.4c). For CdSe-ZnS QDs, similar signatures were ascribed to the dark exciton and its redshifted longitudinal optical phonon replica [44].

Since Auger processes should be effectively suppressed in both material configurations with a slowly varying confinement potential [45], we expected to find photostability as a common feature. However, we observed that the majority of

[18]Samples were synthesized by the group of E. Lifshitz (Technion, Israel).
[19]CdTe core radius of 1.55 nm; alloyed CdTe-CdSe shell of 2 monolayers
[20]CdSe core radius of 2.20 nm; CdS (ZnS) shell of 2 (1–2) monolayers
[21]CNI, MLL-III-532-50-1

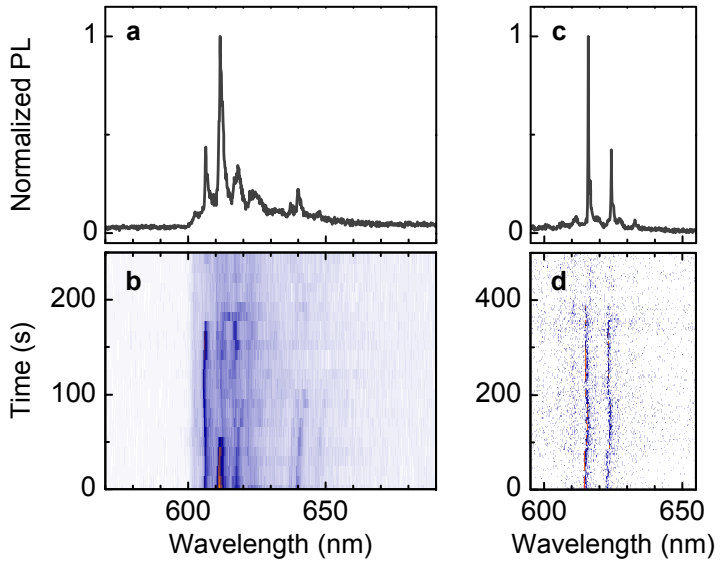

Figure 2.4: **a**, Normalized photoluminescence spectrum of a core-shell CdTe-CdSe colloidal quantum dot and **b**, corresponding color-coded temporal evolution. **c**, **d** Same but for a core-shell-shell CdSe-CdS-ZnS quantum dot. The semiconductor nanocolloids were deposited on quartz substrates and studied at a temperature of 3.1 K using laser excitation at 532 nm.

both CdTe-CdSe and CdSe-CdS-ZnS individual QDs deposited directly on quartz substrates exhibited photobleaching after tens to a few hundred of seconds of laser illumination (Fig. 2.4b and d). Moreover, spectral wandering was ubiquitous on seconds timescales for both samples. These observations confirm that the photophysics of nanocrystal QDs is not only a function of intrinsic parameters but strongly affected by extrinsic factors [46]. As such, the proximity of a charge fluctuating on the nanocrystal surface gives rise to spectral jitter and facilitates photoblinking with long luminescence off-times [47]. Significant separation between the surface charges and the exciton smoothly confined in the QD core should on the other hand recover the photostability as an intrinsic property and characteristic feature of giant-shell QDs [48]. Another convenient strategy to establish photostability for QD materials is to encapsulate them in a polymer matrix to ensure an electrostatically stable environment in analogy to electrochemical passivation [49].

Chapter 3

Quantum light from dielectric substrates covered with PMMA

This chapter is based on the manuscript P1:
A. Neumann, J. Lindlau, and A. Högele. *Contamination of polymethylmethacrylate by organic quantum emitters.* ArXiv e-prints (2017). arXiv:1706.08341.

Matrices of polymethylmethacrylate provide inert host environments to photoactive nanoscale emitters. By virtue of chemical and electrostatic stability, they reduce emission intermittency or photobleaching commonly encountered by nanoemitters at ambient conditions. However, low but finite photoactivity of the polymer matrix itself can compete with the fluorescence of individual nanoemitters and compromise the interpretation of spectroscopic data. The results of this chapter report that contamination of polymethylmethacrylate by organic fluorophores gives rise to optical activity in the visible spectral range with sizable intensity in fluorescent hotpots and quantum emission statistics.

3.1 Introduction and overview of the experiment

Embedding quantum emitters within chemically and electrostatically inert polymer matrices such as PMMA is a common approach to reduce the FL intermittency encountered by a broad class of photoactive nanoparticles [50, 51] and molecular dyes [52] under ambient conditions, thus promoting stable and enhanced FL [34, 35]. However, contamination of the polymer matrix by fluorescent constituents can result in controversial assignment of spectral features. In some spectroscopy experiments it has proven difficult to distinguish between the FL stemming from quantum emitters, the polymer matrix, or the supporting substrate [53, 54]. This is not surprising given the challenge of unambiguous assignment of the FL to its actual source for photoactive systems with low quantum yields, or individual quantum emitters with high quantum yields but inherently low absolute FL intensities.

In the visible spectral range, the realm of photoactive nanoemitters includes single molecules [55], fluorescent nanodiamonds [56], colloidal QDs [57] and nanoplatelets [58], TMD QDs [59–62], or perovskite nanoplatelets [63]. The range of related potential applications in light emitting, detecting, and harvesting devices is as diverse as the specific details of the photophysics of the underlying emitters. In absolute terms, however, and depending on the radiative lifetime, some of these systems feature low FL intensities despite high quantum yields, while others suffer from reduced quantum yields due to optically inactive lowest-lying dark states [52, 64, 65] with strongly inhibited FL at cryogenic temperatures. Irrespective of the actual reason for low intensity, any contamination of the relevant FL by photoemissive substrates or matrices is clearly detrimental to both fundamental studies of nanoemitters and their related applications.

In the following, we present a comprehensive study targeting a quantitative analysis of the FL in the visible spectral range arising from a thin film of PMMA on various dielectric substrates. Surprisingly, we find that PMMA films prepared by standard solution-deposition procedures exhibit optical activity in the visible both at room and cryogenic temperatures. However, the FL is not a characteristic feature of the PMMA itself. It rather stems from fluorescent contaminants in the PMMA matrix that we ascribe to solvent residuals with specific FL intensity and spectra. For individual fluorescent contaminants, pronounced and spectrally stable ZPLs with redshifted vibronic satellites and highly non-classical emission statistics emerge as a generic feature at cryogenic temperatures. At room temperature, thermal broadening of both the ZPL and the vibrational sidebands gives rise to a characteristic three-peak spectrum that can be mistaken for phonon replica of silica color centers [54] or subject to other interpretations [66–72].

3.2 Room temperature characterization of substrates and PMMA

A schematic of our experiment is shown in Fig. 3.1a. We performed FL spectroscopy to study sample-specific emission in the spectral range of 560–770 nm excited with a CW laser[1] at 532 nm, a wavelength frequently used to excite FL in the visible. By raster-scanning the sample with respect to fixed diffraction-limited confocal excitation and collection spots, we acquired maps of FL intensity as in Fig. 3.1b–e with a single photon counting APD, and hyperspectral maps with spectrally dispersed FL as in Fig. 3.1f recorded at each raster-scan pixel for spectral analysis of individual emission hotspots. The studies were complemented by time-correlated FL, second-order FL coherence, and FL excitation spectroscopy experiments performed either at room temperature or at cryogenic temperatures.

In the first stage of the experiments we studied the FL characteristics of bare dielectric substrates. It has been argued recently that silica-based substrates host intrinsic fluorescent centers with sizable FL intensity in the visible [54]. Therefore, we first investigated the FL from the surface of bare fused silica substrates exposed to different cleaning procedures (see Appendix A for details on cleaning protocols). Under ambient conditions and 250 µW irradiation in a FWHM spot of 0.5 µm we acquired raster-scan FL maps[2] shown in Fig. 3.1b–d. For fused silica sonicated subsequently in acetone and isopropanol according to a common cleaning procedure we observed FL from the entire sample surface with inhomogeneous intensity and an average APD count rate of $\sim$ 4 kcts/s (Fig. 3.1b). After an additional sonication step in deionized water the level of FL decreased to an average of $\sim$ 2 kcts/s away from hotspot emission with $\sim$ 4 kcts/s (Fig. 3.1c). Most remarkably, additional treatment with oxygen plasma suppressed the FL from the silica surface below the dark count rate of the APD (Fig. 3.1d). This set of data clearly establishes the absence of intrinsic FL defects on silica substrates. Moreover, it provides a first hint at the source of the FL as stemming from organic surface contaminants that do not withstand oxygen plasma treatment.

For the second experimental stage we prepared substrates free of FL background and covered them by spin-coating with PMMA dissolved in anisole. On a silica substrate with 200 nm of PMMA, we observed the reappearance of fluorescent hotspots with intensities of up to $\sim$ 6 kcts/s on a background of $\sim$ 0.5 kcts/s (Fig. 3.1e) under measurement conditions identical to those of Fig. 3.1b–d. Similar results were found for as-deposited and thermally cross-linked PMMA films fabricated from anisole solutions (see Appendix A for sample details). For most hotspots, the FL was spa-

[1] CNI, MLL-III-532-50-1

[2] Measured using an apochromat (attocube systems, LT-APO/VISIR/0.82) with NA of 0.82.

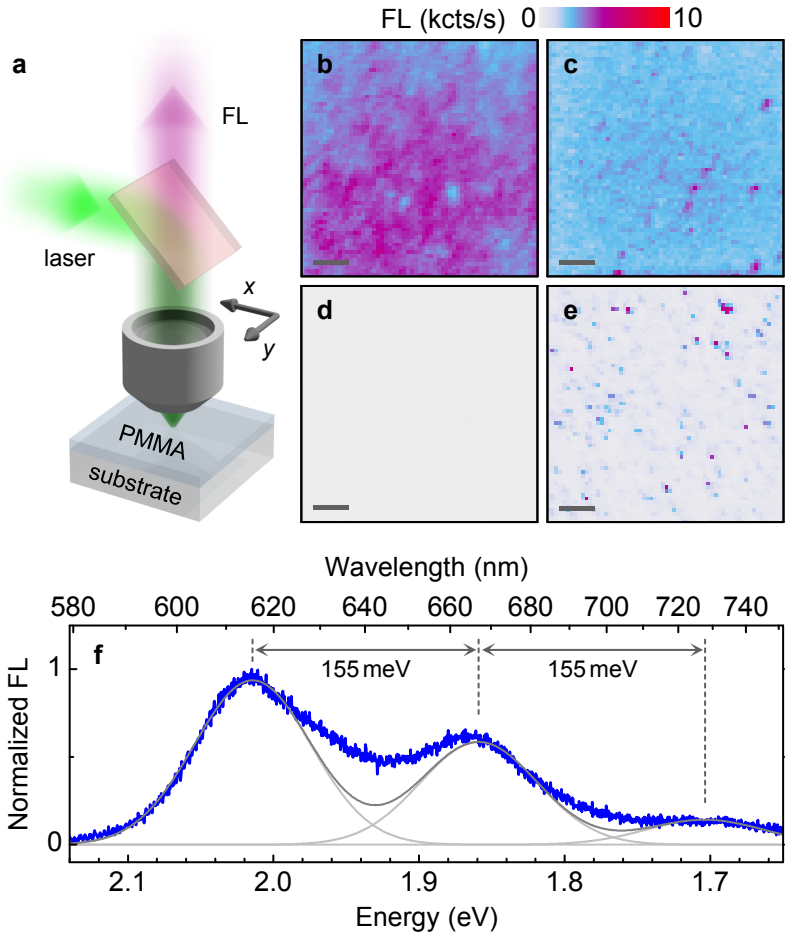

Figure 3.1: a, Schematic of the experiment: fluorescence from dielectric substrates coated with a thin film of PMMA was studied with confocal raster-scan imaging and spectroscopy. Raster-scan fluorescence intensity maps of the surface of fused silica **b**, after sonication in acetone and isopropanol, **c**, additional sonication in deionized water, and **d**, oxygen plasma treatment. **e**, Fluorescence image of plasma-cleaned fused silica with a thin film of PMMA formulated in anisole. All maps were recorded with circularly polarized laser excitation at 532 nm and 130 kW/cm^2; the scale bars are 3 μm. **f**, Fluorescence spectrum of a typical hotspot in PMMA with a fit by three Gaussian peaks with full-width at half-maximum linewidths of 90 meV and equidistant energy spacings of 155 meV. All data were obtained at room temperature.

tially localized to the diffraction-limited spot and characterized by room temperature spectra as in Fig. 3.1f. The spectrum[3] with maximum FL at 2.02 eV (614 nm) can be reproduced with some success by three overlapping Gaussian peaks with FWHM linewidths of 90 meV, equidistant separations of 155 meV, and intensities

[3]Measured using an oil immersion objective (Olympus, UPLFLN 100XOI2) with NA of 1.30.

that reduce with decreasing emission energy (gray solid lines in Fig. 3.1f). Pending an explanation for the mismatch between this simplistic model fit and the actual spectrum, we point out its striking similarity to the spectra ascribed earlier to various sources [53, 54, 66–70, 72]. Moreover, it exhibits a remarkable correspondence with the spectra of individual dyes in PMMA [73, 74], providing a second hint to hydrocarbon molecules as a source for misinterpretation and establishing a link to the visionary association made between the spectra of non-blinking colloidal QDs [70] and organic dyes [75].

3.3 Cryogenic temperature characterization of substrates and PMMA

To elucidate the correspondence between the FL hotspots found at room temperature in thin films of PMMA and the spectral signatures of organic molecules we carried out spectroscopy studies at the cryogenic temperature of 3.1 K. Fig. 3.2a and b show representative cryogenic FL maps of PMMA films on a fused silica substrate and a perforated silicon nitride membrane, respectively. Both maps were acquired in the hyperspectral mode by recording spectrally dispersed FL with a nitrogen-cooled CCD and color-coding its maximum intensity at each raster-scan pixel. Note the conceptual difference to the raster-scan maps recorded with APDs: hyperspectral mapping[4] emphasizes emitters with sharp FL peaks over spectrally broad FL background. Again, we found spatially localized emission from diffraction-limited hotspots (inset of Fig. 3.2a) analogous to our room temperature experiments. A few hotspots in Fig. 3.2b (with up to 120 cts/s) clearly stem from PMMA regions suspended over holes which can be distinguished from the silicon nitride membrane by the respective FL background (gray and blue areas of the map correspond to intensities of 10 and 50 cts/s, respectively). This observation confirms once more that the PMMA film rather than the substrate is the actual host of FL hotspots.

Further supporting evidence is provided in Fig. 3.3 showing hyperspectral FL raster-scans of bare dielectric substrates at the temperature of 3.1 K. The studied substrates were fused silica (Fig. 3.3a), quartz (Fig. 3.3b), and sapphire (Fig. 3.3c), which were all exposed to oxygen plasma prior to the cryogenic measurements. The FL maximum level was identical for fused silica and quartz with count rates given by the readout noise of the nitrogen-cooled CCD. The sapphire substrate exhibited spatially homogeneous FL intensity stemming from a sharp peak at $\sim$ 694 nm (1.787 eV) of the R-line of Cr^{3+} ions in Al_2O_3. Consistently, the measurements agree well with the room temperature observation of Fig. 3.1d.

[4] Recorded in the spectral range of 1.68–2.20 eV with a binning of 0.4 meV.

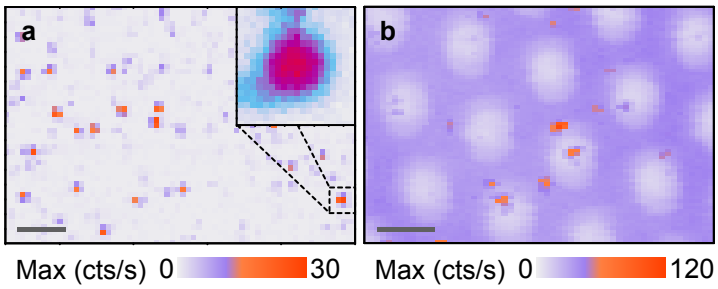

Figure 3.2: **a** and **b**, Cryogenic fluorescence peak intensity maps of PMMA on a fused silica substrate and a perforated silicon nitride membrane, respectively (recorded with 532 nm circularly polarized excitation at 26 kW/cm^2 and linearly polarized excitation at 65 kW/cm^2; the scale bars are 3 μm). The inset in **a** shows a 5× zoom to the hotspot delimited by the dashed box. The gray circular areas in **b** are regions of freestanding PMMA. All data were recorded at 3.1 K.

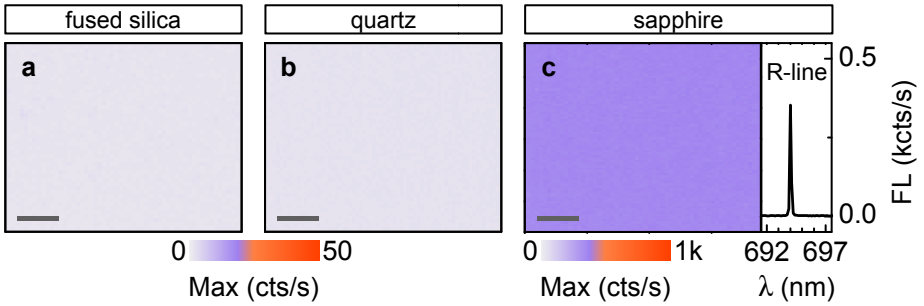

Figure 3.3: **a**, **b**, and **c**, Raster-scan maps of spectrally dispersed fluorescence maxima for oxygen plasma-treated fused silica, quartz, and sapphire substrates, respectively. The fluorescence intensity levels in **a** and **b** correspond to the readout noise of the CCD, the homogeneous level of 350 cts/s in **c** corresponds to the R-line emission at ∼ 694 nm (1.787 eV) of Cr^{3+} ions in sapphire with a characteristic spectrum shown in the right panel. All data were measured at 3.1 K with a linearly polarized 532 nm laser at a power density of 130 kW/cm^2; scale bars are 3 μm.

3.4 Fluorescence properties of single hotspots

We proceed with studies of the spectral features as well as the optical properties of single fluorescent hotspots in anisole-based PMMA films at 3.1 K. A characteristic cryogenic FL spectrum of a hotspot is shown in Fig. 3.4a. It features a narrow and intense peak, which we label as ZPL, accompanied by weak redshifted satellites. More than 60% of localized emission sites exhibited similar spectral characteristics at low temperature. Within this group of emitters with spectrometer-limited ZPLs, 94% of hotspots constitute the class of emitters with a ZPL centered around 2.05 eV emission energy (605 nm emission wavelength). The corresponding normal distribu-

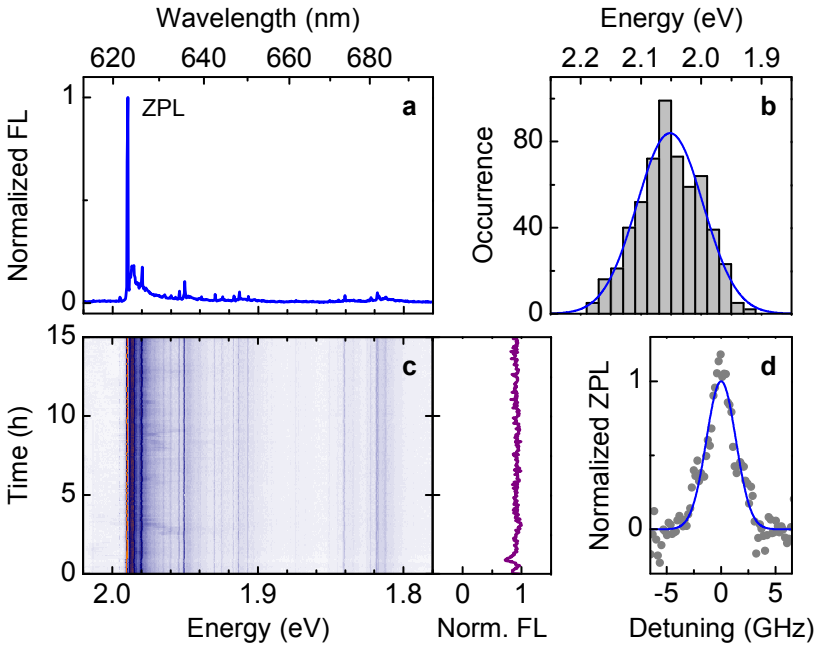

Figure 3.4: **a**, Normalized fluorescence spectrum of a typical hotspot with an intense zero-phonon line (ZPL) and redshifted satellites. **b**, Spectral distribution of the zero-phonon line of about 600 hotspots (the blue line is a Gaussian fit). **c**, Temporal evolution of the fluorescence spectrum (left) and normalized intensity (right) over 15 h for the hotspot with spectrum in **a**. **d**, Zero-phonon line spectrum resolved with a scanning Fabry-Pérot etalon (gray circles). The Gaussian fit (blue line) yields an inhomogeneous linewidth of 3.18 ± 0.13 GHz. All data were recorded at 3.1 K with 532 nm excitation.

tion of the ZPL energy is shown in Fig. 3.4b, where the blue solid line is a Gaussian fit to the histogram with a FWHM of 130 meV. The remaining 6% of the single-site emitters with intense FL exhibited two intense and sharp peaks with two intense satellites and a much narrower spread in the energy of the blue-most peak as shown separately in Fig. 3.5a and b, respectively.

All spectra of the dominant emitter class were remarkably stable over time without significant FL intermittence during the course of observation of 15 h (Fig. 3.4c) and beyond. Throughout the temporal evolution, the ZPL remained spectrometer-limited to one pixel of the CCD corresponding to an upper bound on the FWHM linewidth of 0.4 meV. A high-resolution spectrum recorded with a scanning Fabry-Pérot etalon[5] suggests that spectral wandering broadens the ZPL on a tens of minutes timescale to an inhomogeneous peak with a FWHM of 3.18 ± 0.13 GHz (Fig. 3.4d). These spectral signatures find their correspondence in the studies of hydrocarbon fluorophores embedded in a polymer host matrix [77–79]. Within this

[5]Home-built, spectral resolution of 150 MHz and scanning rate of 5.5 MHz/s, see Ref. 76.

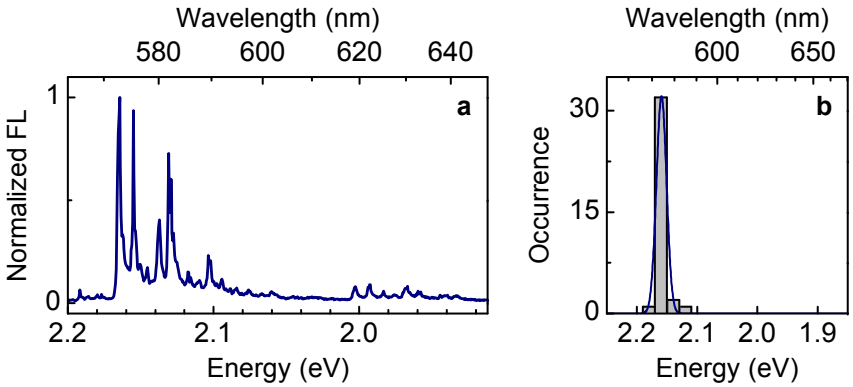

Figure 3.5: **a**, Normalized fluorescence spectrum of a hotspot emitter featuring two intense and sharp emission peaks with two intense vibronic satellites. **b**, Corresponding energy distribution of the blue-most peak; solid line is a normal distribution fit with a full-width at half-maximum of 20 meV. All data were measured at 3.1 K with excitation at 532 nm.

framework, low-temperature FL of single molecules is characterized by a spectrally narrow ZPL associated with the principal electronic transition [80] and sidebands stemming from Franck-Condon transitions between vibronically dressed molecular electronic states [81, 82]. Stabilized in PMMA, single molecules exhibit FL with low intermittency and ZPLs limited by spectral diffusion to ~ 1 GHz [78, 83]. The redshifted satellites of the ZPL are equally well pronounced in vibronic spectroscopy [84] of molecules with characteristic vibrational degrees of hydrocarbon complexes.

The data of Fig. 3.6 further substantiates the correspondence between the optical properties of single hotspots and molecular emitters. With polarization-resolved measurements shown in Fig. 3.6a we confirmed the dipolar character associated with the molecular transition of the ZPL [74]. The orientation of the absorption and emission axes measured with linearly polarized excitation and detection, respectively, were determined as collinear within our experimental precision. Furthermore, time-correlated measurements of Fig. 3.6b revealed the characteristic FL decay dynamics of molecules on nanoseconds timescale [85]. The single-exponential lifetimes of 3.8 and 3.6 ns for the ZPL within a spectral window of 60 meV and the total FL intensity, respectively, were the same within the temporal resolution of ~ 0.3 ns in our experiments[6], identifying redshifted sidebands as vibronic ZPL replicas. Finally, single photon emission statistics as a hallmark of single-molecule FL [86, 87] are presented in Fig. 3.6c and d. With photon correlation spectroscopy we observed pronounced photon antibunching in the normalized second-order coherence function

[6]Picosecond excitation (PicoQuant, LDH-P-FA-530B) and APD detection.

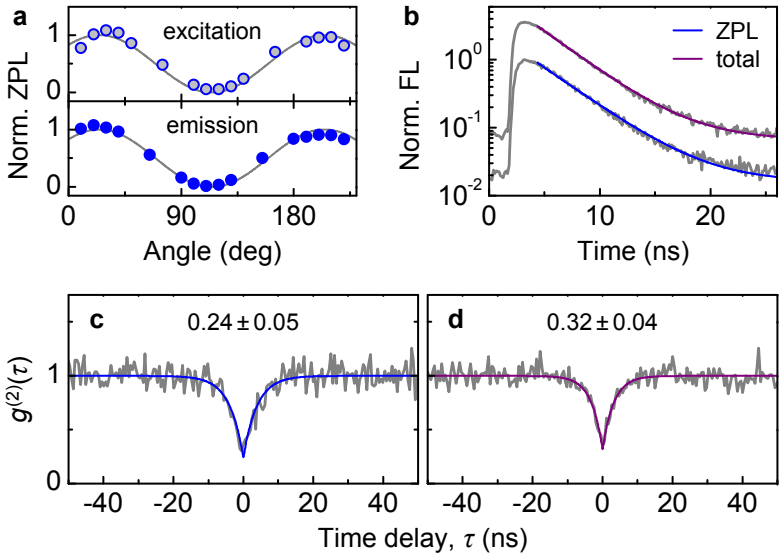

Figure 3.6: **a**, Polarization characteristics of the zero-phonon line: normalized intensity as a function of the rotation angle of a linear polarizer in excitation and detection (top and bottom panels, respectively; the gray lines represent the same functional form of the fits to the data). **b**, Time-correlated decay of the zero-phonon line and the total fluorescence (gray traces) of a single hotspot, and corresponding monoexponential fits with decay constants of 3.8 and 3.6 ns (blue and purple traces). The plots were offset for clarity. **c** and **d**, Second-order coherence function $g^{(2)}(\tau)$ recoded with and without spectral selection of the zero-phonon line, respectively. The blue and purple lines are fits to the data with multiphoton probabilities of 0.24 ± 0.05 and 0.32 ± 0.04. All data were recorded at 3.1 K with excitation at 532 nm.

$g^{(2)}(\tau)$ at zero time delay for both the FL within a band-pass interval of 60 meV around the ZPL (with $g^{(2)}(0) = 0.24 \pm 0.05$ in Fig. 3.6c) and the full FL spectrum without spectral filtering ($g^{(2)}(0) = 0.32 \pm 0.04$ in Fig. 3.6d). Thus, within the uncertainty of our measurement, we can rule out simultaneous photon emission into the ZPL and the sideband spectrum associated with the vibronic ZPL satellites.

Having identified the fluorescent hotspots in PMMA as single molecules, we utilized vibrationally resolved FL spectroscopy [82, 84, 88] to shed light on their molecular nature. Fig. 3.7a shows a spectrum of a hotspot that is representative for fluorescent contaminants in PMMA prepared with anisole as solvent. A series of low-frequency vibrational modes contributes to the sidebands below 80 meV (645 cm^{-1}), followed by a group of replicas around 173 meV (1395 cm^{-1}) and a weaker satellite group around 346 meV (2790 cm^{-1}). The latter is in fact a second harmonic of the preceding group as confirmed by correlation analysis between all individual peaks of the two groups upon a spectral shift by 173 meV. All main vibrational features in emission have their broadened counterpart resonances in absorption, as

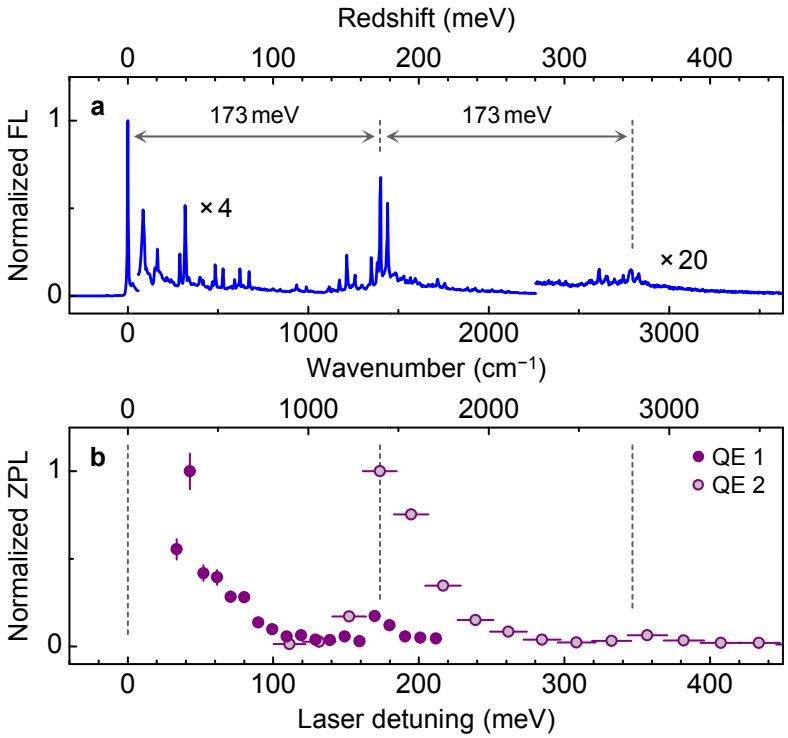

Figure 3.7: **a**, Normalized fluorescence spectrum of a typical hotspot recorded with excitation at 532 nm and plotted as a function of spectral redshift from the zero-phonon line at 2.134 eV. The intensity was magnified by a factor of 4 (20) above 7 meV (280 meV) redshift to highlight two groups of phonon sidebands with a spacing of 173 meV. **b**, Normalized zero-phonon line intensity as a function of excitation laser detuning for two quantum emitters (QE) with spectral features as in **a** recorded within excitation wavelength intervals of 538–583 and 485–555 nm (solid and open circles, respectively). All data were recorded at 3.1 K.

demonstrated by the FL excitation spectra in Fig. 3.7b recorded for two typical emitters[7] with different ZPL energies as a function of laser energy detuning at constant excitation power. For both quantum emitters of Fig. 3.7b, the absorption is enhanced whenever the laser detuning with respect to the ZPL matches the energy of the vibronic sidebands (the dashed lines in Fig. 3.7 emphasize the correspondence between the resonances in emission and absorption).

The vibrationally resolved spectrum of Fig. 3.7b is typical for fluorescent molecules in PMMA films from anisole-based solutions. It exhibits a striking similarity with the cryogenic FL of anthracene characterized by a ZPL in the ultraviolet (around 3 eV) and a pronounced vibronic satellite group around 1400 cm^{-1}

[7] QE 1 and QE 2 were excited by an optical parametric oscillator (Coherent, Mira-OPO) and a filtered supercontinuum laser (NKT Photonics, SuperK EXW-12) with FWHM spectral bandwidths of 0.5 nm and 5.5 nm, respectively.

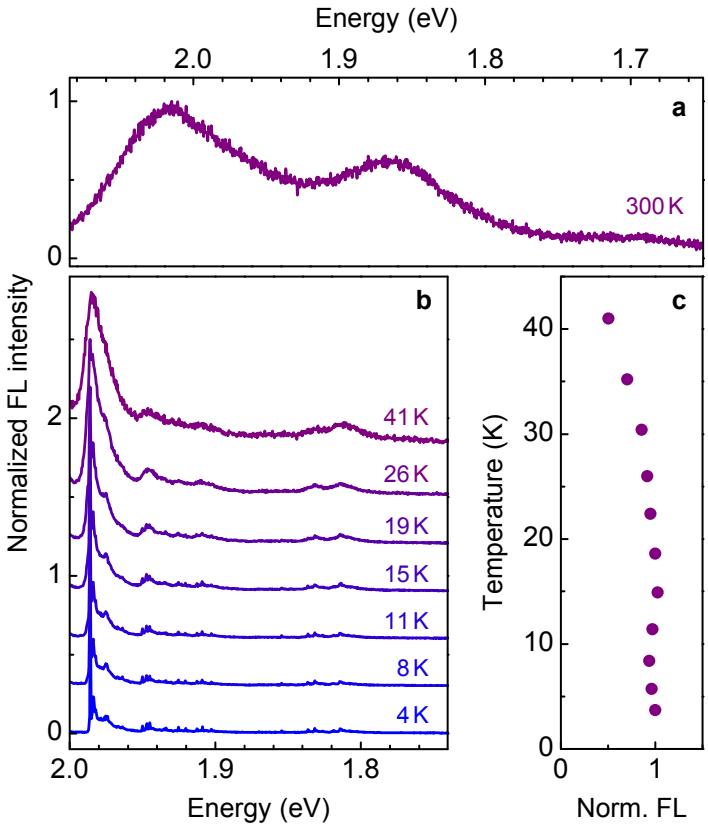

Figure 3.8: **a**, Normalized fluorescence spectra of a hotspot emitter measured at 300 K (reproduced from Fig. 3.1f) and **b**, of a similar emitter for selected temperatures ranging from 4 K to 41 K (the traces were offset for clarity). **c**, Total fluorescence normalized to the maximum value at 4 K as a function of temperature. Laser excitation was at 532 nm.

redshifts [89]. The according vibrational degrees of freedom are related to the intramolecular stretching of adjacent carbon bonds in polycyclic aromatic hydrocarbons [82]. The observation of the ZPL emission in the visible (around 2 eV) from anisole-based PMMA suggests that the optical activity of solvent-related contaminants in such films stems from acene chains such as pentacene, or from anthracene-derived dyes such as alizarin.

The evolution of the spectral features as a function of temperature is presented in Fig. 3.8. The ZPL and the vibronic satellites broadened upon heating from 4 to 41 K (Fig. 3.8b), and the overall FL decreased gradually for temperatures above $\sim$ 25 K (Fig. 3.8c). Both the initial intensity and the spectral lineshape were recovered upon successive cooling back to 4 K. The trend of thermal broadening as in Fig. 3.8b eventually results in significant spectral overlap of the ZPL and vibronic satellites at room temperature with predominant contributions from the vibronic group around $\sim$ 155 meV and its second harmonic around $\sim$ 310 meV redshifts (Fig. 3.8a).

3.4.1 Quantum yield estimate

In the following we estimate the FL quantum yield of the dominant fluorescent hotspots in PMMA films formed with anisole-based solutions as a measure for their efficiency and significance. The quantum yield of an emitter is given by the ratio of emitted photons to absorbed photons per unit time. In our experiments it is calculated by scaling the FL intensity of single hotspots to photostable emitters with known optical properties. We used single NV color centers in bulk diamond that exhibit a quantum yield of $\Phi_{\mathrm{NV}} \simeq 70\%$ [90] and a dipole averaged absorption cross-section of $\sigma_{\mathrm{NV}} \simeq 3.1 \times 10^{-17}$ cm^2 [91] for 532 nm excitation. With these quantities, the conversion cross-section of a fluorescent hotspot, given by the product of the corresponding quantum yield Φ_{FH} and absorption cross-section σ_{FH}, is determined as:

$$\Phi_{\mathrm{FH}}\sigma_{\mathrm{FH}} = \frac{I_{\mathrm{FH}}}{I_{\mathrm{NV}}}\frac{\tau_{\mathrm{FH}}}{\tau_{\mathrm{NV}}}\frac{\Omega_{\mathrm{NV}}}{\Omega_{\mathrm{FH}}}\Phi_{\mathrm{NV}}\sigma_{\mathrm{NV}}. \tag{3.1}$$

Here, the term $I_{\mathrm{FH}}/I_{\mathrm{NV}}$ is the FL intensity of a hotspot scaled to the FL of a single NV center for the same excitation power in the linear response regime of both emitters. This ratio ranged from 1.9 to 2.4 for room temperature measurements and peaked at ~ 13.2 for cryogenic temperatures of 3.1 K and 4.2 K. The emitters were excited with CW excitation at 532 nm and circular polarization to ensure averaging over the possible orientations of the transition dipole moments. The factor $\tau_{\mathrm{FH}}/\tau_{\mathrm{NV}}$ accounts for the different FL lifetimes of the fluorescent hotspots and the NV centers with $\tau_{\mathrm{FH}} \simeq 3.6$ ns and $\tau_{\mathrm{NV}} \simeq 12.9$ ns determined experimentally. Finally, we also account for the difference in the effective collection solid angles for fluorescent dipoles embedded in different dielectric environments (PMMA and diamond) with respective refractive indices via $\Omega_{\mathrm{NV}}/\Omega_{\mathrm{FH}}$ which was close to $\simeq 0.35$ in our experiments.

With these values the conversion cross-section of a typical fluorescent hotspot excited at 532 nm was in the order of $\sim 5 \times 10^{-18}$ cm^2 at room temperature and increased to $\sim 3 \times 10^{-17}$ cm^2 at cryogenic temperatures. Using $\sigma_{\mathrm{FH}} \simeq 1 \times 10^{-16}$ cm^2 as a typical absorption cross-section of the second absorption band of common polycyclic hydrocarbon compounds [92], we obtain an estimate for the FL quantum yield Φ_{FH} of $\sim 5\%$ at room temperature and up to 30% at cryogenic temperatures. We obtained similar values, both at room and cryogenic temperatures, from scaling the quantum yield of fluorescent hotspots in anisole-based samples to FL characteristics of individual terrylenediimide molecules.

3.5 Spectroscopy of PMMA films prepared with different solvents

After examining fluorescent hotspots in anisole-based PMMA using vibrational FL spectroscopy, we extended our studies to PMMA films derived from other solvents (see Appendix A for sample preparation details). As highlighted by the raster-scan maps of Fig. 3.9, the areal density and the FL intensity of hotspots in PMMA films formed with chlorobenzene (Fig. 3.9d, e), methyl isobutyl ketone (Fig. 3.9g, h) and toluene (Fig. 3.9j, k) were similar to anisole-based PMMA characteristics (Fig. 3.9a, b). The vibronic signatures, however, showed significant differences. Fig. 3.9c, f, i, and l show normalized average spectra of 25 brightest fluorophore contaminants in PMMA films prepared with different solvents.

The spectrum of a typical hotspot in chlorobenzene-based PMMA features a low-frequency vibronic band around 250 cm^{-1} and a pronounced high-frequency band around 1400 cm^{-1} discussed earlier (as indicated by the rhomb and the hexagon in Fig. 3.9f). In contrast, the vibronic FL characteristics of hotspots in PMMA films formed with methyl isobutyl ketone and toluene solutions (Fig. 3.9i and l, respectively) exhibit additional vibrational signatures at 548 and 757 cm^{-1}. The vibronic modes, labeled with rhombs and tip-up and tip-down triangles in Fig. 3.9f, i, and l are characteristic of rylene dyes composed of naphthalenes. While the low-frequency mode (rhombs in Fig. 3.9f, i, and l) is close to that of the long axis stretch of a terrylene molecule, the higher-frequency modes (tip-up and tip-down triangles in Fig. 3.9i and l) are consistent with the short axis stretch and ring deformation of outer naphthalenes, respectively [82]. Note that naphthalene-related bands of rylene dyes are only very weakly expressed in the averaged vibronic FL spectra observed in anisole- and chlorobenzene-based PMMA films (Fig. 3.9c and f).

In addition to solvent-specific differences in the spectra of fluorescent hotspots in PMMA, vibrationally resolved FL spectroscopy identifies the normal modes of aromatic hydrocarbons around 170 meV (1400 cm^{-1}) as a generic feature of FL contaminants at low temperatures. At elevated temperatures, these modes develop into broad vibronic satellites (see Fig. 3.8 for FL spectra at different temperatures) that accompany the FL from the thermally broadened principal molecular transition. With this in mind, the interpretation of the three-peak structure of the room-temperature FL spectrum in Fig. 3.1f as arising from an organic fluorophore is straight forward. For an adequate modeling, however, the contributions of all other vibrational modes must be taken into account. The main corrections to the inhomogeneous spectral profile of the ZPL and the vibronic modes of polycyclic hydrocarbons will naturally appear on the low-energy side of the peaks, where the fit with three Gaussians most significantly deviates from the actual spectrum.

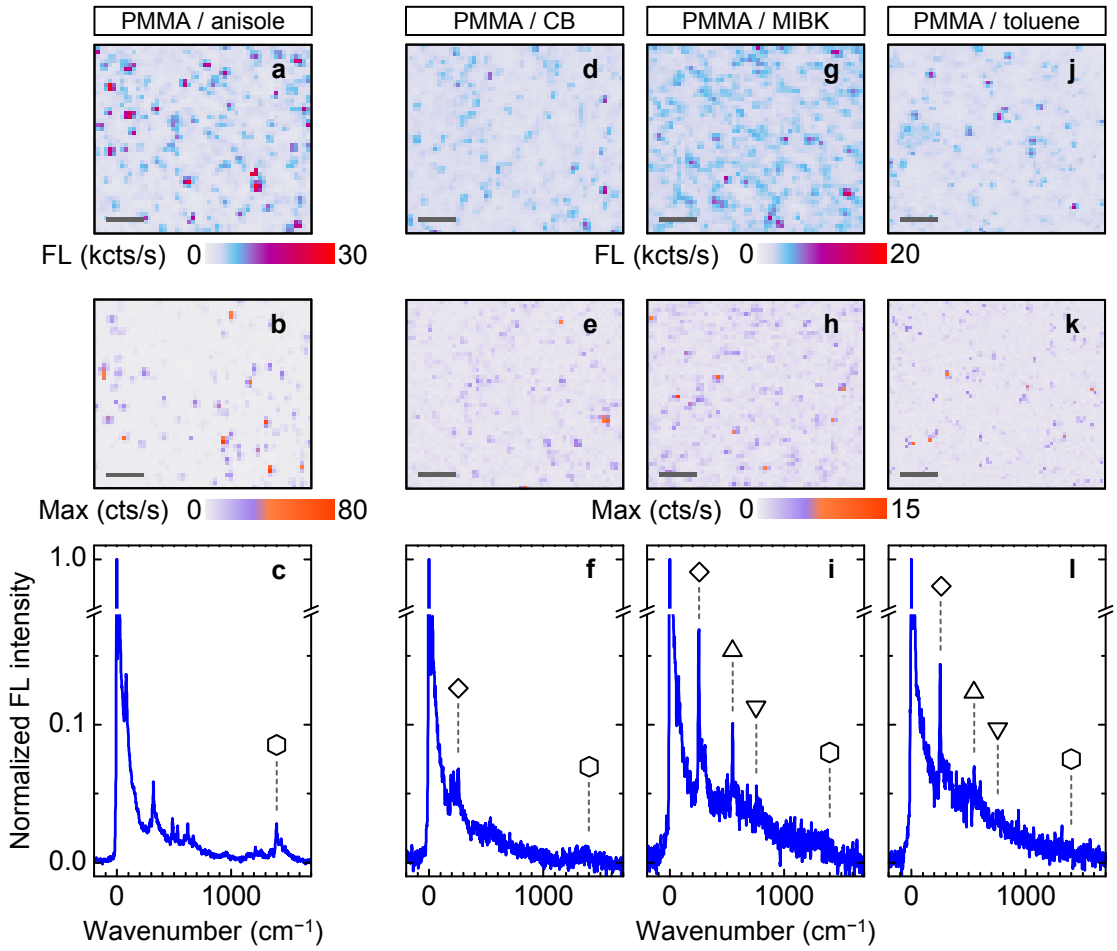

Figure 3.9: **a** and **b**, Raster-scan maps of integrated fluorescence intensity and spectrally dispersed fluorescence maxima, respectively, for PMMA dissolved with anisole. **d** and **e**, **g** and **h**, **j** and **k**, Same for PMMA films prepared with chlorobenzene (CB), methyl isobutyl ketone (MIBK), and toluene solutions, respectively. All scale bars are 3 μm. **c**, **f**, **i**, and **l**, Average fluorescence spectra of 25 most intense hotspots in PMMA dissolved in anisole, chlorobenzene, methyl isobutyl ketone, and toluene, respectively, displayed as a function of the redshift from the zero-phonon line. The symbols indicate specific vibronic modes of hydrocarbon-based molecular dyes. All data were recorded at 3.1 K with circularly polarized laser excitation at 532 nm and 52 kW/cm^2 on thermally annealed PMMA films of 200 nm thickness on oxygen plasma-cleaned fused silica.

3.6 Conclusions

In concise terms, our comprehensive study of fluorescent spots, ubiquitously present in PMMA films and on contaminated dielectric substrates, leads to the conclusion that organic fluorophores are the actual source of misinterpreted FL signatures. The quantum yield estimate of such organic quantum emitters ranges from $\sim 5\%$ at room

temperature up to 30% at 3.1 K. Even though these values are not remarkably high, the corresponding FL intensity can be significant in studies of photoactive systems with reduced quantum yields in cryogenic or ambient environments. In fact, we found the FL intensity of PMMA hotspots to be roughly a third of the emission intensity of individual terrylenediimide molecules at cryogenic temperatures, and in many instances even more intense than commercial radiant dyes at ambient conditions. Given the present technological limitations to solvent purity, it seems unlikely that contamination of PMMA and other polymer matrices can be completely avoided in future experiments. On the other hand, the abundance of stable quantum emitters in polymer films could facilitate a range of fundamental studies and technological developments relying on simple and cheap sources of non-classical light.

Chapter 4

Spin and valley physics in two-dimensional semiconductors

This chapter provides basic theoretical concepts and an overview to the electronic and optical properties of group-VIB transition metal dichalcogenide monolayers. As a new class of two-dimensional semiconductors with a direct band gap and a counterpart to the well-known graphene, their distinct structural and electronic properties are at first briefly summarized in a phenomenological manner. Apart from the spin degree of freedom, crystal electrons in these materials posses a valley pseudospin which describes degenerate band extrema in momentum space and provides a further binary quantum degree of freedom. By exploiting the pertinent symmetries of the system, the non-centrosymmetric band extrema are modeled within a framework of two bands. This simple model is then used to derive valley- and spin-dependent optical selection rules for interband transitions. Moreover, the missing spatial inversion symmetry of the two-dimensional lattice leads to rich Berry phase physics with finite Berry curvatures and orbital magnetic moments in Bloch bands. While the former couples to an applied in-plane electric field and leads to anomalous perpendicular velocity, the latter gives rise to the valley Zeeman effect for an out-of-plane magnetic field. Finally, the formation of strongly bound excitons due to strong attractive Coulomb interaction is discussed.

4.1 Crystal structure and electronic properties

Layered materials are composed of stacked two-dimensional atomic crystals weakly bonded by van der Waals forces [4, 7]. The in-plane stability of the individual atomic planes is ensured by strong covalent bonds. Among these layered materials, especially group-VIB TMD monolayers have attracted significant interest as a new class of two-dimensional semiconductors with exciting electronic and optical properties [25, 93–96]. The chemical composition of these materials is of the form MX_2, where the transition metal M is either molybdenum or tungsten (Mo or W) and the chalcogen X is either sulfur, selenium, or tellurium (S, Se, or Te) [97]. In general the monolayers consist of three covalently bonded atomic planes X-M-X and possess three polytypic phases: $1T$, $1T'$, and $1H$ [98]. However, the $1T$ lattice structure with rhombohedral coordination around the transition metal atom is typically considered unstable. The $1T'$ polytype is a distorted variant of the $1T$ phase, where M atoms are off-centered from their ideal position so that they are surrounded by eight neighbors, six X atoms and two M atoms with metallic M-M bonding. Within the family of six possible group-VIB TMD compounds, only WTe_2 monolayers naturally crystallize in this rare $1T'$ phase and are in fact two-dimensional topological insulators [99, 100]. The remaining five monolayer crystals are found in the $1H$ phase, where M atoms are coordinated by six X atoms residing at the corners of trigonal prisms. Thus, the middle plane, containing only transition metal atoms, acts as a mirror plane between the top and bottom layers of chalcogen atoms. Together the sheets form a two-dimensional hexagonal lattice similar to graphene, as shown in Fig. 4.1a. However unlike graphene, $1H$ phase group-VIB TMD (TMD for short from here on) monolayers have no inversion center and are therefore non-centrosymmetric with their crystal symmetry described by the D^1_{3h} space group.

The electronic structure of bulk TMD materials is governed by an indirect band gap [101], which increases in energy as the layer number is reduced due to quantum confinement in the out-of-plane direction [102]. In the limit of a monolayer, the indirect band gap crosses over to a direct band gap as was first shown for MoS_2 [9, 10]. The direct band gap is located at the six corners of the hexagonal Brillouin zone and, depending on the chemical composition of the TMD monolayer, spans the visible to the near-infrared spectral range [9, 10, 103–105]. These non-central local extrema or K and K' valleys of the conduction and valence bands are degenerate in energy but have opposite spin configurations. This in part is due to spin splitting of both bands caused by spin-orbit interaction originated from the heavy transition metal atoms [106, 107]. The form of the spin splitting is dictated by the σ_h symmetry element of the system, which describes the reflection transformation about the middle plane of the monolayer. Consequently, the σ_h transformation of a given Bloch state must also

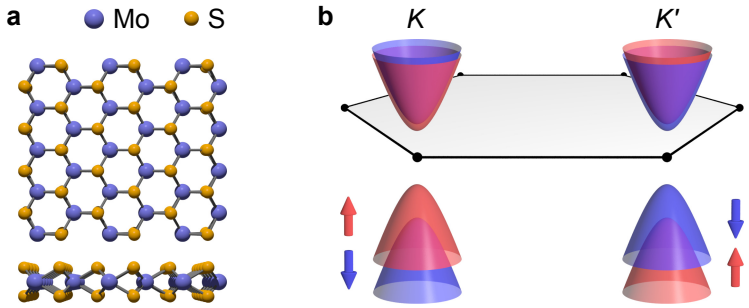

Figure 4.1: **a**, Real space top and side views of monolayer MoS_2 in the $1H$ phase as a representative two-dimensional group-VIB transition metal dichalcogenide. **b**, Schematic band structure of monolayer $1H$-MoS_2 at the corners of its hexagonal Brillouin zone. The spin-orbit split valence and conduction subbands are colored according to their spin degree of freedom in the two inequivalent valleys K and K'. Note that the order of the conduction subbands is reversed for tungsten-based monolayers.

be an eigenstate of the system Hamiltonian with the same eigenenergy. Out-of-plane z spin vectors are conserved under σ_h operation, whereas the transformation of an in-plane spin vector is its opposite. Accordingly, finite spin splittings are only allowed for spin states with expectation values along z. The other key factors responsible for the energy bands to spin-split with opposite splitting signs at the K and K' valleys are the explicitly broken inversion symmetry and the time-reversal symmetry. While for systems without a center of inversion states with opposite wavevectors ($\mathbf{q}$ and $-\mathbf{q}$ or K and K'), same spin states ($\uparrow$ or $\downarrow$), and different energies E are permitted [108]. In the presence of time-reversal symmetry energies of states with opposite wavevectors and spins are related to each other as $E_\uparrow(\mathbf{q}) = E_\downarrow(-\mathbf{q})$. Thus, spin and the binary valley degree of freedom or valley pseudospin (K or K') are uniquely locked providing an exciting platform to explore coupled spin and valley physics [25, 109]. A schematic band structure around the corners of the Brillouin zone for monolayer MoS_2 as a prototypical TMD is presented in Fig. 4.1b.

Bloch electrons in monolayer TMDs are well described as massive Dirac fermions [109] with an absolute value of the effective mass in the order of $\sim 0.5m_0$ [110], where m_0 is the free electron mass. The corresponding electronic band edges mainly stem from d-orbitals of the transition metal atoms, with an angular momentum quantum number $l = 2$, and a small contribution from a mixture of p-orbitals of the chalcogen atoms, with $l = 1$. The wavefunctions of the orbitals are combined chirally in spherical harmonic form in accordance with the wavevector point group C_{3h} at K and K' [94]. This symmetry group is generated by σ_h and the element C_3, defined as rotation by $2\pi/3$ around the z axis. Thus, all Bloch states at K and K' have to be eigenstates of both point group operations. Considering only the dominant d-

orbitals, Bloch wavefunctions are formed as a linear combination of atomic orbitals ϕ_c^κ for the conduction band minimum and ϕ_v^κ for the valence band maximum. These symmetry adapted orbitals with magnetic quantum numbers m are given by [94, 109]:

$$\phi_c^\kappa(\mathbf{r}) = d_{z^2} = d_0 \qquad \text{with} \quad m = 0, \tag{4.1a}$$

$$\phi_v^\kappa(\mathbf{r}) = \frac{1}{\sqrt{2}}\left(d_{x^2-y^2} + \mathrm{i}\kappa d_{xy}\right) = d_{2\kappa} \quad \text{with} \quad m = 2\kappa, \tag{4.1b}$$

where $\mathbf{r} = (x, y, z)$ and the valley index κ is $+1$ for K and -1 for K'. The functions d_{z^2}, d_{xy}, and $d_{x^2-y^2}$ are real orbitals, d_0 and $d_{2\kappa}$ are spherical orbitals d_m [111].

The m numbers of ± 2 in the valence band result in giant spin-orbit splittings exceeding 100–200 meV and 400 meV for Mo- and the heavier W-based TMD monolayers, respectively [106, 112]. Here, the upper valence electron spin states are generally $\uparrow$ in the K valley and $\downarrow$ in the K' valley. As for the conduction band edge, the spin-orbit splitting originates from coupling to remote higher-order bands of d-orbital character with $m = \pm 1$ of the transition metal atoms [113, 114] and, furthermore, the secondary p-orbital contributions with $m = \pm 1$ of the chalcogen atoms [106, 107]. The two competing contributions lead to energy splittings ranging from 3 meV to $\sim$ 40 meV with a sign difference between Mo- and W-based monolayers [106, 107]. The electron spin states of the lower conduction subband for Mo-based (W-based) monolayers are mostly $\uparrow$ ($\downarrow$) in the K valley and $\downarrow$ ($\uparrow$) in the K' valley (see Fig. 4.1b for MoS_2). Through spin-orbit engineering in alloy monolayers, for example $Mo_{(1-x)}W_xSe_2$, spin degeneracy between the K and K' conduction band edge states is also possible [115].

4.2 Symmetry-based two-band model

The low energy physics at the band edges of TMD monolayers can be well captured by a two-band model, where the system is described with $\mathbf{k} \cdot \mathbf{p}$ perturbation theory [109]. For this model, the general form of the Hamiltonian can be derived by using the symmetries of the crystal structure. Spin-orbit interaction is included as an intra-atomic contribution.

We begin with the stationary one-electron Schrödinger equation for eigenstates expanded in terms of direct products of $|\mathbf{r}\rangle$ and z-spin kets $|s\rangle$ with $s \in \{\uparrow, \downarrow\}$:

$$|\Psi_{\nu,\mathbf{q}}\rangle = \sum_s \int \mathrm{d}\mathbf{r}\, \psi_{\nu,\mathbf{q},s}(\mathbf{r})\, |\mathbf{r}\rangle \otimes |s\rangle\,, \tag{4.2}$$

where the spinors $\langle \mathbf{r}s|\Psi_{\nu,\mathbf{q}}\rangle = \psi_{\nu,\mathbf{q},s}(\mathbf{r})$ are Bloch-type functions indexed by subband ν and wavevector $\mathbf{q}$ within the first Brillouin zone.

The Schrödinger equation with spin-orbit interaction then satisfies

$$\hat{H}\,|\Psi_{\nu,\mathbf{q}}\rangle = E_\nu(\mathbf{q})\,|\Psi_{\nu,\mathbf{q}}\rangle\,, \tag{4.3}$$

where $E_\nu(\mathbf{q})$ is the $\mathbf{q}$-dependent eigenenergy of $|\Psi_{\nu,\mathbf{q}}\rangle$ and the Hamiltonian is

$$\hat{H} = \frac{1}{2m_0}\hat{\mathbf{p}}^2 + V(\mathbf{r}) + \frac{\hbar}{4m_0^2c^2}(\nabla V \times \hat{\mathbf{p}})\cdot\hat{\boldsymbol{\sigma}}. \tag{4.4}$$

Here, $\hat{\mathbf{p}} = (\hat{p}_x, \hat{p}_y, \hat{p}_z)$ is the momentum operator, $V(\mathbf{r})$ is the lattice potential, $\hat{\boldsymbol{\sigma}} = (\hat{\sigma}_x, \hat{\sigma}_y, \hat{\sigma}_z)$ is the dimensionless spin operator, $\hbar$ is the reduced Planck constant, and c is the speed of light in vacuum.

To proceed we consider solutions for small wavevectors $\mathbf{k} = (k_x, k_y, k_z)$ measured from the band extrema K and K' with wavevectors $\kappa\mathbf{K}$. At these points with $\mathbf{k} = 0$, eigenstates $|\Psi_{\nu,\kappa\mathbf{K}}\rangle$ can be approximately factorized into a pure spin state and an orbital Bloch state $|\psi^\kappa_\mu\rangle = |\psi_{\mu,\kappa\mathbf{K}}\rangle$ characterized by the bulk band index μ [116]. For fixed κ the lattice-periodic functions $\mathrm{e}^{-\mathrm{i}\kappa\mathbf{K}\cdot\mathbf{r}}\,\langle\mathbf{r}|\psi^\kappa_\mu\rangle$ then provide a complete and orthonormal set for any function with lattice symmetry [117, 118]. Thus, Bloch-type spinors $\langle\mathbf{r}s|\Psi_{\nu,\mathbf{k}+\kappa\mathbf{K}}\rangle$ can be expanded as a linear combination of $\mathrm{e}^{\mathrm{i}\mathbf{k}\cdot\mathbf{r}}\,\langle\mathbf{r}|\psi^\kappa_\mu\rangle$. Eigenstates of $\hat{H}$ in the vicinity of $\kappa\mathbf{K}$, for convenience labeled by the μ and s indices of the dominant states instead of the subband index ν, then have the form

$$|\Psi_{\nu,\mathbf{k}+\kappa\mathbf{K}}\rangle = \mathrm{e}^{\mathrm{i}\mathbf{k}\cdot\mathbf{r}}\sum_{\mu',s'}\mathcal{C}^\kappa_{\mu,s,\mu',s'}(\mathbf{k})\,|\psi^\kappa_{\mu'}\rangle\otimes|s'\rangle = |\Psi^\kappa_{\mu,\mathbf{k},s}\rangle\,, \tag{4.5}$$

where $\mathcal{C}^\kappa_{\mu,s,\mu',s'}(\mathbf{k})$ are expansion coefficients. For this result together with the notations $|\psi^\kappa_\mu s\rangle = |\psi^\kappa_\mu\rangle\otimes|s\rangle$ and $E^\kappa_{\mu,s}(\mathbf{k}) = E_\nu(\mathbf{k}+\kappa\mathbf{K})$, the Schrödinger equation of Eq. 4.3 can be rewritten as

$$\sum_{\mu',s'}\mathcal{C}^\kappa_{\mu,s,\mu',s'}(\mathbf{k})\big[\hat{H}_{\mathrm{eff}} - E^\kappa_{\mu,s}(\mathbf{k})\big]\,|\psi^\kappa_{\mu'}s'\rangle = 0. \tag{4.6}$$

The operator $\hat{H}_{\mathrm{eff}} = \hat{H}_0 + \hat{H}_{\mathbf{k}\cdot\mathbf{p}} + \hat{H}_{\mathrm{so}}$ is the effective Hamiltonian with

$$\hat{H}_0 = \frac{1}{2m_0}\hat{\mathbf{p}}^2 + V(\mathbf{r}), \tag{4.7a}$$

$$\hat{H}_{\mathbf{k}\cdot\mathbf{p}} = \frac{\hbar}{m_0}\mathbf{k}\cdot\hat{\mathbf{p}} + \frac{\hbar^2\mathbf{k}^2}{2m_0} \approx \frac{\hbar}{m_0}\mathbf{k}\cdot\hat{\mathbf{p}}, \tag{4.7b}$$

$$\hat{H}_{\mathrm{so}} = \frac{\hbar}{4m_0^2c^2}[\nabla V\times(\hat{\mathbf{p}}+\hbar\mathbf{k})]\cdot\hat{\boldsymbol{\sigma}} \approx \frac{\hbar}{4m_0^2c^2}(\nabla V\times\hat{\mathbf{p}})\cdot\hat{\boldsymbol{\sigma}}. \tag{4.7c}$$

Here, $\hat{H}_0$ is the unperturbed Hamiltonian without spin-orbit coupling, $\hat{H}_{\mathbf{k}\cdot\mathbf{p}}$ is the $\mathbf{k}\cdot\mathbf{p}$ perturbation, where we neglect the free electron term $\hbar^2\mathbf{k}^2/(2m_0)$, and $\hat{H}_{\mathrm{so}}$ is the spin-orbit interaction, which we assume to be independent of $\mathbf{k}$.

In the following we take into account only the lowest conduction and highest valence bulk bands with $\mu = c$ and v, respectively, for the orbital states $|\psi_\mu^\kappa\rangle$. The symmetry adapted wavefunctions of these states can be approximated as

$$\langle \mathbf{r}|\psi_\mu^\kappa\rangle = \psi_\mu^\kappa(\mathbf{r}) = N^{-1/2}\sum_n \mathrm{e}^{\mathrm{i}\kappa\mathbf{K}\cdot(\mathbf{R}_n+\boldsymbol{\delta})}\phi_\mu^\kappa(\mathbf{r}-\mathbf{R}_n-\boldsymbol{\delta}), \tag{4.8}$$

where $\mathbf{R}_n$ is the position vector of the nth unit cell, $\boldsymbol{\delta}$ is the site of the transition metal atom within the unit cell, and N is the number of unit cells in the lattice. The functions $\phi_\mu^\kappa(\mathbf{r})$ are spherical orbitals $d_m(\mathbf{r})$ as given by Eqs. 4.1.

We can now determine the matrix representation of the effective Hamiltonian $\hat{H}_{\text{eff}}$ in the basis $\{|\psi_c^\kappa s\rangle, |\psi_v^\kappa s\rangle\}$. For the unperturbed system without spin-orbit coupling and direct band-gap energy Δ, the Hamiltonian matrix is

$$H_0 = \begin{bmatrix} \Delta/2 & 0 \\ 0 & -\Delta/2 \end{bmatrix}, \tag{4.9}$$

where we chose the zero energy symmetrically.

To determine the matrix elements of $\hat{H}_{\mathbf{k}\cdot\mathbf{p}}$, we introduce $k_\pm = k_x \pm \mathrm{i}k_y$ and $\hat{p}_\pm = \hat{p}_x \pm \mathrm{i}\hat{p}_y$. Since the effective Hamiltonian is invariant under σ_h reflection and $\hat{p}_z$ is not, we can simplify $\hat{H}_{\mathbf{k}\cdot\mathbf{p}}$ of Eqs. 4.7 as

$$\hat{H}_{\mathbf{k}\cdot\mathbf{p}} = \frac{\hbar}{2m_0}(k_-\hat{p}_+ + k_+\hat{p}_-). \tag{4.10}$$

The corresponding matrix elements $\langle\psi_{\mu'}^\kappa s'|\hat{p}_\pm|\psi_\mu^\kappa s\rangle = \langle\psi_{\mu'}^\kappa|\hat{p}_\pm|\psi_\mu^\kappa\rangle\,\delta_{s',s}$ are constrained by the C_{3h} wavevector point group at K and K'. To find non-zero elements it is useful to consider the transformation of Bloch wavefunctions $\psi_\mu^\kappa(\mathbf{r})$ constructed with spherical orbitals $\phi_\mu^\kappa(\mathbf{r}) = d_m(\mathbf{r})$ under C_3 rotation:

$$\hat{U}_{C_3}\psi_\mu^\kappa(\mathbf{r}) = N^{-1/2}\sum_n \mathrm{e}^{\mathrm{i}\kappa\mathbf{K}\cdot(\mathbf{R}_n+\boldsymbol{\delta})} d_m\big(C_3^{-1}\mathbf{r}-\mathbf{R}_n-\boldsymbol{\delta}\big) \tag{4.11a}$$

$$= N^{-1/2}\sum_n \mathrm{e}^{\mathrm{i}\kappa(C_3\mathbf{K})\cdot[C_3(\mathbf{R}_n+\boldsymbol{\delta})]} d_m\big[C_3^{-1}\mathbf{r}-C_3^{-1}C_3(\mathbf{R}_n+\boldsymbol{\delta})\big] \tag{4.11b}$$

$$= N^{-1/2}\sum_n \mathrm{e}^{\mathrm{i}\kappa(C_3\mathbf{K})\cdot(\mathbf{R}_n+\boldsymbol{\delta})} d_m\big[C_3^{-1}(\mathbf{r}-\mathbf{R}_n-\boldsymbol{\delta})\big] \tag{4.11c}$$

$$= N^{-1/2}\mathrm{e}^{\mathrm{i}\kappa\mathbf{K}\cdot(C_3^{-1}\boldsymbol{\delta}-\boldsymbol{\delta})}\sum_n \mathrm{e}^{\mathrm{i}\kappa\mathbf{K}\cdot(\mathbf{R}_n+\boldsymbol{\delta})} d_m\big[C_3^{-1}(\mathbf{r}-\mathbf{R}_n-\boldsymbol{\delta})\big] \tag{4.11d}$$

$$= \eta_\delta\eta_m\psi_\mu^\kappa(\mathbf{r}). \tag{4.11e}$$

Here, the calculation steps are as follows. (4.11a) The C_3 symmetry operator $\hat{U}_{C_3}$ is applied on Eq. 4.8. The first step follows from $\hat{U}_{C_3}\psi_\mu^\kappa(\mathbf{r}) = \langle\mathbf{r}|\hat{U}_{C_3}|\psi_\mu^\kappa\rangle = \langle\hat{U}_{C_3}^\dagger\mathbf{r}|\psi_\mu^\kappa\rangle =$

$\langle C_3^{-1}\mathbf{r}|\psi_\mu^\kappa\rangle$, where we use that rotation operators and associated matrix representations are unitary with $C_3^\dagger = C_3^{-1}$. (4.11b) We use that the inner product of two vectors is invariant under unitary transformations, thus $\mathbf{k}\cdot\mathbf{r} = (C_3\mathbf{k})\cdot(C_3\mathbf{r})$, and we insert the identity matrix in the form of $C_3^{-1}C_3$. (4.11c) Summation over $C_3(\mathbf{R}_n+\boldsymbol{\delta})$ is replaced with $\mathbf{R}_n + \boldsymbol{\delta}$, which is the same for C_3 rotations centered around any atom site or the hollow center of any lattice hexagon. (4.11d) As C_3 is an element in the wavevector group of $\kappa\mathbf{K}$, we use that $\exp[\mathrm{i}\kappa(C_3\mathbf{K})\cdot\mathbf{R}_n] = \exp(\mathrm{i}\kappa\mathbf{K}\cdot\mathbf{R}_n)$, and furthermore we apply $(C_3\mathbf{k})\cdot\mathbf{r} = \mathbf{k}\cdot\big(C_3^{-1}\mathbf{r}\big)$. (4.11e) Finally, the parameters $\eta_\delta = \exp\big[\mathrm{i}\kappa\mathbf{K}\cdot\big(C_3^{-1}\boldsymbol{\delta}-\boldsymbol{\delta}\big)\big]$ and $\eta_m = \exp(-\mathrm{i}2\pi m/3)$ are introduced, which respectively describe the change of the lattice phase and the rotation of the spherical orbital around its own center [119]. The latter is obtained from

$$\hat{U}_{C_3} d_m(\mathbf{r}) = d_m\big(C_3^{-1}\mathbf{r}\big) = \exp\big(-\mathrm{i}\tfrac{2\pi}{3}m\big) d_m(\mathbf{r}) = \eta_m d_m(\mathbf{r}). \tag{4.12}$$

We proceed with the C_3 rotated complex momentum operator $\hat{p}_\pm$, which we characterize by the parameter $\eta_\pm = \exp(\mp\mathrm{i}2\pi/3)$. By using the form $\hat{p}_\pm = \boldsymbol{\alpha}_\pm\cdot\hat{\mathbf{p}}$ with $\boldsymbol{\alpha}_\pm = (1, \pm\mathrm{i}, 0)$, we obtain

$$\hat{U}_{C_3}\hat{p}_\pm\hat{U}_{C_3}^{-1} = \boldsymbol{\alpha}_\pm\cdot\hat{U}_{C_3}\hat{\mathbf{p}}\hat{U}_{C_3}^{-1} = \boldsymbol{\alpha}_\pm\cdot C_3^{-1}\hat{\mathbf{p}} = \exp\big(\mp\mathrm{i}\tfrac{2\pi}{3}\big)\hat{p}_\pm = \eta_\pm\hat{p}_\pm. \tag{4.13}$$

The transformations of Eqs. 4.11 and 4.13 imply that the non-zero elements of the $\mathbf{k}\cdot\mathbf{p}$ perturbation are off-diagonal, since:

$$\begin{aligned}
\langle\psi_{\mu'}^\kappa|\hat{p}_\pm|\psi_\mu^\kappa\rangle &= \langle\psi_{\mu'}^\kappa|\hat{U}_{C_3}^{-1}\hat{U}_{C_3}\hat{p}_\pm\hat{U}_{C_3}^{-1}\hat{U}_{C_3}|\psi_\mu^\kappa\rangle \\
&= \langle\hat{U}_{C_3}\psi_{\mu'}^\kappa|\hat{U}_{C_3}\hat{p}_\pm\hat{U}_{C_3}^{-1}|\hat{U}_{C_3}\psi_\mu^\kappa\rangle \\
&= \eta_\delta^*\eta_\delta\ \eta_{m'}^*\eta_m\ \eta_\pm\ \langle\psi_{\mu'}^\kappa|\hat{p}_\pm|\psi_\mu^\kappa\rangle \\
&= \exp\big[-\mathrm{i}\tfrac{2\pi}{3}(m-m'\pm1)\big]\ \langle\psi_{\mu'}^\kappa|\hat{p}_\pm|\psi_\mu^\kappa\rangle\,,
\end{aligned} \tag{4.14}$$

where m (m') is the magnetic quantum number of band μ (μ'). Clearly, the elements $\langle\psi_{\mu'}^\kappa|\hat{p}_\pm|\psi_\mu^\kappa\rangle$ can only be finite if $m - m' \pm 1 \bmod 3 = 0$. This is the case for $m' = 0$ and $m = 2\kappa$ with $\kappa = +1$ for $\hat{p}_+$ and $\kappa = -1$ for $\hat{p}_-$. The other alternative is $m' = 2\kappa$ and $m = 0$ with $\kappa = -1$ for $\hat{p}_+$ and $\kappa = +1$ for $\hat{p}_-$.

Continuing the symmetry analysis, we exploit that $|\psi_\mu^\kappa\rangle = \hat{\mathcal{K}}\,|\psi_\mu^{-\kappa}\rangle$, where $\hat{\mathcal{K}}$ is the complex conjugation operator, and establish:

$$\begin{aligned}
\langle\psi_{\mu'}^\kappa|\hat{H}_{\mathbf{k}\cdot\mathbf{p}}|\psi_\mu^\kappa\rangle &= \langle\hat{\mathcal{K}}\psi_{\mu'}^{-\kappa}|\hat{H}_{\mathbf{k}\cdot\mathbf{p}}|\hat{\mathcal{K}}\psi_\mu^{-\kappa}\rangle \\
&= -\,\langle\hat{\mathcal{K}}\psi_{\mu'}^{-\kappa}|\hat{\mathcal{K}}\hat{H}_{\mathbf{k}\cdot\mathbf{p}}\psi_\mu^{-\kappa}\rangle \\
&= -\big(\langle\psi_{\mu'}^{-\kappa}|\hat{H}_{\mathbf{k}\cdot\mathbf{p}}|\psi_\mu^{-\kappa}\rangle\big)^*.
\end{aligned} \tag{4.15}$$

Combining the above, the $\mathbf{k}\cdot\mathbf{p}$ perturbation of Eq. 4.10 is represented by the matrix

$$H_{\mathbf{k}\cdot\mathbf{p}} = \frac{\hbar}{4m_0}\begin{bmatrix} 0 & (\kappa+1)k_-\xi + (\kappa-1)k_+\xi^* \\ (\kappa+1)k_+\xi^* + (\kappa-1)k_-\xi & 0 \end{bmatrix}, \tag{4.16}$$

with the material parameter $\xi = \langle\psi_c^{+1}|\hat{p}_+|\psi_v^{+1}\rangle$. As a fitting variable, ξ has finite real values which can be obtained with ab initio density functional theory [114, 120]. Furthermore, ξ can be related to tight-binding models as $\xi = 2atm_0/\hbar$, where a is the lattice constant and t is the effective hopping integral between the d-orbitals of the transition metal atoms mediated by the p-orbitals of the chalcogen atoms [106, 121]. Using this, the form of Eq. 4.16 reduces to

$$H_{\mathbf{k}\cdot\mathbf{p}} = \begin{bmatrix} 0 & at(\kappa k_x - \mathrm{i}k_y) \\ at(\kappa k_x + \mathrm{i}k_y) & 0 \end{bmatrix}. \tag{4.17}$$

The non-zero matrix elements of the spin-orbit interaction can also be found by using the σ_h and C_3 symmetries of the system. For this we rewrite $\hat{H}_{\mathrm{so}}$ in Eqs. 4.7 as

$$\hat{H}_{\mathrm{so}} = \hat{\boldsymbol{\mathcal{B}}}\cdot\hat{\boldsymbol{\sigma}} = \hat{\mathcal{B}}_x\hat{\sigma}_x + \hat{\mathcal{B}}_y\hat{\sigma}_y + \hat{\mathcal{B}}_z\hat{\sigma}_z, \tag{4.18}$$

with $\hat{\boldsymbol{\mathcal{B}}} = \hbar(4m_0^2c^2)^{-1}\nabla V\times\hat{\mathbf{p}} = \left(\hat{\mathcal{B}}_x, \hat{\mathcal{B}}_y, \hat{\mathcal{B}}_z\right)$ representing the internal magnetic field of the system in units of half a Bohr magneton. In this notation, all matrix elements of the first two terms of Eq. 4.18 are zero for our basis functions. This is explained by the passive transformation of $\hat{\boldsymbol{\mathcal{B}}}$ generated by the σ_h symmetry operator $\hat{U}_{\sigma_h}^{-1}$:

$$\begin{aligned}\hat{U}_{\sigma_h}\hat{\boldsymbol{\mathcal{B}}}\hat{U}_{\sigma_h}^{-1} &= \hbar(4m_0^2c^2)^{-1}\left(\sigma_h^{-1}\nabla\right)V\times\left(\sigma_h^{-1}\hat{\mathbf{p}}\right)\\ &= \hbar(4m_0^2c^2)^{-1}\det\left(\sigma_h^{-1}\right)\sigma_h^{-1}(\nabla V\times\hat{\mathbf{p}})\\ &= \mathrm{diag}(-1,-1,+1)\hat{\boldsymbol{\mathcal{B}}}.\end{aligned} \tag{4.19}$$

Thus, the matrix elements involving $\hat{\mathcal{B}}_x$ and $\hat{\mathcal{B}}_y$ can only be finite between states with opposite σ_h parity. For our basis states, which are all even with respect to σ_h, only the last term of Eq. 4.18 yields non-zero elements:

$$\langle\psi_{\mu'}^{\kappa}s'|\hat{H}_{\mathrm{so}}|\psi_{\mu}^{\kappa}s\rangle = \langle\psi_{\mu'}^{\kappa}|\hat{\mathcal{B}}_z|\psi_{\mu}^{\kappa}\rangle\,\langle s'|\hat{\sigma}_z|s\rangle = \delta_{\mu',\mu}\delta_{s',s}s_z\,\langle\psi_{\mu}^{\kappa}|\hat{\mathcal{B}}_z|\psi_{\mu}^{\kappa}\rangle\,. \tag{4.20}$$

For the second equality sign we use that the spin space elements $\langle s'|\hat{\sigma}_z|s\rangle$ define the diagonal Pauli matrix for the eigenstates $|\uparrow\rangle$ and $|\downarrow\rangle$ with eigenvalues $s_z = +1$ and -1, respectively. Furthermore, we take into account that $\hat{\mathcal{B}}_z$ is invariant under C_3 transformation and is therefore diagonal for the basis $\{|\psi_c^{\kappa}\rangle, |\psi_v^{\kappa}\rangle\}$, as it only couples states with the same C_3 eigenvalues. This can be seen by establishing an identity analogous to Eq. 4.14.

To simplify the matrix elements of $\hat{\mathcal{B}}_z$, we use the atomic approximation [116]. Hereby only components from the spherical orbitals of transition metal atoms and the lattice potential residing on the same site are evaluated, and the rest is discarded:

$$\langle \psi_\mu^\kappa | \hat{\mathcal{B}}_z | \psi_\mu^\kappa \rangle \approx \lambda_\mu \langle \phi_\mu^\kappa | \hat{L}_z | \phi_\mu^\kappa \rangle / \hbar = \lambda_\mu \langle d_m | \hat{L}_z | d_m \rangle / \hbar = m\lambda_\mu. \tag{4.21}$$

Here, $\hat{L}_z$ is the z component of the angular momentum operator $\hat{\mathbf{L}} = \hat{\mathbf{r}} \times \hat{\mathbf{p}}$ and the parameter λ_μ quantifies the strength of the spin-orbit coupling in the band μ. Our two-band model can qualitatively reproduce a sizable spin splitting in the valence band, however it leaves the conduction band edge spin degenerate as $\langle \phi_c^\kappa | \hat{L}_z | \phi_c^\kappa \rangle = \langle d_0 | \hat{L}_z | d_0 \rangle = 0$. The origin of spin splitting in the conduction band partly lies in the off-diagonal coupling of the conduction band to remote bands constructed with $d_{\pm 1}$ transition metal orbitals, which are odd with respect to σ_h and therefore yield finite $\hat{\mathcal{B}}_x$ and $\hat{\mathcal{B}}_y$ matrix elements. Furthermore, the minor contribution of the chalcogen $p_{\mp 1}$ orbitals in the conduction band with $\kappa = \pm 1$ results in a spin splitting with an opposite sign as compared to the former second-order process [94, 106, 107]. Both effects have been neglected for simplicity and can be corrected with a phenomenological $\kappa s_z \lambda_c$ spin-orbit interaction term with the same symmetry-dictated form as found for the valence band [113, 122, 123]. The matrix representation of $\hat{H}_{\mathrm{so}}$ is then given by

$$H_{\mathrm{so}} = \begin{bmatrix} \kappa s_z \lambda_c & 0 \\ 0 & \kappa s_z \lambda_v \end{bmatrix}. \tag{4.22}$$

In summary, the matrix representation of the effective two-band Hamiltonian around the K and K' valleys (Eqs. 4.7) is given by the summation of the contributions in Eqs. 4.9, 4.17, and 4.22:

$$H_{\mathrm{eff}} = \begin{bmatrix} \Delta/2 + \kappa s_z \lambda_c & at(\kappa k_x - \mathrm{i}k_y) \\ at(\kappa k_x + \mathrm{i}k_y) & -\Delta/2 + \kappa s_z \lambda_v \end{bmatrix}. \tag{4.23}$$

This simple Hamiltonian, first proposed in Ref. 109 with $\lambda_c = 0$, describes massive Dirac fermions. As H_{eff} is fully diagonal in spin space, it governs the dynamics of the conduction and valence band edges with the same spin and cannot induce spin flips.

To finalize our two-band model, we solve Eq. 4.6 to obtain the eigenenergies $E_{\mu,s}^\kappa(\mathbf{k})$ and the eigenstates $\mathrm{e}^{-\mathrm{i}\mathbf{k}\cdot\mathbf{r}} |\Psi_{\mu,\mathbf{k},s}^\kappa\rangle$ of $\hat{H}_{\mathrm{eff}}$ in the vicinity of K and K'. The spin-dependent eigenenergies $E_{c,s}^\kappa(\mathbf{k})$ and $E_{v,s}^\kappa(\mathbf{k})$, which specify the dispersions of

the conduction and valence subbands for a given set of spin and valley indices, are given by

$$E^{\kappa}_{c,s}(\mathbf{k}) = \frac{1}{2}\left[\kappa s_z(\lambda_v + \lambda_c) + \sqrt{\Lambda^2 + 4a^2t^2k^2}\right], \tag{4.24a}$$

$$E^{\kappa}_{v,s}(\mathbf{k}) = \frac{1}{2}\left[\kappa s_z(\lambda_v + \lambda_c) - \sqrt{\Lambda^2 + 4a^2t^2k^2}\right], \tag{4.24b}$$

with the shorthands $\Lambda = \Delta - \kappa s_z(\lambda_v - \lambda_c)$ and $k^2 = k_x^2 + k_y^2$. The corresponding eigenstates are

$$\mathrm{e}^{-\mathrm{i}\mathbf{k}\cdot\mathbf{r}}\,|\Psi^{\kappa}_{c,\mathbf{k},s}\rangle = \mathcal{C}^{\kappa}_{c,s,c,s}(\mathbf{k})\,|\psi^{\kappa}_{c}s\rangle + \mathcal{C}^{\kappa}_{c,s,v,s}(\mathbf{k})\,|\psi^{\kappa}_{v}s\rangle = |u^{\kappa}_{c,\mathbf{k}}s\rangle\,, \tag{4.25a}$$

$$\mathrm{e}^{-\mathrm{i}\mathbf{k}\cdot\mathbf{r}}\,|\Psi^{\kappa}_{v,\mathbf{k},s}\rangle = \mathcal{C}^{\kappa}_{v,s,c,s}(\mathbf{k})\,|\psi^{\kappa}_{c}s\rangle + \mathcal{C}^{\kappa}_{v,s,v,s}(\mathbf{k})\,|\psi^{\kappa}_{v}s\rangle = |u^{\kappa}_{v,\mathbf{k}}s\rangle\,. \tag{4.25b}$$

As the effective Hamiltonian is diagonal in the spin basis $\{|\uparrow\rangle\,, |\downarrow\rangle\}$, all spin-mixing coefficients $\mathcal{C}^{\kappa}_{\mu',\uparrow,\mu,\downarrow}(\mathbf{k})$ and $\mathcal{C}^{\kappa}_{\mu',\downarrow,\mu,\uparrow}(\mathbf{k})$ are zero and $|u^{\kappa}_{\mu,\mathbf{k}}s\rangle = |u^{\kappa}_{\mu,\mathbf{k}}\rangle \otimes |s\rangle$. The eigenvectors $\boldsymbol{\mathcal{C}}^{\kappa}_{\mu,\mathbf{k},s}$ representing the states $|u^{\kappa}_{\mu,\mathbf{k}}s\rangle$ in the basis set defined by the unperturbed Hamiltonian matrix are then specified by

$$\boldsymbol{\mathcal{C}}^{\kappa}_{c,\mathbf{k},s} = \begin{bmatrix}\mathcal{C}^{\kappa}_{c,s,c,s}(\mathbf{k}) \\ \mathcal{C}^{\kappa}_{c,s,v,s}(\mathbf{k})\end{bmatrix} = \begin{bmatrix}\cos\dfrac{\vartheta}{2}\exp(-\mathrm{i}\kappa\varphi) \\ \sin\dfrac{\vartheta}{2}\end{bmatrix}, \tag{4.26a}$$

$$\boldsymbol{\mathcal{C}}^{\kappa}_{v,\mathbf{k},s} = \begin{bmatrix}\mathcal{C}^{\kappa}_{v,s,c,s}(\mathbf{k}) \\ \mathcal{C}^{\kappa}_{v,s,v,s}(\mathbf{k})\end{bmatrix} = \begin{bmatrix}\sin\dfrac{\vartheta}{2}\exp(-\mathrm{i}\kappa\varphi) \\ -\cos\dfrac{\vartheta}{2}\end{bmatrix}. \tag{4.26b}$$

Here, the azimuthal angle φ and polar angle ϑ are parametrized as

$$\varphi = \arctan\frac{k_y}{k_x} \quad \text{and} \quad \vartheta = \arccos\frac{\Lambda}{\sqrt{\Lambda^2 + 4a^2t^2k^2}}. \tag{4.27}$$

This two-band model is sufficient to explain some of the main valley-dependent features of monolayer TMDs, including the optical selection rules (Section 4.3), the Berry curvature, and the orbital magnetic moment (Section 4.4). Furthermore, it reveals the band dispersion with spin-orbit coupling and comparable magnitudes of the electron and hole effective masses. Because of this, the model laid the theoretical foundation for various related studies found in the literature [122, 124–127]. Some limitations of the presented theory, which can be overcome by more involved models, are the missing electron-hole asymmetry and trigonal warping of the bands [106, 114, 121].

4.3 Optical selection rules

Optical interband transitions in monolayer TMDs with non-central valleys are of a different origin as compared to conventional semiconductors like GaAs. Generally, both the magnetic moments from parent atomic orbitals of Bloch electrons (intracellular current) as well as the phase winding of the Bloch states at the K and K' points under rotational symmetry (intercellular current) need to be considered [128]. The latter contribution gives rise to valley-dependent optical selection rules, which are discussed in the following.

In a semi-classical approach to absorption or stimulated emission, the interband transition probability per unit time and unit volume (i.e. transition rate) of an electron (with charge $-e$) from the subband μ, s to a different subband μ', s' can be approximated by Fermi's golden rule. The transition rate for spontaneous emission is interrelated to the other two processes and can be expressed in terms of Einstein's coefficients. In the following we treat the absorption case for an incident radiation field with angular frequency ω, unit polarization vector $\boldsymbol{\epsilon}$, and vector potential amplitude maximum A_0. We assume the validity of the electric dipole approximation, where the wavelength of the radiation field is much longer than the lattice constant, and thus consider only vertical transitions in reciprocal space. The initial and final states within our two-band model (Section 4.2) are described by $|\Psi^{\kappa}_{v,\mathbf{k},s}\rangle$ and $|\Psi^{\kappa}_{c,\mathbf{k},s'}\rangle$, respectively (Eqs. 4.25). With this in mind, the absorption rate can be written as [129, 130]:

$$\mathcal{W}^{\kappa}_{vs\to cs'} = \frac{2\pi}{\hbar}\frac{e^2}{4m_0^2}|A_0|^2 \sum_{\mathbf{k}} \left|\boldsymbol{\epsilon}\cdot\boldsymbol{\mathcal{P}}^{\kappa}_{cs',vs}(\mathbf{k})\right|^2 \delta\left[E^{\kappa}_{c,s'}(\mathbf{k}) - E^{\kappa}_{v,s}(\mathbf{k}) - \hbar\omega\right], \tag{4.28}$$

where the matrix element $\boldsymbol{\mathcal{P}}^{\kappa}_{cs',vs}(\mathbf{k})$ is given by

$$\boldsymbol{\mathcal{P}}^{\kappa}_{cs',vs}(\mathbf{k}) = \langle \Psi^{\kappa}_{c,\mathbf{k},s'}|\hat{\boldsymbol{\pi}}|\Psi^{\kappa}_{v,\mathbf{k},s}\rangle\,, \tag{4.29}$$

with the pseudomomentum operator $\hat{\boldsymbol{\pi}} = \hat{\mathbf{p}} + \hbar(4m_0c^2)^{-1}\hat{\boldsymbol{\sigma}}\times\nabla V$. Using the commutation relation $\hat{\boldsymbol{\pi}} = \mathrm{i}m_0\hbar^{-1}\left[\hat{H},\hat{\mathbf{r}}\right]$ between the Hamiltonian (Eq. 4.4) and the position operator $\hat{\mathbf{r}}$, an equivalent electric dipole approximation form of Eq. 4.29 can be obtained:

$$\begin{aligned}
\boldsymbol{\mathcal{P}}^{\kappa}_{cs',vs}(\mathbf{k}) &= \mathrm{i}\frac{m_0}{\hbar}\langle \Psi^{\kappa}_{c,\mathbf{k},s'}|\left[\hat{H},\hat{\mathbf{r}}\right]|\Psi^{\kappa}_{v,\mathbf{k},s}\rangle \\
&= \mathrm{i}\frac{m_0}{\hbar}\left(\langle \hat{H}\Psi^{\kappa}_{c,\mathbf{k},s'}|\hat{\mathbf{r}}|\Psi^{\kappa}_{v,\mathbf{k},s}\rangle - \langle \Psi^{\kappa}_{c,\mathbf{k},s'}|\hat{\mathbf{r}}|\hat{H}\Psi^{\kappa}_{v,\mathbf{k},s}\rangle\right) \\
&= \mathrm{i}\frac{m_0}{\hbar}\left[E^{\kappa}_{c,s'}(\mathbf{k}) - E^{\kappa}_{v,s}(\mathbf{k})\right]\langle \Psi^{\kappa}_{c,\mathbf{k},s'}|\hat{\mathbf{r}}|\Psi^{\kappa}_{v,\mathbf{k},s}\rangle \\
&= \mathrm{i}\frac{m_0}{\hbar}\left[E^{\kappa}_{c,s}(\mathbf{k}) - E^{\kappa}_{v,s}(\mathbf{k})\right]\langle \Psi^{\kappa}_{c,\mathbf{k},s}|\hat{\mathbf{r}}|\Psi^{\kappa}_{v,\mathbf{k},s}\rangle\,\delta_{s',s}.
\end{aligned} \tag{4.30}$$

This form of the electron-radiation interaction does not contain spin operators, meaning that optical transitions are only allowed between orbital parts with the same spin state. The subbands described by the two-band model are eigenstates of $\hat{\sigma}_z$ and therefore conserve the z-spin orientation during transition processes, which is reflected by the Kronecker delta $\delta_{s',s}$ in Eq. 4.30.

At first we consider the transition rate of an electron from a valence subband to a conduction subband for the absorption of a $\sigma^{\pm}$ photon propagating along the $+z$ direction with $\boldsymbol{\epsilon} = (1, \pm\mathrm{i}, 0)/\sqrt{2} = \boldsymbol{\epsilon}_{\pm}$. Strictly at K or K' the transition rate is then quantified by $\boldsymbol{\epsilon}_{\pm} \cdot \boldsymbol{\mathcal{P}}^{\kappa}_{cs',vs}(0) \propto \langle \psi^{\kappa}_{c} | \boldsymbol{\epsilon}_{\pm} \cdot \hat{\mathbf{r}} | \psi^{\kappa}_{v} \rangle \, \delta_{s',s}$. Noting the identity of Eq. 4.14 and that $\boldsymbol{\epsilon}_{\pm} \cdot \hat{\mathbf{r}}$ transforms the same way as $\hat{p}_{\pm}$ under C_3 rotation, it is clear that this transition is allowed only if $2\kappa \pm 1 \bmod 3 = 0$, which defines the chiral optical selection rules in TMD monolayers. This means that optical σ^+ and σ^- fields propagating along $+z$ only couple to the K ($\kappa = +1$) and K' ($\kappa = -1$) points, respectively. This assignment is reversed for photons traveling along $-z$ as photons of opposite helicity and momentum have the same polarization vector. In the experiment we consider all photons to be outgoing and therefore label incoming photons by the opposite helicity.

Near the K and K' points the coupling strength to optical fields can be calculated using the momentum space representation $\hat{\mathbf{r}} = \mathrm{i}\nabla_{\mathbf{k}}$ of the position operator. With Eqs. 4.25 to 4.27, we obtain

$$\langle \Psi^{\kappa}_{c,\mathbf{k},s} | \hat{\mathbf{r}} | \Psi^{\kappa}_{v,\mathbf{k},s} \rangle = \mathrm{i}\Big\{ \Big[\big(\boldsymbol{\mathcal{C}}^{\kappa}_{c,\mathbf{k},s}\big)^{\dagger} \partial_{\varphi} \boldsymbol{\mathcal{C}}^{\kappa}_{v,\mathbf{k},s} \Big] \nabla_{\mathbf{k}} \varphi + \Big[\big(\boldsymbol{\mathcal{C}}^{\kappa}_{c,\mathbf{k},s}\big)^{\dagger} \partial_{\vartheta} \boldsymbol{\mathcal{C}}^{\kappa}_{v,\mathbf{k},s} \Big] \nabla_{\mathbf{k}} \vartheta \Big\}, \tag{4.31}$$

with the explicitly calculated contributions

$$\big(\boldsymbol{\mathcal{C}}^{\kappa}_{c,\mathbf{k},s}\big)^{\dagger} \partial_{\varphi} \boldsymbol{\mathcal{C}}^{\kappa}_{v,\mathbf{k},s} = -\mathrm{i}\kappa \frac{at|k|}{\sqrt{\Lambda^2 + 4a^2t^2k^2}}, \qquad \nabla_{\mathbf{k}} \varphi = \boldsymbol{\epsilon}_z \times \mathbf{k}/k^2, \tag{4.32a}$$

$$\big(\boldsymbol{\mathcal{C}}^{\kappa}_{c,\mathbf{k},s}\big)^{\dagger} \partial_{\vartheta} \boldsymbol{\mathcal{C}}^{\kappa}_{v,\mathbf{k},s} = \frac{1}{2}, \qquad \nabla_{\mathbf{k}} \vartheta = \frac{2at\Lambda}{\Lambda^2 + 4a^2t^2k^2} \boldsymbol{\epsilon}_k, \tag{4.32b}$$

where $\boldsymbol{\epsilon}_z = (0, 0, 1)$ and $\boldsymbol{\epsilon}_k = (k_x, k_y, 0)/|k|$. With this the absolute square of the wavevector-resolved matrix element entering the absorption rate in Eq. 4.28 for $\sigma^{\pm}$ ($\sigma^{\mp}$) photons traveling along $+z$ ($-z$) is given by the simple expression [109]:

$$\big| \boldsymbol{\epsilon}_{\pm} \cdot \boldsymbol{\mathcal{P}}^{\kappa}_{cs,vs}(\mathbf{k}) \big|^2 = \frac{m_0^2 a^2 t^2}{2\hbar^2} \left(1 \pm \kappa \frac{\Lambda}{\sqrt{\Lambda^2 + 4a^2t^2k^2}} \right)^2 = \big| \mathcal{P}^{\kappa,\pm}_{cs,vs}(\mathbf{k}) \big|^2. \tag{4.33}$$

Within the validity of the two-band $\mathbf{k}\cdot\mathbf{p}$ model with $\Lambda \gg at|k|$, the valley-dependent selection rules also uphold in the vicinity of the K and K' points. In fact, first-principles calculations show that chiral absorption selectivity remains close to perfect for the entire valleys and only exhibits rapid sign change across the valley bound-

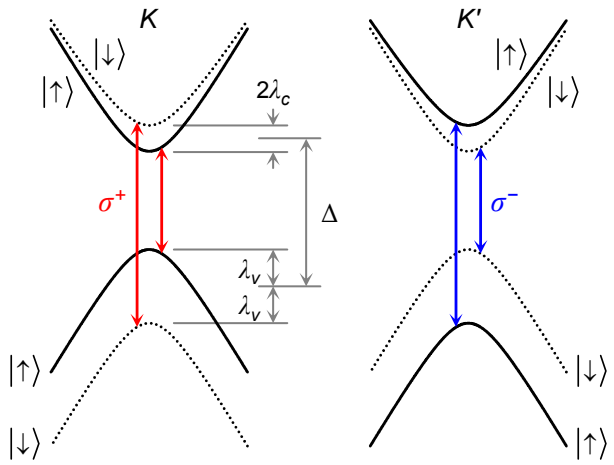

Figure 4.2: Valley- and spin-dependent optical selection rules for monolayer MoS_2, as a representative two-dimensional transition metal dichalcogenide. The solid and dotted curves respectively represent the band edge dispersions of the spin ↑ and ↓ subbands quantized along the out-of-plane $+z$ direction. Interband transitions denoted by the red (blue) arrows for σ^+ (σ^-) photons propagating along the spin quantization axis are coupled exclusively to the K (K') valley. Relevant energies (Δ, λ_c, and λ_v) are not to scale and labeled in accordance with the two-band model of Section 4.2.

aries [131]. Since the spin-split bands at K and K' are time-reversals of each other, the selection rules are also inherently spin-dependent as schematically illustrated in Fig. 4.2. This optical interface to the valley pseudospin allows to selectively generate valley polarization and detect it upon recombination of the photocarriers [131–133].

It is straight forward to extend our analysis for absorption of radiation with an arbitrary polarization and propagation direction. For example, linearly polarized light traveling along the z axis will simultaneously excite both the K and K' valleys since the radiation can be considered as a coherent superposition of σ^+ and σ^- photon beams. The optical coherence will then induce valley coherence in the form of photocarrier pairs in a linear superposition at the K and K' valleys [134]. As for radiation fields with in-plane wavevectors, only the in-plane polarization components will couple to the valley subbands of our two-band model. This is owed to the oddness of $\boldsymbol{\epsilon}_z \cdot \hat{\mathbf{r}}$ and the evenness of the involved orbital states of the system under σ_h reflection. However, in a more complete model the subbands are no longer pure z-spin states and generally include minor contributions from direct products of opposite spin states and remote odd orbital states. Consequently, nominally spin-forbidden interband transitions become weakly allowed for z-polarized radiation, as the odd dipole operator $\boldsymbol{\epsilon}_z \cdot \hat{\mathbf{r}}$ couples orbital states with opposite σ_h parity [135]. Interestingly, at the K and K' points group theory dictates that such dark dipolar transitions from the lower valence subbands must remain strictly forbidden [136].

4.4 Berry curvature and valley Zeeman effect

Upon adiabatic evolution where external parameters are slowly changed in a closed loop, an eigenstate of a quantum system acquires a phase, known as the Berry phase [137], which is a gauge-invariant physical quantity. The associated Berry curvature for a three dimensional parameter space is defined as a gauge field vector in analogy to electrodynamics and a closed loop is no longer necessary. As a gauge-invariant quantity and therefore an observable of the system, the Berry curvature is essential to describe Bloch electrons [138]. It is an intrinsic property of the band structure and finite for crystals without time-reversal symmetry or inversion symmetry. For Bloch electrons with lattice-periodic states $|u_{\nu,\mathbf{q}}\rangle$ the Berry curvature is defined by [138]:

$$\mathbf{\Omega}_\nu(\mathbf{q}) = \nabla_\mathbf{q} \times \langle u_{\nu,\mathbf{q}} | \mathrm{i}\nabla_\mathbf{q} | u_{\nu,\mathbf{q}} \rangle \,. \tag{4.34}$$

From this definition it can be shown that the presence of time-reversal symmetry imposes the restriction

$$\mathbf{\Omega}_\nu(-\mathbf{q}) = -\mathbf{\Omega}_\nu(\mathbf{q}), \tag{4.35}$$

and spatial inversion symmetry requires that

$$\mathbf{\Omega}_\nu(-\mathbf{q}) = \mathbf{\Omega}_\nu(\mathbf{q}). \tag{4.36}$$

As a consequence, the Berry curvature must vanish for all $\mathbf{q}$ in systems with both symmetries.

The Berry curvature can be understood as a magnetic field in momentum space and therefore influences the dynamics of Bloch electrons. For example in the presence of an electric field, electrons acquire an anomalous velocity proportional to the Berry curvature of their subband. In general, the semi-classical transport dynamics of adiabatically moving Bloch electrons confined within a single subband ν can be treated as a narrow wavepacket with real and reciprocal space dimensions much smaller than the lattice constant and the size of Brillouin zone, respectively. In analogy to spin, the wavepacket may self-rotate around its center of mass and therefore posses an orbital magnetic moment given by [139]:

$$\mathbf{M}_\nu(\mathbf{q}) = -\mathrm{i}\frac{e}{2\hbar} \langle \nabla_\mathbf{q} u_{\nu,\mathbf{q}} | \times \left[\mathrm{e}^{-\mathrm{i}\mathbf{q}\cdot\mathbf{r}} \hat{H} \mathrm{e}^{\mathrm{i}\mathbf{q}\cdot\mathbf{r}} - E_\nu(\mathbf{k}) \right] | \nabla_\mathbf{q} u_{\nu,\mathbf{q}} \rangle \,, \tag{4.37}$$

where $|u_{\nu,\mathbf{q}}\rangle$ is an eigenstate of the transformed Hamiltonian $\mathrm{e}^{-\mathrm{i}\mathbf{q}\cdot\mathbf{r}} \hat{H} \mathrm{e}^{\mathrm{i}\mathbf{q}\cdot\mathbf{r}}$ with the eigenenergy $E_\nu(\mathbf{k})$. It is worth mentioning that the orbital magnetic moment has the same properties as the Berry curvature under time-reversal and spatial inversion symmetry, and in many cases it can be significantly larger than the spin moment [140]. Together with the Berry curvature, the orbital magnetic moment characterizes the effect of the Berry phase of Bloch electrons.

Within the formalism of the symmetry-based two-band model of Section 4.2, one can write the Berry curvature for the subband μ, s around the K or K' point with valley index κ of a TMD monolayer as

$$\mathbf{\Omega}^{\kappa}_{\mu,s}(\mathbf{k}) = \nabla_{\mathbf{k}} \times \langle u^{\kappa}_{\mu,\mathbf{k}} s | \mathrm{i}\nabla_{\mathbf{k}} | u^{\kappa}_{\mu,\mathbf{k}} s \rangle \,. \tag{4.38}$$

For two-dimensional crystals only the Berry curvature z component of the conduction and valence subbands is non-zero and can be written as [128, 139]:

$$\left[\mathbf{\Omega}^{\kappa}_{c,s}(\mathbf{k})\right]_z = -\frac{\hbar^2}{m_0^2} \frac{\left|\mathcal{P}^{\kappa,+}_{cs,vs}(\mathbf{k})\right|^2 - \left|\mathcal{P}^{\kappa,-}_{cs,vs}(\mathbf{k})\right|^2}{\left[E^{\kappa}_{v,s}(\mathbf{k}) - E^{\kappa}_{c,s}(\mathbf{k})\right]^2} = -\left[\mathbf{\Omega}^{\kappa}_{v,s}(\mathbf{k})\right]_z . \tag{4.39}$$

With Eqs. 4.24 and 4.33, the following analytic expression can be obtained:

$$\left[\mathbf{\Omega}^{\kappa}_{c,s}(\mathbf{k})\right]_z = -\kappa \frac{2a^2t^2\Lambda}{\left(\Lambda^2 + 4a^2t^2k^2\right)^{3/2}} = -\left[\mathbf{\Omega}^{\kappa}_{v,s}(\mathbf{k})\right]_z . \tag{4.40}$$

In the same spirit the orbital magnetic moment of the subband μ, s of our symmetry-based model is given by

$$\mathbf{M}^{\kappa}_{\mu,s}(\mathbf{k}) = -\mathrm{i}\frac{e}{2\hbar} \langle \nabla_{\mathbf{k}} u^{\kappa}_{\mu,\mathbf{k}} s | \times \left[\hat{H}_{\mathrm{eff}} - E^{\kappa}_{\mu,s}(\mathbf{k})\right] | \nabla_{\mathbf{k}} u^{\kappa}_{\mu,\mathbf{k}} s \rangle \,, \tag{4.41}$$

where in analogy to the Berry curvature only the z component is finite [128, 139]:

$$\left[\mathbf{M}^{\kappa}_{c,s}(\mathbf{k})\right]_z = \frac{e\hbar}{2m_0^2} \frac{\left|\mathcal{P}^{\kappa,+}_{cs,vs}(\mathbf{k})\right|^2 - \left|\mathcal{P}^{\kappa,-}_{cs,vs}(\mathbf{k})\right|^2}{E^{\kappa}_{v,s}(\mathbf{k}) - E^{\kappa}_{c,s}(\mathbf{k})} = \left[\mathbf{M}^{\kappa}_{v,s}(\mathbf{k})\right]_z . \tag{4.42}$$

Thus, we obtain the expression

$$\left[\mathbf{M}^{\kappa}_{c,s}(\mathbf{k})\right]_z = -\kappa \frac{ea^2t^2\Lambda}{\hbar\left(\Lambda^2 + 4a^2t^2k^2\right)} = \left[\mathbf{M}^{\kappa}_{v,s}(\mathbf{k})\right]_z , \tag{4.43}$$

which quantifies the orbital magnetic moment of the two-band approximation with its peak value at $k = 0$ given by $\left[\mathbf{M}^{\kappa}_{\mu,s}(0)\right]_z = -\kappa e a^2 t^2/(\hbar\Lambda) = \kappa M^{\mathrm{orb}}_{\mu,s}$.

It is evident that the Berry curvatures as well as the orbital magnetic moments of the Bloch subbands are inherently connected to the valley-contrasting circular dichroism described in Section 4.3. Furthermore, the valley-contrasting Berry curvatures also signify that in an in-plane electric field charge carriers in K and K' will accumulate at opposite transverse boundaries of the sample [109, 128, 140]. This valley Hall effect is closely related to the spin Hall effect, only with spins replaced by valley pseudospins, and was experimentally verified for MoS_2 monolayer devices [27]. As the Berry curvatures in the conduction and valence subbands have opposite signs for a given valley, electron and hole doped systems also exhibit a sign reversal

to the valley Hall effect, which is moreover accompanied by a spin Hall effect for both types of charge carriers [109].

In an out-of-plane external magnetic field B_z the orbital magnetic moment and also the z-spin magnetic moment will induce a Zeeman shift in the K and K' valleys [141]. As both magnetic moments for a given subband in K and K' are identical in magnitude but opposite in sign, an applied field B_z will break the time-reversal symmetry of the electronic states in the two valleys. The lifted degeneracy can be measured in magneto-optical experiments as a linear splitting of optical interband resonances as was first observed in the selenide monolayers [142–145], followed by the sulfide [146] and $MoTe_2$ monolayers [147]. A needed requirement for this valley Zeeman effect is the generally asymmetric orbital magnetic moments in the conduction and valence subbands with the same spin index and valley pseudospin κ, which yield unequal energy shifts $\kappa\Delta_c^{\mathrm{orb}}$ and $\kappa\Delta_v^{\mathrm{orb}}$, respectively. The Zeeman shift due to the spin magnetic moment ($\kappa\Delta^{\mathrm{spin}}$) does not contribute to the splitting as spin is conserved in optical transitions, and has the same effect on the initial and final states. Accordingly, the valley Zeeman splitting (Δ_{VZ}), defined as the energy difference between optical interband resonances at K and K', can be quantified with an effective g-factor (g_{VZ}) as

$$\Delta_{\mathrm{VZ}} = 2\big(\Delta_c^{\mathrm{orb}} - \Delta_v^{\mathrm{orb}}\big) = g_{\mathrm{VZ}}\mu_{\mathrm{B}}B_z, \tag{4.44}$$

where $\mu_{\mathrm{B}} = e\hbar/(2m_0)$ is the Bohr magneton.

For our two-band model the net Zeeman shift Δ_{VZ} must vanish since $\Delta_c^{\mathrm{orb}} = -M_{c,s}B_z$ and $\Delta_v^{\mathrm{orb}} = -M_{v,s}B_z$ are the same as is evident from Eq. 4.43. This clearly contradicts the experimentally observed $g_{\mathrm{VZ}} \approx -4$ associated with optical recombination of band-edge excitons [142–145]. Coulomb renormalization effects alone cannot explain this discrepancy, which is in fact a generic shortcoming of two-band approximations [148, 149] even in the presence of effective mass asymmetry terms [150]. However, in a six-band $\mathbf{k}\cdot\mathbf{p}$ model coupling to the remote second upper conduction and third lower valence band can provide asymmetric orbital magnetic moments which yield g_{VZ} values in reasonable agreement with the experimental observations [149].

Alternatively, an intuitive estimation of g_{VZ} can be obtained by decomposing the orbital magnetic moments along z in the conduction and valence bands into their respective intercellular and intracellular components [142–145]. The Zeeman shift arising from the intercellular current circulations for the valley κ is determined by $\kappa\Delta_\mu^{\mathrm{inter}}$ with $\Delta_\mu^{\mathrm{inter}} = \mu_{\mathrm{B}}B_z m_0/|m_\mu^*|$, where m_μ^* is the effective mass of the band μ (we neglect the spin index). Since the effective masses in both bands are similar, this contribution does not greatly affect g_{VZ}. In contrast, the absolute shift owed

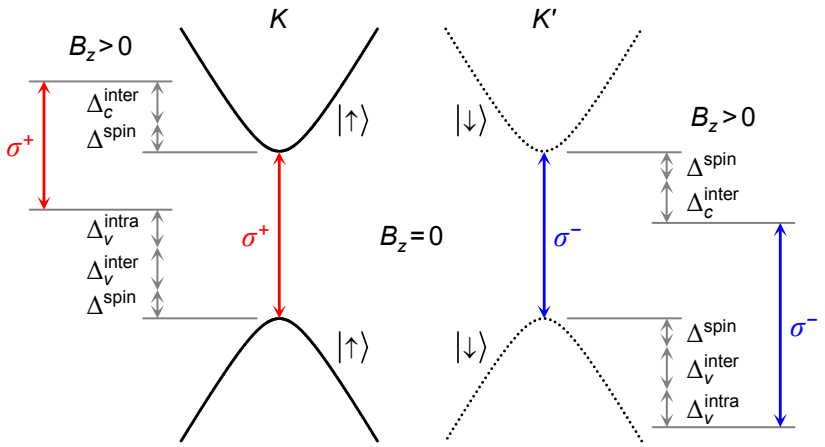

Figure 4.3: Valley Zeeman effect in a monolayer transition metal dichalcogenide for out-of-plane magnetic fields B_z. The schematic shows dipole allowed optical transitions from and to the upper valence subband in K (spin $\uparrow$) and K' (spin $\downarrow$), which couple to σ^+ and σ^- photons, respectively. For finite fields B_z the degeneracy of the valleys is lifted owed to opposite Zeeman shifts in the two valleys with unequal contributions for the valence and conduction subbands. The magnitude of the energy shift for the valence subband is determined by contributions from the intracellular and intercellular orbital, as well as the bare spin magnetic moments (Δ_v^{intra}, Δ_v^{inter}, and Δ^{spin}, respectively). For the conduction subband, primarily constructed with d_{z^2} orbitals, the intracellular magnetic moment is approximately zero and the contribution from the intercellular magnetic moment (Δ_c^{inter}) is different as a result of the electron-hole asymmetry.

to the intracellular magnetic moment from the multiorbital nature of the bands is not symmetric and approximated by $\kappa\Delta_\mu^{\text{intra}} \approx \mu_{\text{B}} B_z m$, where m is the magnetic quantum number of the dominant basis orbitals of the bulk band μ (Eqs. 4.1). While the d_0 orbitals of the conduction band provide $\Delta_c^{\text{intra}} \approx 0$, the intracellular current circulation of valence band electrons primarily stems from $d_{2\kappa}$ orbitals and contributes $\Delta_v^{\text{intra}} \approx 2\mu_{\text{B}} B_z$. With this, the valley Zeeman splitting, calculated as

$$\Delta_{\text{VZ}} = 2\big(\Delta_c^{\text{inter}} - \Delta_v^{\text{inter}} + \Delta_c^{\text{intra}} - \Delta_v^{\text{intra}}\big) \approx 2\Big(\frac{m_0}{|m_c^*|} - \frac{m_0}{|m_v^*|} - 2\Big)\mu_{\text{B}} B_z, \tag{4.45}$$

then yields $g_{\text{VZ}} \approx -4$ if m_c^* and m_v^* are the same in magnitude. An illustration describing the valley Zeeman effect within this simple approach is provided in Fig. 4.3.

4.5 Excitonic effects

To this end we have neglected Coulomb interaction between photoexcited charge carriers. If this interaction is included bound excitonic states arise, which renormalize

the optical band gap. In two-dimensional materials excitonic effects are especially strong owed to enhancement by weak screening and the relatively large effective masses [151]. Below we discuss the simple case of an electron-hole pair formed by conduction and valence band states around the K and K' valleys. These bound pairs are commonly referred to as A (B) excitons if the hole is in the upper (lower) valence subband.

Within the framework of the two-band model of Section 4.2, the exciton basis states can be represented as a linear combination of excited states of the system [129, 152]:

$$\sum_{\mathbf{k}_e,\mathbf{k}_h} \mathcal{A}^{n,\mathbf{Q}}_{s_e,\kappa_e,s_h,\kappa_h}(\mathbf{k}_e,\mathbf{k}_h) \left| \Psi^{\kappa_e}_{c,\mathbf{k}_e,s_e} \Psi^{\kappa_h}_{v,\mathbf{k}_h,s_h} \right\rangle , \tag{4.46}$$

where the coordinate representation of the two-particle excited state with an electron in the conduction band and a hole in the valence band is given by

$$\left\langle \mathbf{r}_e\mathbf{r}_h \right| \Psi^{\kappa_e}_{c,\mathbf{k}_e,s_e} \Psi^{\kappa_h}_{v,\mathbf{k}_h,s_h} \Big\rangle = \Psi^{\kappa_e}_{c,\mathbf{k}_e,s_e}(\mathbf{r}_e) \Psi^{\kappa_h}_{v,\mathbf{k}_h,s_h}(\mathbf{r}_h). \tag{4.47}$$

Here, the subscripts e and h respectively denote electron and hole representations, and the coordinates $\mathbf{r}_e$ and $\mathbf{r}_h$ are taken to include the spin coordinates. Apart from the spin indices (s_e, s_h) and the valley indices (κ_e, κ_h), excitons states are labeled by the envelope index n and the total exciton wavevector $\mathbf{Q} = \mathbf{k}_e + \mathbf{k}_h - (\kappa_e + \kappa_h)\mathbf{K}/2$ found in the expansion coefficients $\mathcal{A}^{n,\mathbf{Q}}_{s_e,\kappa_e,s_h,\kappa_h}(\mathbf{k}_e,\mathbf{k}_h)$. The electron representation is $\Psi^{\kappa_e}_{c,\mathbf{k}_e,s_e}(\mathbf{r}_e) = \Psi^{\kappa}_{c,\mathbf{k},s}(\mathbf{r}_h)$ and the hole representation is defined by $\Psi^{\kappa_h}_{v,\mathbf{k}_h,s_h}(\mathbf{r}_h) = \hat{\mathcal{T}}\Psi^{\kappa}_{v,\mathbf{k},s}(\mathbf{r}_h)$ with the time-reversal operator $\hat{\mathcal{T}} = \hat{\mathcal{K}}\hat{\sigma}_y$. This convention means that for momentum-direct excitons we have $\kappa_e = -\kappa_h$ and $\mathbf{k}_e = -\mathbf{k}_h$, and that for optically bright excitons coupled to light under normal incidence spin $\downarrow_h$ ($\uparrow_h$) holes describe the absence of spin $\uparrow_e$ ($\downarrow_e$) electrons.

Using the effective mass theory for excitons and with neglected band mixing [129], the binding energies $E^n_X(\mathbf{Q})$ of the exciton states $X = \{s_e, \kappa_e, s_h, \kappa_h\}$ are obtained from the differential equation

$$\left(-\frac{\hbar^2\nabla_e^2}{2m_e^*} - \frac{\hbar^2\nabla_h^2}{2m_h^*} - \frac{e^2}{4\pi\epsilon_0\epsilon|\mathbf{r}_e - \mathbf{r}_h|} \right) \Phi^{n,\mathbf{Q}}_X(\mathbf{r}_e,\mathbf{r}_h) = E^n_X(\mathbf{Q}) \Phi^{n,\mathbf{Q}}_X(\mathbf{r}_e,\mathbf{r}_h), \tag{4.48}$$

with the vacuum permittivity ϵ_0, the effective dielectric constant ϵ, the effective electron (hole) mass $m_e^* = m_c^*$ ($m_h^* = -m_v^*$), and the real-space envelope functions

$$\Phi^{n,\mathbf{Q}}_X(\mathbf{r}_e,\mathbf{r}_h) = \mathcal{V}^{-1} \sum_{\mathbf{k}_e,\mathbf{k}_h} \mathrm{e}^{\mathrm{i}\mathbf{k}_e\cdot\mathbf{r}_e} \mathrm{e}^{\mathrm{i}\mathbf{k}_h\cdot\mathbf{r}_h} \mathcal{A}^{n,\mathbf{Q}}_{s_e,\kappa_e,s_h,\kappa_h}(\mathbf{k}_e,\mathbf{k}_h), \tag{4.49}$$

where $\mathcal{V}$ is the crystal volume. For TMD monolayers $\epsilon = \epsilon(\mathbf{r}_e, \mathbf{r}_h)$ is non-local and strongly dependent on the electron and hole separation of the exciton state [153]. To obtain a simple estimate for the exciton binding energies we assume a constant background dielectric constant of $\epsilon \approx 5$, which is in agreement with the monolayer being on top of a substrate with a static dielectric constant of $\sim$ 10. Then by considering only in-plane motion of the charge carriers, Eq. 4.49 yields the Rydberg series of the two-dimensional hydrogen model [154], complemented by the center of mass kinetic energy of the exciton:

$$E_X^n(\mathbf{Q}) = \frac{\hbar^2 \mathbf{Q}^2}{2(m_e^* + m_h^*)} - \frac{e^4}{32\pi^2\hbar^2\epsilon_0^2\epsilon^2(n-1/2)^2} \frac{m_e^* m_h^*}{m_e^* + m_h^*}. \tag{4.50}$$

For similar electron and hole effective masses of $\sim 0.5 m_0$, the ground state binding energy is roughly $E_X^1(0) \approx -0.5$ eV, which greatly exceeds those found for conventional two-dimensional semiconductors based on GaAs. This value agrees in order of magnitude with the reported experiments [15–19], and clearly shows that robust excitons that are stable at room temperature dominate the photophysics in TMD monolayers. Even though the binding energies are comparable to typical Frenkel excitons, ab initio calculations show that the exciton wavefunctions extend over several unit cells and yield a Bohr radius of $\sim$ 1 nm for the lowest state [17, 155]. Thus, the wavefunctions are largely of the Wannier-Mott character, which justifies the effective mass approximation of Eq. 4.48.

Chapter 5

Opto-valleytronic imaging of two-dimensional semiconductors

This chapter is based on the original publication P2:
A. Neumann, J. Lindlau, L. Colombier, M. Nutz, S. Najmaei, J. Lou, A. D. Mohite, H. Yamaguchi, and A. Högele. *Opto-valleytronic imaging of atomically thin semiconductors.* Nat. Nanotechnol. **12**, 329–334 (2017).

Transition metal dichalcogenide semiconductors represent elementary components of layered heterostructures for emergent technologies beyond conventional opto-electronics. In their monolayer form they host electrons with quantized circular motion and associated valley polarization and valley coherence as key elements of opto-valleytronic functionality. This chapter introduces two-dimensional polarimetry as means of direct imaging of the valley pseudospin degree of freedom in monolayer transition metal dichalcogenides. Using molybdenum disulfide as a representative material with valley-selective optical transitions, we establish quantitative image analysis for polarimetric maps of extended crystals, and identify valley polarization and valley coherence as sensitive probes of crystalline disorder. Moreover, we find site-dependent thermal and non-thermal regimes of valley-polarized excitons in perpendicular magnetic fields. Finally, we demonstrate the potential of wide-field polarimetry for rapid inspection of opto-valleytronic devices based on atomically thin semiconductors and heterostructures.

5.1 Introduction and overview of the experiment

The valley quantum degree of freedom manifests itself as the quantized angular motion of crystal electrons near the band edges. In analogy to spin it represents a resource for quantum information in conventional semiconductors such as aluminum arsenide [156] and silicon [157], or in atomically thin materials including graphene [158] and TMDs [25, 109]. Direct band gap monolayer TMDs [9, 10] are particularly viable for practical realizations of valleytronic concepts as they enable initialization [109], manipulation [159], and detection [131–133] of the valley pseudospin by all-optical means. Despite successful realization of first opto-valleytronic devices [27, 28], controversy prevails with respect to possible intrinsic and extrinsic origins of significant variations in the degrees of valley polarization [131–133, 160, 161] and valley coherence [134, 162] observed for different material representatives of monolayer TMD semiconductors.

The valley pseudospin in TMDs is most conveniently accessed with PL polarimetry of band-edge excitons [25]. The degrees of circular and linear PL polarization, P_c and P_l, defined as the ratio of emission intensities $P = (I_\mathrm{co} - I_\mathrm{cr})/(I_\mathrm{co} + I_\mathrm{cr})$ detected in co-polarized (I_co) and cross-polarized (I_cr) configurations with a circularly (σ) or linearly (π) polarized excitation laser, are direct measures of valley polarization [131–133] and valley coherence [134, 162]. Most values reported for circular and linear PL polarizations in monolayer TMDs are well below unity, and they vary significantly with material quality or the underlying substrate [131–133, 160, 161, 163–165]. A detailed understanding of the variations in P_c and P_l has been elusive to date and partly attributed to different ratios of the exciton and valley dynamics in different samples. Analogous to optical spin orientation [166], ideal initialization of the valley polarization yields in a steady-state PL measurement $P_\mathrm{c} = 1/(1 + \tau_0/\tau_\mathrm{l})$ close to unity if the exciton lifetime τ_0 is short as compared to the longitudinal valley decay time τ_l. The same argument holds for P_l as a measure of valley coherence with the transverse valley decay time τ_t. For TMD monolayers with long-lived excitons, one therefore expects a sizable reduction in the degrees of circular and linear polarizations due to exchange-mediated valley decay and dephasing [167–169] active during the exciton lifetime.

In the following we demonstrate that the notion of the degrees of circular and linear polarization as being determined simply by the exciton and valley lifetimes is of limited validity, and therefore previous quantitative conclusions drawn from this simplistic picture should be critically revised. However, the model is helpful for a qualitative interpretation of varying degrees of valley polarization and coherence across single TMD monolayers. A more quantitative analysis can be provided by taking into account the optical valley initialization processes. This insight is based

on our experiments on extended MoS_2 flakes grown by CVD and transferred onto SiO_2/Si substrates as a representative TMD material system (see Appendix A for sample details). The valley pseudospin physics in single- and poly-crystalline MoS_2 monolayers were addressed with steady-state two-dimensional circular and linear PL polarimetry.

5.2 Photoluminescence spectroscopy of extended monolayers

We begin our studies by characterizing individual MoS_2 crystals with cryogenic PL spectroscopy. The experimental setup for confocal PL spectroscopy and raster-scan imaging is shown schematically in Fig. 5.1a. The sample was cooled to 3.1 K in a closed-cycle cryostat and positioned within the confocal excitation and detection spots of a low-temperature apochromatic objective. The polarization of the excita-

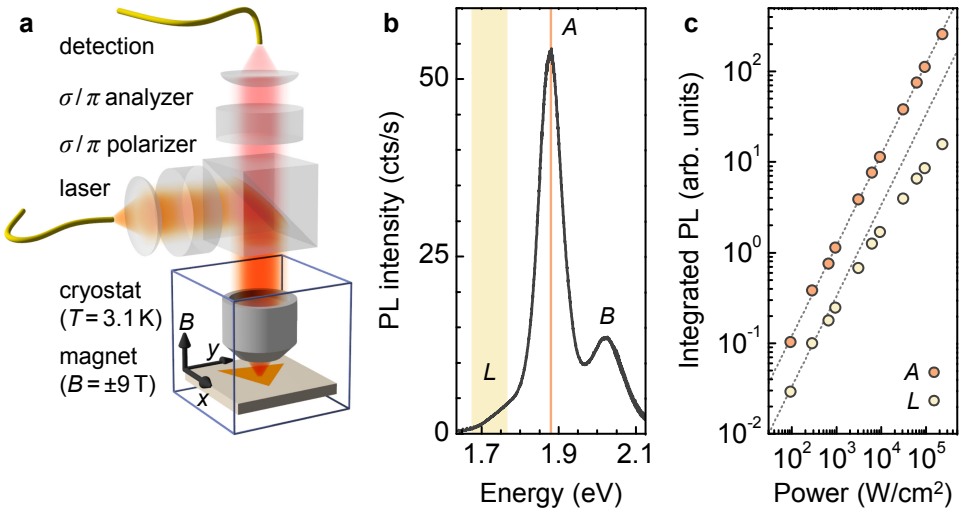

Figure 5.1: Confocal spectroscopy of extended MoS_2 monolayers. **a**, Experimental setup schematics: the sample with extended monolayer MoS_2 crystals on SiO_2 is positioned within diffraction-limited confocal laser excitation and photoluminescence detection spots (0.7 μm diameter) of a low-temperature apochromatic objective in a closed-cycle cryostat with a base temperature of 3.1 K. A solenoid allows to apply magnetic fields of up to 9 T perpendicular to the crystal plane. The excitation and detection channels feature polarizing optical components for photoluminescence polarimetry in circular (σ) and linear (π) bases. **b**, Cryogenic photoluminescence spectrum of monolayer MoS_2 with A, B, and low-energy (L) exciton features. **c**, Photoluminescence intensities of A and L excitons as a function of laser power recorded within the colored spectral bands in **b**; dashed lines indicate linear response. The data were recorded at 3.1 K with a laser at 532 nm.

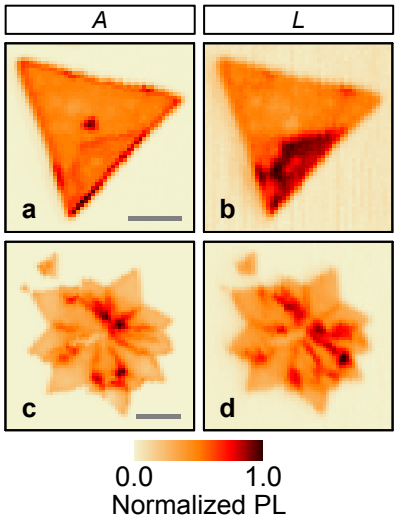

Figure 5.2: **a** and **b**, Raster-scan images of the photoluminescence intensity within the A and L exciton bands of Fig. 5.1b for a single-crystalline MoS_2 flake grown by chemical vapor deposition. **c** and **d**, Same for a poly-crystalline MoS_2 flake. The data were measured at 3.1 K with excitation at 532 nm; scale bars are 5 µm.

tion and detection pathways was set independently for circular or linear polarimetry by suitable combinations of linear polarizers, half- and quarter-waveplates. A superconducting solenoid was used to apply magnetic fields up to 9 T perpendicular to the sample.

A representative cryogenic spectrum of monolayer MoS_2 recorded with a non-resonant CW excitation laser[1] at 532 nm is shown in Fig. 5.1b. It features A and B exciton PL around 1.9 eV and 2.0 eV characteristic of monolayer MoS_2 on SiO_2 [9, 10]. Additionally, we observed a redshifted PL of localized excitons (L) which exhibit saturation as a function of the excitation laser power [170] in contrast to A excitons with linear response (Fig. 5.1c). The maps in Fig. 5.2a–d, constructed by color-coding normalized raster-scan PL within exciton-specific bands indicated in Fig. 5.1b, show the A and L exciton PL profiles for two representative MoS_2 flakes of our studies. The triangular shape (Fig. 5.2a and b) is typical for CVD-grown single-crystal flakes, while the star-shaped geometry of the poly-crystalline flake (Fig. 5.2c and d) reflects a cluster of single-crystal domains separated by grain boundaries [12, 13]. The PL intensity profiles show spatial variations across the flakes due to the presence of spatial inhomogeneities in the crystal quality. The edges and the center of the single-crystal triangle exhibit a more intense A exciton PL than the rest of the flake (Fig. 5.2a), while the L exciton emission is most intense in a 'puddle' at

[1] CNI, MLL-III-532-50-1

the right edge of the triangle (Fig. 5.2b). Based on previous studies [12, 13], Raman spectroscopy and optical inspection of other flakes on our sample, we identify the central region as a bilayer triangle formed on top of the monolayer single-crystal MoS_2. The puddle is probably a collection of point defect contaminants responsible for exciton localization [170]. The poly-crystalline star shows homogeneous domains of both A and L emission separated by lines of enhanced intensity (Fig. 5.2c and d) at the grain boundaries [12, 13] which also seem to favor exciton localization. At low excitation powers, emission hotspots of cryogenic QDs [59–62] dominate the PL intensity profiles of L excitons (see Section 5.5.1).

5.2.1 Basic spectral characteristics

Apart from the non-resonant excitation at 532 nm (2.33 eV), the PL of monolayer MoS_2 crystals on SiO_2/Si was optionally excited with a CW laser[2] at 637 nm (1.95 eV) in resonance with the blue shoulder of the A exciton. Here, the spectral features of the two excitation schemes are briefly discussed. The non-resonant PL shown in Fig. 5.3a exhibits contributions of both neutral and charged excitons, A and A^-, due to unintentional doping of MoS_2 crystals on p-doped SiO_2/Si substrates [171]. The asymmetric lineshape of the total PL (spectrum in Fig. 5.3a) can be decomposed into two Lorentzians with equal FWHM linewidths of 62 meV separated by the trion binding energy of ~ 30 meV [172]. The near-resonant spectrum[3] recorded with a long-pass filter at 652 nm (1.90 eV) in Fig. 5.3b (gray and blue traces show for the same flake position non-resonant and near-resonant spectra, respectively) exhibited additional sharp features identified as Raman scattered photons by the substrate (Si) and the MoS_2 monolayer, with assignments given in Fig. 5.4a adopted from Ref. 173. The Raman spectra were useful to identify bilayer regions (as in the center of the single-crystal triangle) where they exhibited a characteristic splitting of the $A_{1g}(\Gamma)$ mode shown in Fig. 5.4b under resonant excitation with the fundamental exciton [174].

To avoid contamination of the opto-valleytronic properties of A excitons by Raman photons, we selected a spectral band of 3 meV width centered at 1.879 eV near the PL maximum of the A exciton emission and away from Raman resonances (the red spectral interval in Figs. 5.1b, 5.3, and 5.4a is the same). Moreover, for the quantitative analysis of the degree of circular polarization of A excitons, the contribution of A^- was removed by fitting the total PL with two Lorentzians and subtracting the contribution of the trion PL from the spectral band chosen for the opto-valleytronic analysis as described above.

[2] New Focus, Velocity TLB-6704
[3] The spectral resolution for confocal PL measurements was ~ 0.35 meV.

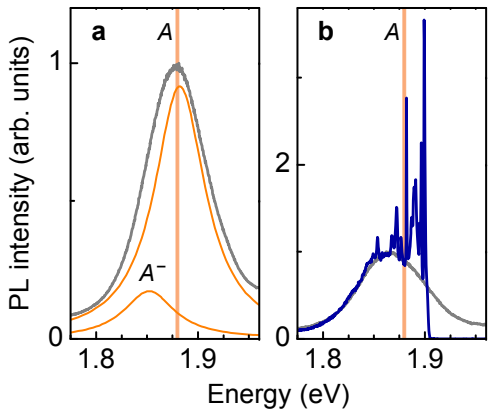

Figure 5.3: **a**, Photoluminescence spectrum reproduced from Fig. 5.1b (gray) with Lorentzian fits (orange) to the contributions of the neutral and charged excitons, A and A^-, centered around 1.882 eV and 1.852 eV, respectively, with full-width at half-maximum linewidths of 62 meV. **b**, Comparison of the photoluminescence spectra for non-resonant excitation at 532 nm (2.33 eV) and excitation at 637 nm (1.95 eV) in resonance with the blue shoulder of the A exciton (gray and blue traces, respectively); the near-resonant spectrum was recorded with a long-pass filter at 652 nm (1.90 eV). The A exciton band is indicated in red for all spectra. Sharp spectral features on the photoluminescence peak in **b** are Raman modes as described in Fig. 5.4. The data were recorded at 3.1 K.

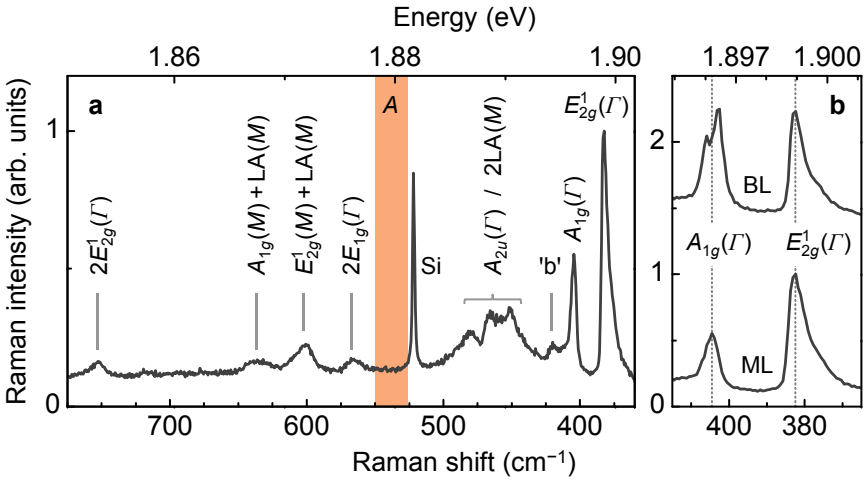

Figure 5.4: **a**, Monolayer MoS_2 Raman spectrum for the near-resonant excitation at 637 nm; the Raman modes were assigned according to the bulk notation of Ref. 173. The spectrum was measured with a resolution of ~ 0.6 cm^{-1} on the same flake and regular position as in Fig. 5.3b; note that the A exciton band of 3 meV width (shown in red) is away from Raman features. **b**, Vertically offset Raman spectra of the $E^1_{2g}(\Gamma)$ and $A_{1g}(\Gamma)$ modes for the near-resonant excitation at 637 nm on representative monolayer (ML) and bilayer (BL) positions of the triangular flake in Fig. 5.2 (the dashed lines are guides to the eye). The splitting of the $A_{1g}(\Gamma)$ mode is characteristic of bilayer transition metal dichalcogenides under resonant excitation [174]. All measurements were obtained at 3.1 K.

5.2.2 Polarization-resolved photoluminescence

Co-polarized (I_{co}) and cross-polarized (I_{cr}) PL spectra recorded with an excitation laser at 637 nm are shown in Fig. 5.5a and c for circular and linear bases, respectively. The spectral characteristics of P_c and P_l, presented in Fig. 5.5b and d, were calculated as the normalized differences between co- and cross-polarized PL intensities according to $P = (I_{co} - I_{cr})/(I_{co} + I_{cr})$. Data in Fig. 5.5e and f confirm that the degree of linear polarization is independent of the choice of the linear basis (the linear PL polarization is parallel to the axis of the excitation laser set along π^H and π^D in Fig. 5.5e and f, respectively). The red bar in Fig. 5.5a–d is the earlier assigned band used for confocal opto-valleytronic imaging of A excitons.

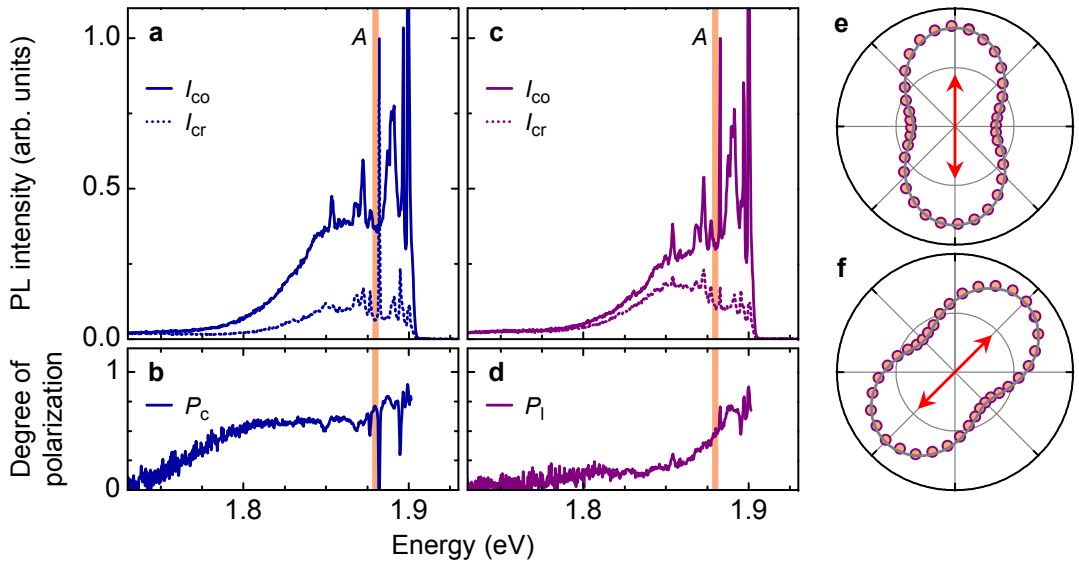

Figure 5.5: **a**, Photoluminescence spectra recorded in co-polarized (solid trace, I_{co}) and cross-polarized (dashed trace, I_{cr}) configurations with σ^+ excitation. **b**, Corresponding degree of circular polarization P_c. **c**, Co- and cross-polarized photoluminescence spectra under linear (π^H) excitation and **d**, degree of linear polarization P_l. The A exciton band indicated in red was used for confocal opto-valleytronic imaging. **e**, **f**, Polar plots of the normalized photoluminescence intensity within the spectral band as a function of the rotation angle θ of the linear analyzer for π^H, π^D orientations of the linear polarizer (indicated by red arrows), respectively. The gray solid lines are fits to the data with a $[1+P_l\cos(2\theta-2\phi)]$ functional dependence, where ϕ is the polarizer angle. All measurements were recorded on the monolayer triangle away from defects with an excitation laser at 637 nm (1.95 eV) and a long-pass filter at 652 nm (1.90 eV); the temperature was 3.1 K.

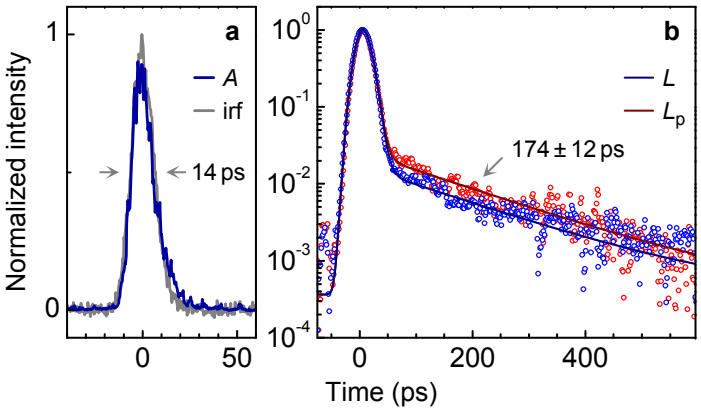

Figure 5.6: **a**, **b**, Time-resolved photoluminescence of A excitons (blue trace) and localized excitons in and away from the puddle, L_p and L (red and blue circles). Band-pass filters with widths of 35 meV (50 meV) were used for spectral selection of A (L and L_p) excitons. The decay dynamics in **a** were limited by the instrument response function (irf) with a measured full-width at half-maximum of ~ 14 ps (gray trace). The solid lines in **b** are fits to the data: the fast decay components of the localized excitons were dispersion broadened, the slow components exhibited monoexponential decays with decay constants of 174 ± 12 ps and contributions relative to the total signal of 12% (L_p, dark red trace) and 8% (L, dark blue trace). All data were measured on the triangular MoS_2 flake with laser excitation at 637 nm in **a** and 630 nm in **b**; the temperature was 3.1 K.

5.2.3 Time-resolved photoluminescence

In the following we address the PL decay dynamics of A and localized excitons on a regular position and in the puddle for the MoS_2 triangle of Fig. 5.2. The time-resolved studies presented in Fig. 5.6 were performed using a streak camera for detection and a femtosecond optical parametric oscillator[4] (OPO) for excitation. The fiber-coupled system exhibited dispersion-limited temporal resolution down to ~ 10 ps depending on the spectral bandwidth and the length of the single-mode fiber. The A exciton PL dynamics, measured in a spectral band of 35 meV, showed radiative decay with a time constant below the resolution limit of ~ 14 ps given by the dispersion-limited instrument response function (Fig. 5.6a). Localized excitons, selected by a band-pass filter of 50 meV width, exhibited two decay timescales (Fig. 5.6b): the dominant fast component was resolution-limited (with partial contribution from A excitons), and the slow component exhibited monoexponential decay with a lifetime of 174 ± 12 ps in agreement with previous results [161]. The slow decay channel accounted for 8% of the total PL intensity on a regular position (L) and for 12% in the puddle (L_p) of the triangular crystal.

[4]Coherent, Mira-OPO

5.3 Raster-scan opto-valleytronic imaging

The polarization-resolving feature of our setup allows us to identify characteristic signatures of crystal defects with circular and linear polarimetry. To construct polarimetric maps we raster-scanned the sample with respect to fixed confocal excitation and detection spots, and performed spectral acquisition of co- and cross-polarized PL at each raster pixel with an excitation power density of $\sim$ 25 kW/cm^2. An averaged background spectrum was subtracted from all image pixels, and co- and cross-polarized PL intensities of A and L excitons were integrated within the spectral bands shown in Fig. 5.1b. Pixels with a standard deviation of P above 0.05, stemming from vanishingly small PL intensities away from the flake, were set to zero.

The two-dimensional maps of the degrees of circular and linear PL polarizations in Fig. 5.7a–d were recorded for the flakes of Fig. 5.2 with a laser at 637 nm in resonance with the blue shoulder of the A exciton PL which typically results in high near-resonant polarization values [19, 132, 134, 161]. In the absence of an external magnetic field, time-reversal symmetry implies identical degrees of K and K' valley polarization and thus equal P_c recorded with σ^+ and σ^- polarimetry [109]. Equivalently, the valley coherence is independent of the choice of the linear basis [134].

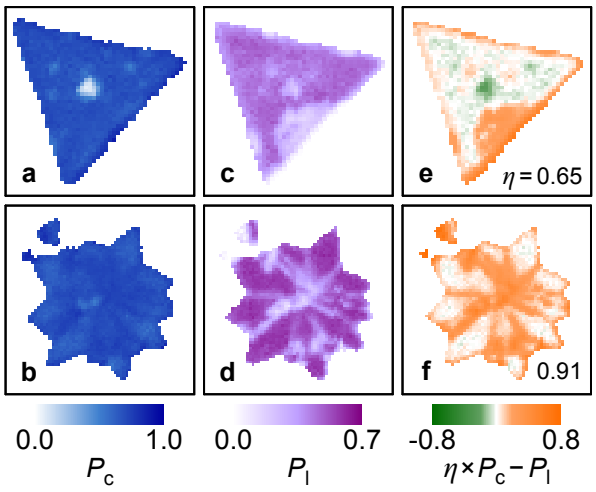

Figure 5.7: Raster-scan polarimetry of single- and poly-crystalline MoS_2. **a**, **b**, Circular and **c**, **d**, linear polarimetric profiles of the photoluminescence within the A exciton band for single- and poly-crystalline MoS_2 of Fig. 5.2, respectively. The false-color maps in **e** and **f** were computed as scaled differences of P_c and P_l (with different scaling factors η as given in **e** and **f**) to highlight the regions of bilayer formation (green) and valley decoherence at crystal defects (orange). All data were recorded with an excitation laser at 637 nm; the temperature was 3.1 K.

First, we focus our analysis on the fundamental A exciton to discuss the polarization in the K valley, and the valley coherence in terms of K-K' superpositions.

The feature of highest contrast in the P_c maps of the single- and poly-crystalline flakes is located at the triangle center (Fig. 5.7a) and coincides with the bilayer region discussed earlier. Optical selection rules are different for TMD bilayers [175] and provide direct means to single out bilayer regions in polarimetric imaging. Away from bilayer regions and edges, the degree of P_c in Fig. 5.7a and b is remarkably high and homogeneous. Most surprisingly, the grain boundaries of the poly-crystalline star are almost invisible in the map of Fig. 5.7b. This observation of homogeneous valley polarization is in stark contrast to the sizable variations in the PL intensity profiles (Fig. 5.2a and c). It is also strongly contrasted by the pronounced inhomogeneities of the respective P_l profiles in Fig. 5.7c and d, where both the puddle and the grain boundaries appear most prominently as sites of low valley coherence. To discuss these differences qualitatively, we recall the simple model where valley depolarization and dephasing are responsible for the reduction of P_c and P_l during the exciton lifetime. High P_c values in the maps of Fig. 5.7a and b imply that the degree of optical valley pseudospin initialization is high in our experiments — a necessary condition for the optical generation of valley coherence. With the exception of the bilayer region, the homogenous P_c profiles also suggest that the longitudinal valley relaxation is slow on the timescale of the exciton lifetime even in the presence of disorder. On the same timescale, however, rapid transverse valley relaxation results in locally reduced P_l values as in the defective regions of the flakes in Fig. 5.7c and d.

In order to visualize the regions of rapid valley dephasing signified by large differences in P_c and P_l, we present differential polarization profiles for both representative flakes. Fig. 5.7e and f were computed with a scaling factor η of 0.65 and 0.91, respectively, to enhance the map contrast and thus the visibility of monolayer defects by highlighting sites of valley decoherence (crystal edges, grain boundaries, and the puddle of surface contaminants) in orange and bilayers in green. Orange regions of disorder are characterized by rapid dephasing of optically generated quantum coherent superpositions of K and K' excitons without signatures of low valley polarization. The white areas of the differential profiles in Fig. 5.7e and f identify the least defective monolayer crystals most favorable for opto-valleytronic applications.

These qualitative observations are furthermore documented in Fig. 5.8, where we reproduce the maps of Fig. 5.7a–d to indicate specific positions (numbered from 1 to 6) for a quantitative comparison of site-to-site variations of P_c (blue bars) and P_l (purple bars) summarized in Fig. 5.8e for the of A exciton band. Similar polarimetric measurements were performed on other MoS_2 flakes. Fig. 5.9a, c and Fig. 5.9b, d show profiles of P_c and P_l for a poly-crystalline and a single-crystalline

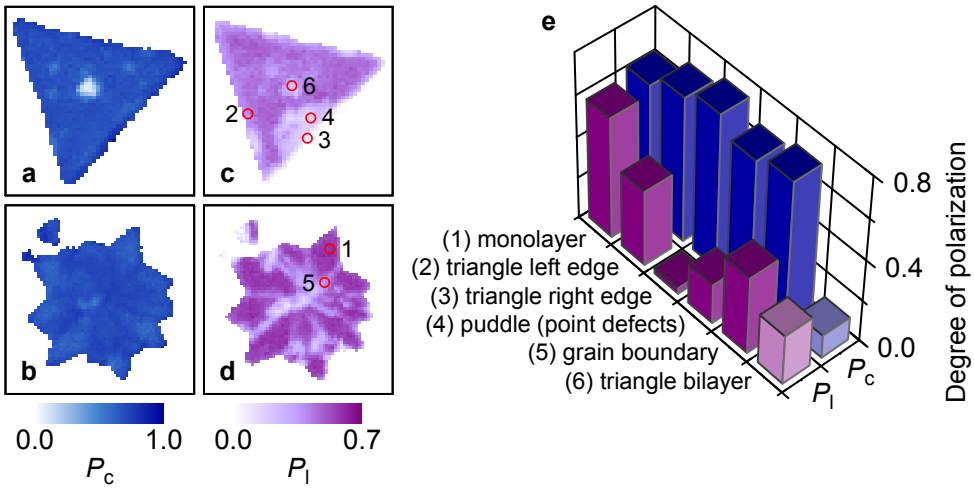

Figure 5.8: **a**, **b**, Circular and **c**, **d**, linear polarimetric profiles for A exciton bands of single- and poly-crystalline MoS_2, respectively. The data are reproduced from Fig. 5.7a–d with specific positions 1–6 added for a quantitative comparison. **e**, P_c (blue bars) and P_l (purple bars) for A excitons at characteristic positions of the flakes marked with red circles in **c** and **d**. All data were measured at 3.1 K with laser excitation at 637 nm.

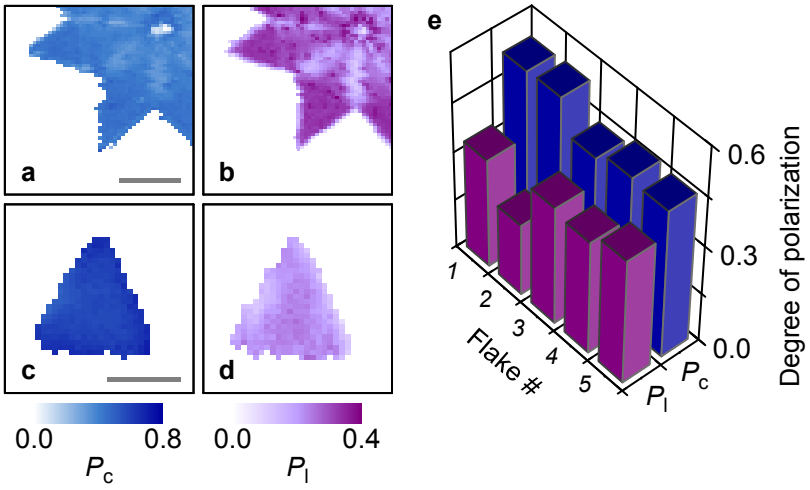

Figure 5.9: **a**, **b**, Maps of P_c and P_l for a segment of a poly-crystalline MoS_2 flake (scale bar is 10 μm). **c**, **d**, Maps of P_c and P_l for a single-crystal monolayer triangle (scale bar is 3 μm). The bar chart in **e** summarizes variations in P_c and P_l (blue and purple bars, respectively) for five different MoS_2 monolayers at 3.1 K and 637 nm excitation.

MoS_2 monolayer, respectively. The bar chart in Fig. 5.9e summarizes the statistics of P_c and P_l acquired on five different monolayer flakes.

5.3.1 Equivalence of polarization bases at zero magnetic field

In the absence of an external magnetic field, time-reversal symmetry implies the equivalence of the degrees of circular polarization measured in σ^+ and σ^- configurations. The set of data in Fig. 5.10a–c demonstrates that the degree of the circular polarization is independent of the choice of the circular basis: P_c is identical (within the precision of our measurement) for σ^+ and σ^- polarization bases (compare Fig. 5.10a and b, respectively). This fact is also reflected by the vanishing difference profile $\Delta P_c = P_c(\sigma^+) - P_c(\sigma^-)$ shown in Fig. 5.10c. The analogous set of data is respectively shown for the degrees of linear polarization recorded under horizontal (π^H) and diagonal (π^D) linearly polarized excitations in Fig. 5.10d and e; their vanishing difference $\Delta P_l = P_l(\pi^H) - P_l(\pi^D)$ is plotted in Fig. 5.10f. The data demonstrate the independence of P_l of the choice of the linear basis.

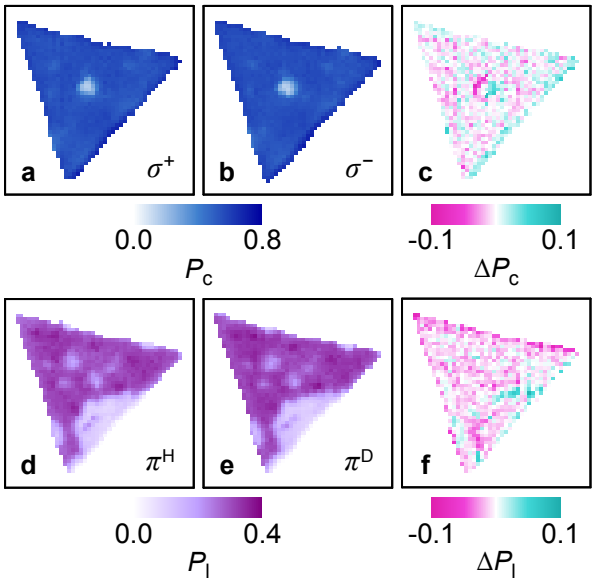

Figure 5.10: **a**, **b**, P_c and **d**, **e**, P_l for circularly polarized σ^+, σ^- (right- and left-handed) and linearly polarized π^H, π^D (horizontal and diagonal) laser excitation. **c**, Equivalence of the circular polarization bases, where changes to P_c are prohibited by time-reversal symmetry, computed as $\Delta P_c = P_c(\sigma^+) - P_c(\sigma^-) \simeq 0$. **f**, Same for different linear polarization bases: $\Delta P_l = P_l(\pi^H) - P_l(\pi^D) \simeq 0$. Note the changed scale in **c** and **f**. All measurements were spectrally integrated and recorded at zero magnetic field with laser excitation at 637 nm. The temperature was 3.1 K.

5.4 Opto-valleytronic imaging in magnetic field

Our analysis is complemented by circular polarimetric profiling in non-zero magnetic fields. A positive magnetic field oriented orthogonal to the TMD monolayer plane breaks the time-reversal symmetry and lifts the valley degeneracy by decreasing (increasing) the exciton energy in the K (K') valley [142–146, 148]. Moreover, it changes the degree of circular polarization [142–145, 148], which we monitored for our flakes with magneto-optical polarimetry. The polarimetric maps recorded in a magnetic field of +9 T within the A and L exciton bands are shown in Fig. 5.11a–d for the representative single-crystal triangle. The main signature of the valley Zeeman effect in opto-valleytronic imaging is the field-induced difference in P_c measured with σ^+ and σ^- excitations (compare Fig. 5.11a and c with b and d). In a positive field of 9 T the P_c within both A and L spectral bands exhibits a decrease (increase) under σ^+ (σ^-) excitation in regular regions of the triangular flake.

To analyze the field-induced changes in the valley polarization of A excitons we removed the contribution of the trion PL from the A exciton band by spectral deconvolution (see Section 5.2.1). The resulting evolution of P_c with magnetic field on a regular site of the single-crystal triangle is presented in the upper and central

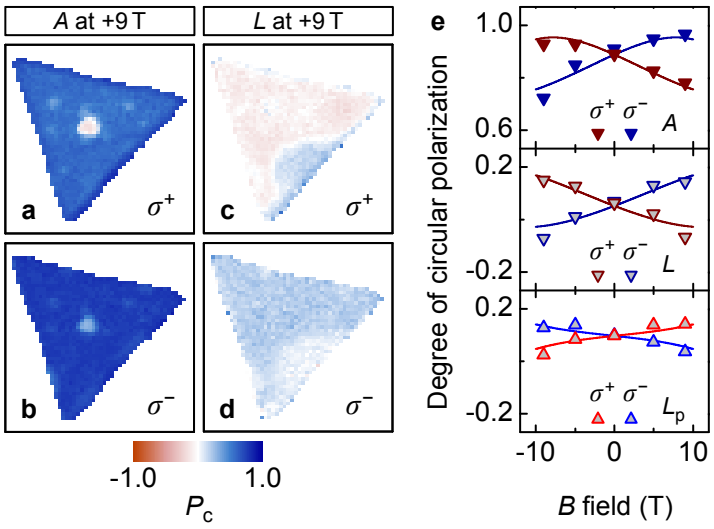

Figure 5.11: The valley Zeeman effect in polarimetric imaging. **a**, **b**, and **c**, **d**, Circular polarimetric profiles within the A and L exciton bands under σ^+ and σ^- excitations in a magnetic field of +9 T. Note the negative P_c of bilayer and L excitons away from the puddle (red-colored regions). **e**, Evolutions of A and L exciton P_c with magnetic field. Upper and central panels: A and L excitons in a monolayer region away from the puddle; lower panel: L_p excitons in the puddle (the contribution of trions was removed from the P_c of A). The solid lines are results of the model as described in the text. All data were recorded at 3.1 K with excitation at 637 nm.

panels of Fig. 5.11e for the deconvolved A exciton and for the L exciton band, respectively. The data in the upper panel of Fig. 5.11e exhibit an evolution similar to A excitons in WSe_2 monolayer [144] with an X-shaped pattern that can be much less pronounced on different samples and under less resonant excitation [148]. This X-shape is not a generic feature of TMD magnetoluminescence as it is distinct from the P_c evolutions of $MoSe_2$ neutral excitons in magnetic field [143, 148]. It rather reflects a counter-intuitive steady-state distribution of excitons among the two Zeeman-split K and K' valleys [144]: at positive magnetic fields the population in the energetically higher valley Zeeman branch K' becomes progressively protected from the relaxation into the lower branch K with increasing magnetic field. This 'hot' valley exciton population on a regular position is contrasted by the 'thermal' distribution of localized excitons in the puddle, L_p, with a sign reversal of the X-pattern (Fig. 5.11e, lower panel) as one would expect for a population redistribution that favors the exciton state of lowest energy. The fits to the data (solid lines in Fig. 5.11e) are based on the rate equation model discussed in Section 5.4.1.

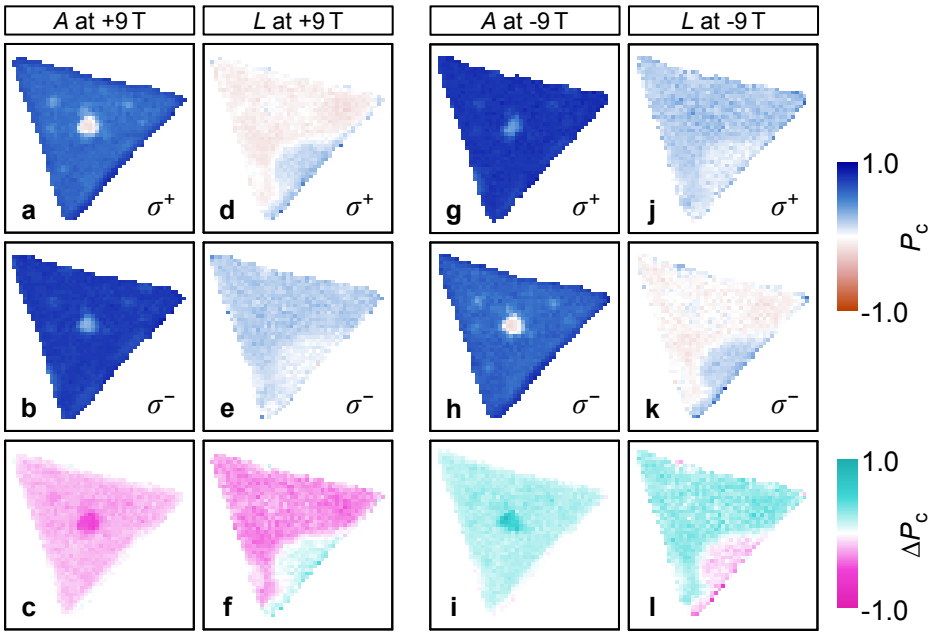

Figure 5.12: Left panel: **a**, **b**, and **d**, **e**, Circular polarimetric profiles within the A and L exciton bands under σ^+ and σ^- excitations in a magnetic field of $B = +9$ T reproduced from Fig. 5.11. **c**, **f**, Corresponding changes in the degrees of circular polarization of the photoluminescence within the A and L exciton bands, respectively, computed as $\Delta P_c = P_c(\sigma^+) - P_c(\sigma^-)$. Right panel: **g**–**l**, Same as the left panel **a**–**f**, but for $B = -9$ T. Sign reversal of magnetic field interchanges the roles of the Zeeman branches associated with σ^+ and σ^- excitations, which results in a sign reversal of ΔP_c as compared to the left panel. All data were recorded at 3.1 K and with a 637 nm laser.

The changes of the degree of circular polarization, quantified as $\Delta P_c = P_c(\sigma^+) - P_c(\sigma^-)$, are visualized in Fig. 5.12 for opto-valleytronic imaging in positive as well as negative fields. For A excitons at $B = +9$ T, ΔP_c is negative (magenta-colored) throughout the MoS_2 flake (Fig. 5.12c). This corresponds to a decrease (increase) of the σ^+ (σ^-) degree of circular polarization for the lower (upper) K (K') Zeeman branch of A excitons as reproduced in Fig. 5.12a (Fig. 5.12b). The L excitons (with corresponding opto-valleytronic maps reproduced in Fig. 5.12d and e) show the same trend away from the puddle and reversed features in the puddle (cyan-colored region in Fig. 5.12f) in accord with thermal population distribution. The right panel of Fig. 5.12 shows the same set of data but for $B = -9$ T. The sign reversal of the magnetic field results in interchanged roles of σ^+ and σ^- polarizations (Fig. 5.12g, h, j, and k) and thus in a sign reversal of ΔP_c (Fig. 5.12i and l).

5.4.1 Theoretical modeling of the valley polarization

In the following we model the degree of circular polarization of excitons in monolayer MoS_2 in the presence of an external magnetic field oriented perpendicular to the crystal surface. To this end we consider a four level system with the crystal ground state $|0\rangle$, the K exciton state $|1\rangle$, the K' exciton state $|2\rangle$, and an excited state $|3\rangle$ in one of the two valleys. All levels are denoted in Fig. 5.13, where without loss of generality the excited state $|3\rangle$ is in the K valley. In the following, exciton states in K (K') that couple to σ^+ (σ^-) polarized optical transitions are tagged with the valley index $\kappa = +1$ ($\kappa = -1$).

For a σ^+ (σ^-) polarized optical transition that is assumed to create population exclusively in the excited K (K') state, the temporal evolution of the populations in each state is given by the following set of rate equations:

$$\text{ground state} \quad |0\rangle: \quad \dot{\rho}_0 = \rho_1\gamma_0 + \rho_2\gamma_0 - \rho_0\gamma_{03}, \tag{5.1a}$$

$$K \text{ state} \quad |1\rangle: \quad \dot{\rho}_1 = \rho_3\gamma_{31} + \rho_2\gamma_{21} - \rho_1\gamma_{12} - \rho_1\gamma_0, \tag{5.1b}$$

$$K' \text{ state} \quad |2\rangle: \quad \dot{\rho}_2 = \rho_3\gamma_{32} - \rho_2\gamma_{21} + \rho_1\gamma_{12} - \rho_2\gamma_0, \tag{5.1c}$$

$$\text{excited state} \quad |3\rangle: \quad \dot{\rho}_3 = \rho_0\gamma_{03} - \rho_3\gamma_{31} - \rho_3\gamma_{32}, \tag{5.1d}$$

where ρ_i is the population of the ith state, $\dot{\rho}_i$ is the temporal derivative of ρ_i, and γ_{ij} is the transition rate from state i to j. The population dynamics are governed by the following rates: γ_{03} denotes the absorption rate from the crystal ground state into an excited state in one of the two valleys, γ_{31} and γ_{32} are the valley conserving and valley flipping relaxation rates (or vice versa), γ_{12} and γ_{21} are the valley flipping rates among the K and K' states, and γ_0 is the K and K' exciton decay rate (including both radiative and non-radiative channels). The total population of the system is

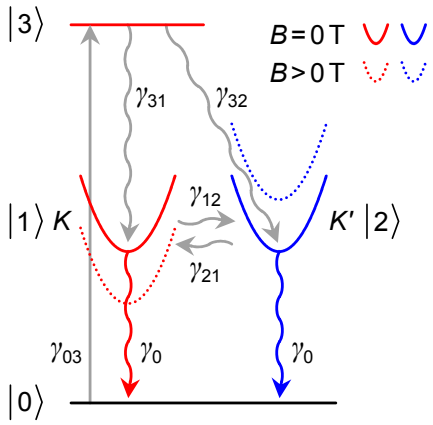

Figure 5.13: Schematics of the model system: energy levels and transition rates of a four level system with the crystal ground state $|0\rangle$, the K exciton state $|1\rangle$, the K' exciton state $|2\rangle$, and the excited K exciton state $|3\rangle$. The solid (dotted) red and blue dispersions represent K and K' excitons without (with) an external magnetic field. γ_{03} denotes the absorption rate from the crystal ground state into the excited state of the K valley exciton, γ_{31} and γ_{32} are the valley conserving and valley flipping relaxation rates, γ_{12} and γ_{21} are the valley flipping rates among the K and K' states, and γ_0 is the K and K' exciton decay rate (including both radiative and non-radiative channels).

normalized to $\rho_0 + \rho_1 + \rho_2 + \rho_3 = 1$, and steady-state solutions are obtained for $\dot{\rho}_i = 0$. The degree of circular polarization $P_c = (I_{co} - I_{cr})/(I_{co} + I_{cr})$ is obtained from steady-state populations ρ_1 and ρ_2 of the K and K' valleys:

$$P_c = \kappa \frac{\rho_1 - \rho_2}{\rho_1 + \rho_2}, \tag{5.2}$$

with the explicit expression equivalent to the one derived in the Supplementary Information of Ref. 144:

$$P_c = \kappa \left(\frac{\gamma_0}{\gamma_0 + \gamma_{12} + \gamma_{21}} \frac{\gamma_{31} - \gamma_{32}}{\gamma_{31} + \gamma_{32}} + \frac{\gamma_{21} - \gamma_{12}}{\gamma_0 + \gamma_{12} + \gamma_{21}} \right). \tag{5.3}$$

We rewrite this expression as

$$P_c = \kappa \left(\frac{\gamma_0}{\gamma_0 + \gamma_{12} + \gamma_{21}} \frac{1 - b_\kappa}{1 + b_\kappa} + \frac{\gamma_{21} - \gamma_{12}}{\gamma_0 + \gamma_{12} + \gamma_{21}} \right), \tag{5.4}$$

with a branching parameter b_κ given by the ratio of the valley flipping to the valley conserving relaxation rates:

$$b_\kappa = \left(\frac{\gamma_{32}}{\gamma_{31}} \right)^\kappa. \tag{5.5}$$

The definition of the branching parameter implies $b_\kappa = \gamma_{32}/\gamma_{31}$ ($b_\kappa = \gamma_{31}/\gamma_{32}$) for $\kappa = +1$ ($\kappa = -1$).

First, we examine the the degree of circular polarization given by Eqs. 5.3 and 5.4 at zero magnetic field. In the presence of time-reversal symmetry, the valley flipping processes are symmetric and thus $\gamma_{12} = \gamma_{21}$. Moreover, in the limit of ideal initial polarization, i. e. for $b_\kappa = 0$, Eqs. 5.3 and 5.4 simplify to

$$P_\mathrm{c}^0 = \frac{1}{1 + 2\gamma_\mathrm{l}/\gamma_0} = \frac{1}{1 + 2r_0}, \tag{5.6}$$

where $r_0 = \gamma_{12}/\gamma_0 = \gamma_{21}/\gamma_0$ is the ratio of the zero-field longitudinal valley depolarization rate $\gamma_{12} = \gamma_{21} = \gamma_\mathrm{l}$ to the exciton decay rate γ_0. This expression is equivalent to the one derived in Ref. 132, and it corresponds to the steady-state degree of circular polarization in optical spin orientation with ideal initial polarization [166]:

$$P_\mathrm{c}^0 = \frac{1}{1 + \tau_0/\tau_\mathrm{l}}, \tag{5.7}$$

if we identify $\tau_0 = 1/\gamma_0$ as the exciton lifetime and $\tau_\mathrm{l} = 1/(2\gamma_\mathrm{l})$ as the valley depolarization time.

In case the initial polarization of the fundamental exciton populations in K and K' valleys is non-ideal because of valley flipping events upon relaxation from the optically excited state, we have analogous to imperfect spin orientation [166]:

$$P_\mathrm{c}^0 = P_\mathrm{i}^0 \frac{1}{1 + 2r_0} = \frac{1 - b_\kappa}{1 + b_\kappa} \frac{1}{1 + 2r_0}, \tag{5.8}$$

with the initial polarization $P_\mathrm{i}^0 = (1 - b_\kappa)/(1 + b_\kappa)$ given by the yield of optical valley polarization of K and K' populations at zero magnetic field in the presence of finite branching $b_\kappa > 0$.

In a finite magnetic field B applied perpendicular to the sample, the valley Zeeman splitting Δ_VZ [142–146, 148] introduces an imbalance between γ_{12} and γ_{21}. In the presence of non-zero branching, we return to Eqs. 5.3 and 5.4 to recapitulate the findings of Ref. 144 with respect to the magnetic field evolution of P_c. First we note qualitatively that due to the valley Zeeman splitting, the imbalance of γ_{12} and γ_{21} increases (decreases) the population transfer rate from the upper (lower) to the lower (upper) Zeeman branch. Thus, provided sufficiently rapid valley depolarization on the timescale of the exciton lifetime, we expect the population to relax into the energetically lower valley. Consequently, the P_c of the upper (lower) Zeeman valley should decrease (increase) with magnetic field. The opposite trend is observed in our study of A and L excitons in monolayer MoS_2 away from defects in agreement with the A exciton response in monolayer WSe_2 reported in Ref. 144. This counter-

intuitive population distribution was attributed to (i) slow intervalley scattering and (ii) polarization protecting branching ratio b_κ that decreases (increases) for the upper (lower) valley with magnetic field [144]. Since no explicit expression for the functional form of the evolution of b_κ with magnetic field was given in Ref. 144, and to account for different materials and experimental conditions, we approximate b_κ with a linear function in B:

$$b_\kappa(B) = b_0 + \kappa\delta B, \tag{5.9}$$

where b_0 is the zero-field branching ratio and δ is a proportionality factor. It is worth noting that Eq. 5.9 should be interpreted as a low-field approximation since it would yield unphysical negative values for $b_\kappa(B)$ in the limit of sufficiently high fields. Moreover, a difference in δ for the K and K' valleys could account for broken time-reversal symmetry in absence of a magnetic field as pointed out in Ref. 144.

To proceed with the analysis of our data using the model of Ref. 144 where $\gamma_1 \ll \gamma_0$ (or correspondingly $r_0 \simeq 0$) was assumed, we fit the P_c evolutions of the A and L excitons on a regular position of the triangular flake with r_0, b_0, and δ as fitting parameters. The results of best fits to the data, obtained from least χ^2_{red} deviation (defined by the unweighted sum of squared deviations between fits and data and divided by the number of degrees of freedom), are presented in Fig. 5.14.

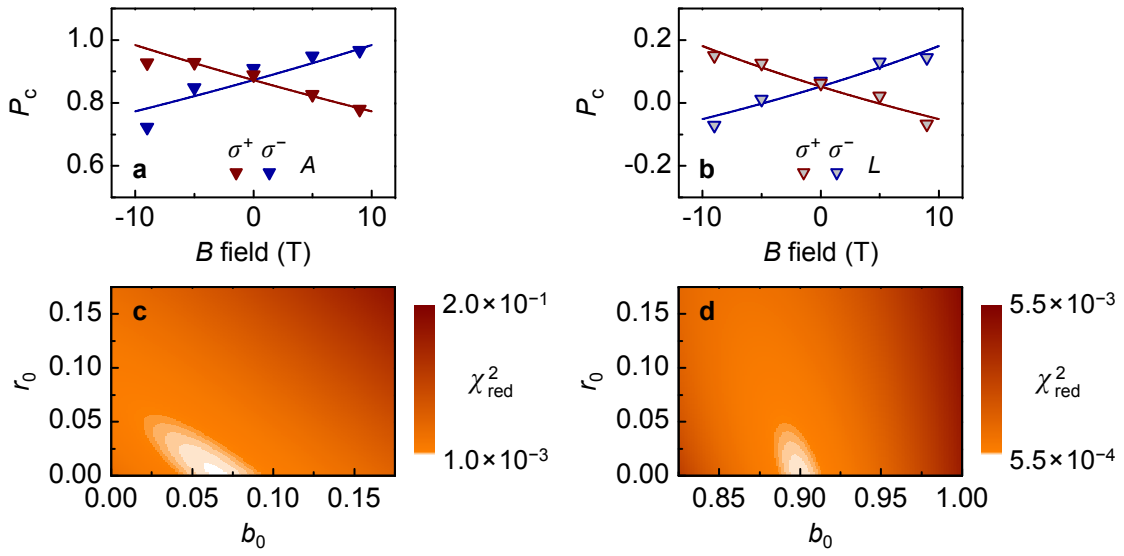

Figure 5.14: **a**, **b**, P_c as a function of magnetic field for A and L excitons; the data are reproduced from Fig. 5.11e. Solid lines are least χ^2_{red} fits according to Eqs. 5.4 and 5.9. Best fits were obtained with $b_0 = 0.07$ and 0.90, $\delta = 0.006$ T^{-1} and 0.018 T^{-1} for A and L excitons, respectively, and $r_0 = 0$ for both A and L. **c**, **d**, Associated χ^2_{red} as a function of r_0 and b_0 for A and L, and δ values given above.

The non-thermal population distribution of both A and L excitons is reflected by the counter-intuitive X-pattern of higher P_c values for the Zeeman branches with higher energy. It is consistent with slow longitudinal valley depolarization on the timescale of the exciton lifetime, and best fits actually yield $r_0 = 0$ for both A and L excitons. The zero-field branching ratio for the selectively initialized population is small for A excitons ($b_0 = 0.07$) and large for L excitons ($b_0 = 0.90$) as expected from the less resonant excitation of the latter. In this framework, the evolution of the branching ratio with magnetic field critically determines the respective P_c pattern: both A and L excitons exhibit an increasing protection of the optical valley polarization in the upper Zeeman valley as the branching ratio between the valley flipping and conserving relaxation rates decreases ($\delta > 0$ for both A and L) due to exchange-modified exciton dispersions [144].

The model of Ref. 144 within the framework of Eqs. 5.4 and 5.9 requires vanishingly small values of r_0 without quantifying its smallness. To obtain an estimate for the ratio of the longitudinal valley depolarization time to the exciton lifetime, we extend the model of Ref. 144 by assigning thermal imbalances to the longitudinal intervalley flipping rates γ_{12} and γ_{21} explicitly using the Boltzmann factor $\exp(\beta)$:

$$\gamma_{12} = r_0\gamma_0 \exp(-\beta), \tag{5.10a}$$

$$\gamma_{21} = r_0\gamma_0 \exp(+\beta), \tag{5.10b}$$

where, at a temperature T, the exponent $\beta = \Delta_{VZ}/(2k_BT)$ is determined by the Boltzmann constant k_B and the valley Zeeman splitting[5] $\Delta_{VZ} = g_{VZ}\mu_B B$ linear in the magnetic field B (with g_{VZ} being the effective exciton g-factor and μ_B the Bohr magneton) [142–146, 148]. The zero-field ratio r_0 defined by Eq. 5.6 is likely to exhibit a magnetic field dependence but short of knowledge of its functional form is assumed here as constant. The exponential imbalance of γ_{12} and γ_{21} is responsible for an effective unidirectional thermalization of population from the upper to the lower Zeeman branch during the exciton lifetime, and modifies Eq. 5.4 to

$$P_c = \frac{1}{1 + 2r_0 \cosh\beta} \frac{1 - b_\kappa}{1 + b_\kappa} + \kappa \frac{2r_0 \sinh\beta}{1 + 2r_0 \cosh\beta}. \tag{5.11}$$

The degree of circular polarization is now sensitive to the thermal imbalance of the intervalley scattering rates through the Boltzmann factor, and it accounts for the non-zero branching in the polarization initialization with its characteristic magnetic field dependence via $b_\kappa(B)$ given by Eq. 5.9. The second term drives the thermal population distribution among the K and K' valleys, while the first term counteracts

[5] Expressed as the difference between K' and K exciton energies.

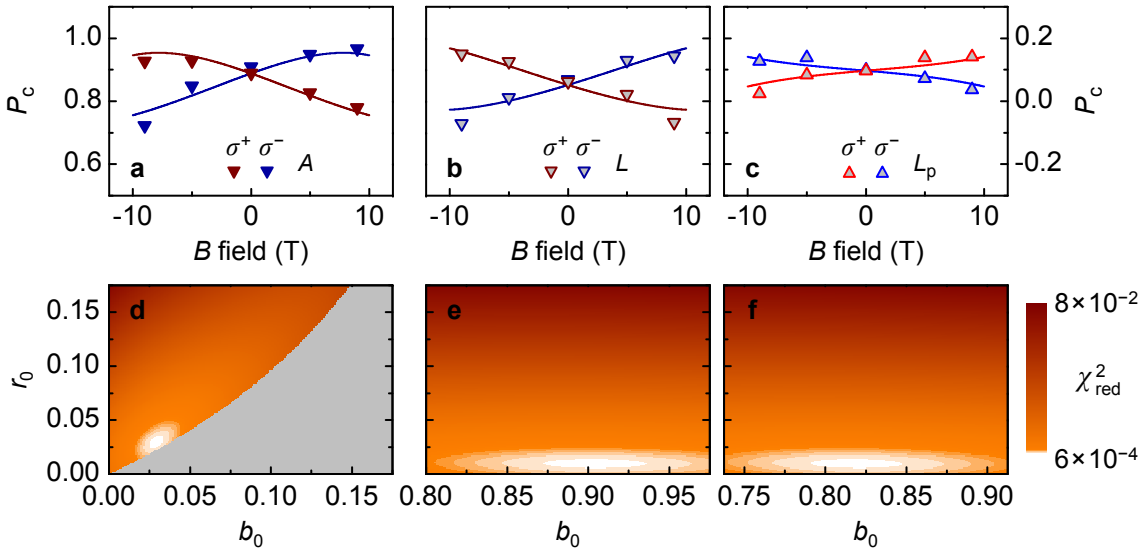

Figure 5.15: a–c, Evolution of A, L, and L_p exciton P_c with magnetic field (the data is reproduced from Fig. 5.11e). Solid lines are a least χ^2_{red} simultaneous fit to the data according to the model given by Eqs. 5.9 and 5.11. To reduce the number of free fitting parameters, the g-factor of the A excitons was fixed to $g_{VZ} = 4.0$, and a global temperature T was assumed. Moreover, $\delta = 0$ was used for L_p, and g and r_0 were set equal for L and L_p. Best fit was obtained for the following values of the remaining free fitting parameters: $b_0 = 0.03$, 0.90, and 0.82 for A, L, and L_p; $r_0 = 0.03$ for A and 0.01 for L and L_p; $\delta = 0.012$ T^{-1} for A and 0.027 T^{-1} for L; $g_{VZ} = 4.4$ for L and L_p; $T = 9$ K. **d–f**, Corresponding χ^2_{red} values as a function of r_0 and b_0 for A, L, and L_p with other parameters as given above. The gray region in **d** with unphysical values of $|P_c| > 1$ was not evaluated.

this thermalization via the functional dependence of the branching ratio b_κ on the magnetic field in favor of a 'hot' population distribution.

With this expression for the field-evolution of P_c, we performed a simultaneous fit of our set of data for A and L excitons away from the puddle and L_p excitons. To minimize the number of free fitting parameters, we assumed no field-dependence of b_κ for the case of L_p excitons that exhibit a thermal population distribution, and set both the g-factors and the ratios r_0 equal for both L and L_p. Moreover, we fixed the A exciton g-factor to 4.0 [146, 148], and assumed a global temperature T for the entire set of data. With these parameters fixed, best simultaneous fit was obtained with $b_0 = 0.03$, 0.90, and 0.82 for A, L, and L_p; $r_0 = 0.03$ for A and 0.01 for L and L_p; $\delta = 0.012$ T^{-1} for A and 0.027 T^{-1} for L; $g_{VZ} = 4.4$ for L and L_p; $T = 9$ K. The corresponding evolutions of P_c for A, L, and L_p excitons are shown in Fig. 5.15a, b, and c, respectively. We note that the best fit yielded an effective temperature of $T = 9$ K consistent with local laser heating, and $g_{VZ} = 4.4$ for L and L_p excitons in agreement with elevated values reported for excitons localized in QDs [59–62].

The main effect of the model of Eq. 5.11 as compared to the model of Eq. 5.4 is the increased field dependence of the A exciton branching (δ increased by a factor of two from 0.006 T^{-1} to 0.012 T^{-1}), whereas the values of the zero-field branching ratio of b_0 for the valley flipping to the valley conserving rate are comparable for the two models. Most importantly, the model yields an estimate for r_0 for both A and localized excitons: best fit values of $r_0 = 0.03$ for A, and 0.01 for L and L_p correspond to $\tau_l/\tau_0 \simeq 17$ and 50, respectively. Taking the PL decay time of 4.5 ps for the A excitons in MoS_2 [161] that we do not resolve in our time-correlated PL experiments, we thus obtain an estimate for the longitudinal valley depolarization time of $\tau_l \simeq 80$ ps for A excitons. With the same scaling we estimate $\tau_l \simeq 230$ ps for localized excitons that exhibit PL decay dynamics dominated by the fast component below the resolution limit of our fiber-based setup with dispersion (as shown in Fig. 5.6b, only $\sim 10\%$ of the total PL intensity of both L and L_p excitons contribute to the slow decay component). The main difference for L and L_p populations stems from different branching during relaxation: while the upper valley polarization of L excitons is weakly yet increasingly protected with magnetic field (with a slope of 0.027 T^{-1}), the branching ratio of L_p excitons is independent of magnetic field. Given similar PL decay dynamics in the L and L_p bands, and similar branching ratios at zero magnetic field, we conclude that hot and thermal valley populations of localized excitons arise from field-dependent and field-independent branching ratios, respectively.

5.4.2 Valley depolarization analysis

The scheme of non-thermal, optically induced valley population imbalance is the opto-valleytronic counterpart of optical spin orientation in conventional semiconductors [166]. For the fundamental A exciton, rate-equation analysis [144] suggests that out-of-equilibrium K and K' valley populations result from both a finite branching of the optically excited valley polarization into valley flipping and valley conserving relaxation channels and a slow valley depolarization in the exciton ground state. In fact, valley depolarization times much longer than the exciton decay time underpin the non-thermal valley population regime [144]. Our analysis that accounts for intervalley thermalization in addition to finite branching of the photoexcited population yields best fits with $\tau_l/\tau_0 \simeq 17$ for A and 50 for L and L_p excitons. In contrast, the model with ideal initial polarization of the luminescent exciton states predicts $\tau_l/\tau_0 \simeq 9$ for A and 0.1 for L excitons, respectively. The discrepancies stem from the fact that the idealized model does not take into account the details of the valley pseudospin initialization in K and K' exciton ground states. Actually it holds only if the valley conserving relaxation significantly outcompetes the valley

flipping relaxation during the formation process of the K and K' excitons out of the selectively excited valley as in the case of A excitons in our experiment with near-resonant excitation. This does not apply to localized states, where significant population branching occurs upon relaxation, and different branching scenarios determine the non-thermal and thermal populations of L and L_p excitons: for the former, alike for A excitons, the valley polarization is increasingly accumulated in the photoexcited upper valley due to a reduction of branching with magnetic field, while for the the latter defect-assisted relaxation is likely to render the branching field-independent.

The regime of $\tau_\mathrm{l}/\tau_0 \gg 1$ identified by our analysis for both A and L excitons in monolayer MoS_2 yields upper bounds on the longitudinal valley depolarization times of $\tau_\mathrm{l} \simeq 80$ ps for A and 230 ps for L and L_p excitons if we take the PL decay time of $\tau_0 = 4.5$ ps for both the A excitons in MoS_2 [161] and the dominant decay timescale of localized excitons in our sample (see Section 5.2.3). In absolute terms, the longitudinal depolarization time of A excitons might be shorter if scaled to a more rapid exciton decay potentially present in our CVD-grown MoS_2 flakes but inaccessible in our experiments due to limited temporal resolution. In relative terms, however, our finding of $\tau_\mathrm{l} \gg \tau_0$ is in accord with previous results on WSe_2 [144]. At the same time it is contrasted by the theoretical estimate $\tau_\mathrm{l} \simeq \tau_0 \simeq 1$ ps for the valley depolarization dynamics in the presence of long-range exchange [168, 169] which in turn is an integral part of the finite-branching model [144]. This caveat is qualitatively resolved by the notion of exchange-mediated valley depolarization timescales beyond 1 ps for luminescent excitons with small center-of-mass momentum away from the light-cone edges [168, 169]. For quantitative consistency, however, efforts in theory and experiment on the details of exciton valley dynamics in the presence of valley conserving and flipping relaxation channels and external magnetic fields are required beyond the scope of this work.

5.5 Wide-field opto-valleytronic imaging

We return to polarimetric mapping to demonstrate that the main valleytronic signatures of layered TMDs discussed above can be obtained with direct two-dimensional imaging. To this end we defocused the excitation laser to illuminate a spot of ~ 100 µm diameter and replaced the single-mode fiber in the detection path with an imaging lens and a standard room-temperature CCD[6]. The resulting optical system images a sample area of $\sim (0.1 \times 0.1)$ µm^2 onto a single pixel of the CCD array. A tunable band-pass filter placed before the CCD imaging lens was used to select

[6]Point Grey, GS3-U3-14S5M-C with pixel size of (6.45×6.45) µm^2 and well depth of 17 ke$^-$

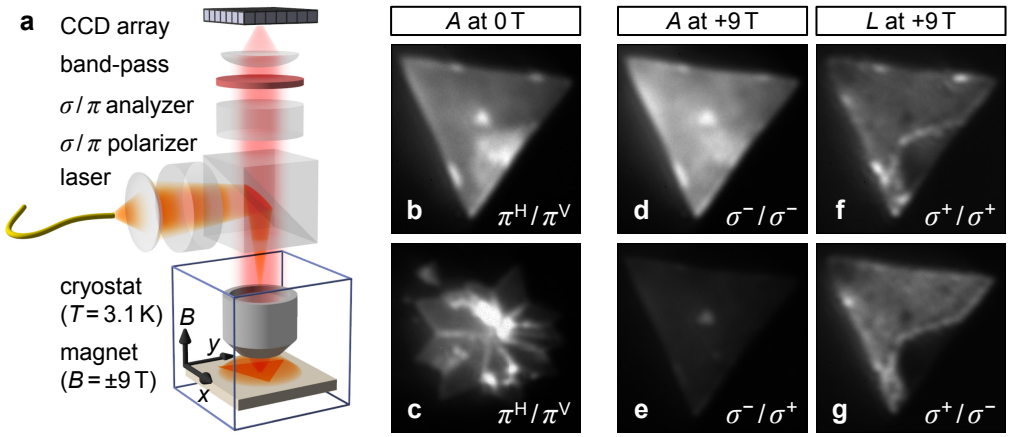

Figure 5.16: Wide-field linear and circular polarimetry. **a**, Setup schematics for wide-field imaging: the excitation laser was defocused to illuminate a spot of $\sim$ 100 µm diameter. Exciton-specific photoluminescence was spectrally selected with a band-pass filter and imaged onto a camera with a 50× effective magnification. **b**, **c**, Images of the A exciton band in cross-linear (π^{H} horizontal excitation / π^{V} vertical detection) configuration for the triangular and the star-shaped crystal, respectively. The bright regions visualize bilayer and valley decoherence sites as in Fig. 5.7e and f. **d**, **e**, Images of the A exciton band in the single-crystal triangle recorded in co-circular (σ^- excitation / σ^- detection) and cross-circular (σ^- excitation / σ^+ detection) configurations in a magnetic field of +9 T. **f**, **g**, Same for the L exciton band in σ^+/σ^+ and σ^+/σ^- configurations, respectively. All images were acquired with equal integration times and a gamma encoding of 0.7. The sample was cooled to 3.1 K; laser excitation was at 637 nm.

exciton-specific bands, and polarimetric imaging was performed either in the circular or linear basis. A fs-OPO[7] was used to excite the PL at 637 nm with an average power density of $\sim$ 200 W/cm^2 at the sample. The corresponding setup schematics are shown in Fig. 5.16a.

Polarimetric images of the two representative flakes recorded in cross-linear configuration (orthogonal excitation and detection polarizations) within the A exciton band are shown in Fig. 5.16b and c. In the given configuration, the high intensity features correspond to bilayer and dephasing regions of the flakes. Apart from a scaling factor, the images are equivalent to gray-scale versions of the false-color maps in Fig. 5.7e and f. They demonstrate qualitatively that disorder in monolayer TMDs can be visualized directly with a rather simple and efficient imaging technique.

It is also straight forward to apply the technique in the circular basis. The images of Fig. 5.16d and e show the PL intensity of A excitons in σ^- co-circular and cross-circular polarimetry for a magnetic field of +9 T. The non-thermalized A ex-

[7] Coherent, Mira-OPO

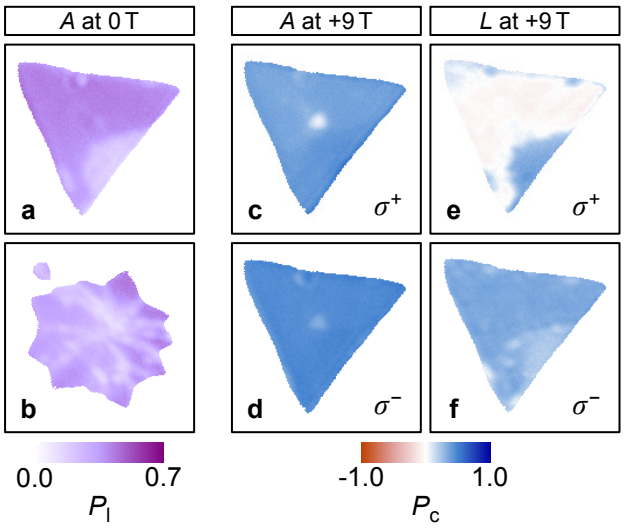

Figure 5.17: **a**, **b**, Linear polarimetric profiles P_l of spectrally filtered A excitons in single- and poly-crystalline MoS_2, respectively, obtained with wide-field imaging. **c**, **d**, and **e**, **f**, Circular polarimetric profiles P_c of A and L excitons within the respective band-pass windows in an external magnetic field of +9 T. The data were recorded at 3.1 K with excitation at 637 nm and σ^+ polarization in **c** and **e**, and σ^- polarization in **d** and **f**.

citon valley population of the upper Zeeman branch K' addressed by σ^- excitation can be readily deduced from Fig. 5.16d and e; for a fully thermalized valley population the flake in Fig. 5.16d would be less intense than in Fig. 5.16e. The analogous set of measurements for the L exciton band in σ^+ co- and cross-polarized configurations (Fig. 5.16f and g) illustrates the negative degree of circular polarization: the cross-polarized image of the flake is brighter (except for the puddle and a few hotspots of point-like QD emission) in accord with the raster-scan polarization image of Fig. 5.11c.

As in confocal polarimetry, polarization-resolved wide-field imaging can be used to construct polarimetric profiles of valley polarization and valley coherence. To demonstrate the quantitative character of the technique, we show in Fig. 5.17a–f the P_l and P_c profiles of the single-crystal MoS_2 triangle obtained with wide-field polarimetry. Note that the opto-valleytronic profiles are in excellent quantitative agreement with confocal data shown in Figs. 5.7 and 5.11 if one takes into account the reduction of P_l and P_c due to wider spectral bands of the band-pass filter used in wide-field polarimetry.

The advantage of the wide-field imaging technique is that it reduces the integration time for opto-valleytronic profiling whenever full spectral information at each pixel of the map is not required. Ultimately, for an image size of $\sim (20\times20)$ μm^2 with a pixel size of $\sim (0.4\times0.4)$ μm^2 an acquisition acceleration of at least $\sim 2.5\times10^3$ can

be obtained with polarimetric profiling in wide-field imaging as compared to confocal raster-scanning with the same spatial resolution, spectral width, noise level, and transmission characteristics. For this estimation we neglected the confocal scanning time and assumed equal excitation power densities of the imaging techniques as well as shot-noise limited signals. We note that for our confocal raster-scan polarimetry the scanning time was a factor of two longer than the integration time, and the transmission properties were a factor of ten lower than for wide-field imaging.

5.5.1 Implications of reduced power density

For wide-field optovalleytronic imaging the average power density ($\sim$ 200 W/cm^2) was a factor of $\sim$ 150 and $\sim$ 500 lower than in confocal measurements with the excitation laser at 637 nm (CW power density of $\sim$ 25 kW/cm^2) and 532 nm (CW power density of $\sim$ 94 kW/cm^2), respectively. In the following, we discuss the main implications of the reduced power density for the observations in wide-field imaging and polarimetry.

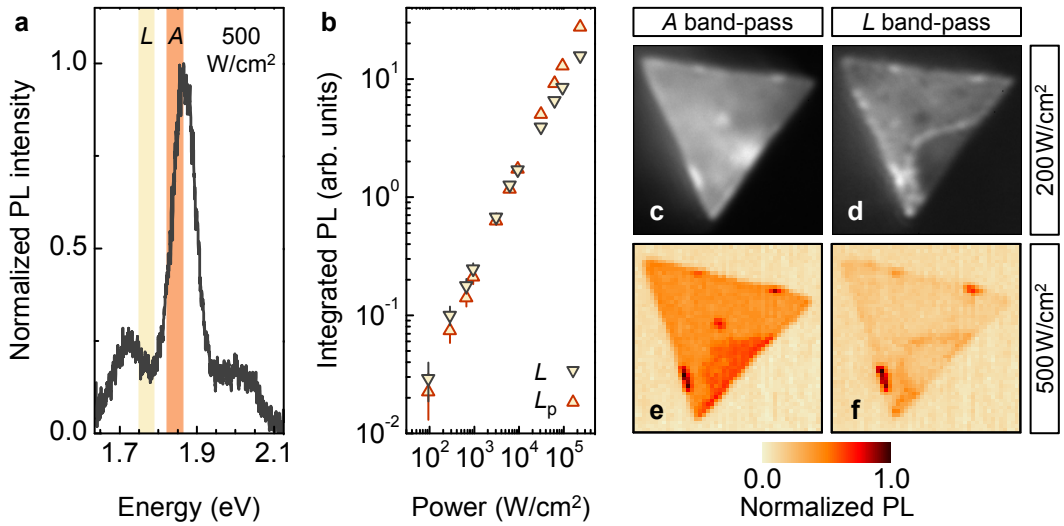

Figure 5.18: Confocal and wide-field imaging at low excitation power densities of $\sim$ 500 W/cm^2 and $\sim$ 200 W/cm^2, respectively. **a**, Confocal low-power excitation spectrum with colored A and L exciton bands used for exciton-selective photoluminescence imaging. **b**, Photoluminescence intensity of L excitons as a function of excitation power away from the puddle (L) and in the puddle (L_p). **c**, **e**, Photoluminescence intensity profiles of A excitons for the triangular flake under low-power excitation in wide-field and confocal imaging, respectively. **d**, **f**, Same but for the L exciton band. The excitation wavelength was 637 nm in **c** and **d**, and 532 nm otherwise. The images in **c** and **d** were acquired with linear gamma encoding. All data were recorded at 3.1 K.

To compare the confocal and wide-field imaging modes we recorded additional PL spectra and intensity maps in the confocal setup configuration at reduced power densities. In Fig. 5.18 we present data recorded in the regime of low power excitation for the single-crystal MoS_2 triangle. A confocal PL spectrum recorded at an excitation power density comparable to that of the wide-field imaging mode is shown in Fig. 5.18a. Colored bands indicate the spectral intervals that were used for the evaluation of confocal PL intensity maps in Fig. 5.18e and f for A and L excitons, respectively. The bands were selected to match the setting of the band-pass filter in wide-field imaging.

As shown in Fig. 5.18b, the PL intensity of L excitons is not saturated at low excitation powers. This results in an increased intensity ratio of L to A exciton PL in the confocal spectrum of Fig. 5.18a as compared to the data in Fig. 5.1b. Moreover, since the saturation responses of L excitons away from the puddle and in the puddle are different (the respective data are denoted as L and L_p in Fig. 5.18b), one expects a crossover in the relative PL intensities of defect-bound excitons in the puddle and on a regular position of the flake. This effect is observed in PL imaging at low excitation power densities: both wide-field (Fig. 5.18d) and confocal (Fig. 5.18f) images of the monolayer triangle show a more intense L exciton PL away from the puddle, whereas at high excitation power densities the L exciton PL in the puddle is more intense (Fig. 5.2b). The more pronounced appearance of hotspots in the PL intensity profiles of A excitons under low-power illumination (Fig. 5.18c and e) as compared to the PL intensity map under high-power illumination (Fig. 5.2a) is also attributed to saturation effects.

5.6 Conclusions

Our study identifies both raster-scan and wide-field polarimetric imaging as viable tools to explore the valley pseudospin physics in layered TMD semiconductors. Experiments that do not require the full spectral information but are meaningful within a limited PL bandwidth will benefit from a decrease of the measurement time required to achieve the same signal-to-noise performance in wide-field and hyperspectral raster-scan polarimetry. For (20×20) μm^2 sample areas like in Fig. 5.16 we estimate a speed-up by at least three orders of magnitude for wide-field imaging as compared to raster-scanning which enables rapid large-scale monitoring of the sample. Clearly, our polarimetric imaging technique is not limited to MoS_2 crystals but establishes novel analytical means for the entire class of layered TMD semiconductors and heterostructures, and can be extended to spin-polarization imaging of conventional semiconductor quantum wells [166]. It will perform most efficiently when applied on TMD materials with spectrally separated exciton and trion emis-

sion bands, a condition accessible for chemically treated MoS_2 [176]. By virtue of simplicity and efficiency our technique will facilitate the analysis of TMD materials in terms of crystalline and environmental disorder and, combined with a microscopic model for the optical valley initialization, it will enable quantitative access to site-dependent valley pseudospin dynamics. Moreover, our findings encourage the experimental exploration of topological exciton-polaritons by identifying sufficiently large regions of low valley depolarization and decoherence in monolayer TMDs for the realization of periodic exciton potential arrays that are key to the implementation of topolaritonic devices [177].

Chapter 6

Imaging of charge doping in monolayer molybdenum disulfide

The work presented in this chapter reports on the photophysics of doped chemical vapor deposition grown molybdenum disulfide monolayers using cryogenic hyperspectroscopy. Formation of robust negatively charged trions and their spectral characteristics are demonstrated on the basis of electrostatically tunable and chemically doped crystals on silicon substrates. For the latter as-grown sample, hyperspectral raster-scan photoluminescence is used to reconstruct excitonic landscapes and doping profiles, which reveal spatial charge inhomogeneities within the material. Complementary strain signatures are distinguished from charging effects in the optical response of the monolayer by means of two-dimensional Raman spectroscopy.

6.1 Introduction and overview of the experiment

Direct band gap optical transitions are dominated by excitonic photophysics of TMD monolayers such as MoS_2. Inherently two-dimensional material properties with strong confinement in space and reduced dielectric screening lead to formation of tightly bound electron-hole pairs with binding energies exceeding several hundred meV [15–17]. The two lowest band-edge excitons, commonly referred to as A and B, reflect the spin-orbit split valence and conduction subbands at the K valleys of the hexagonal Brillouin zone [9, 10]. Apart from neutral excitons, large Coulomb interactions in TMDs call forth pronounced many-body phenomena where quasi-particles consisting of three or more charge carriers are formed, such as trions [20, 21] and biexcitons [22, 23], or Fermi polarons [24].

The quantum kinetics responsible for the photogeneration of stable many-body systems are complex [178]. Trions for example may form through coalescence of an exciton with an extra charge within the Fermi sea of excess charge carriers or evolve from an electron-hole plasma in a non-equilibrium state [179]. In most cases the number of photogenerated trions is determined by the former channel and thus depends on the doping level of the semiconductor. Here we explore electrically and chemically doped monolayer MoS_2 with confocal PL spectroscopy at cryogenic temperatures. Our samples were grown by CVD with methods adopted from Ref. 13 (see Appendix A for synthesis details) and examined with confocal microscopy with an experimental setup as described in the previous chapter. At first we confirm the formation of negatively charged A^- trions for an MoS_2 flake incorporated in a field effect device. Next, using two-dimensional excitonic and Raman imaging of a chemically doped monolayer crystal, we identify B^- trion PL in MoS_2. Moreover, we discuss and compare charge doping profiles in terms of the average number of electrons per A and B-type excitons.

6.2 Opto-electronic properties of a charge carrier tunable monolayer

A schematic of our monolayer MoS_2 field effect transistor[1] is shown in Fig. 6.1a. Electrical contacts on top of a MoS_2 monolayer triangle were defined by means of laser lithography followed by deposition of titanium (3 nm) and gold (50 nm). The semiconducting layer was separated by 100 nm of SiO_2 from a highly p-doped silicon substrate, which was used as the back gate of the device. An atomic force microscopy (AFM) image showing the monolayer, where the electrical contacts are colored green,

[1] Details of device fabrication can be found in Ref. 180.

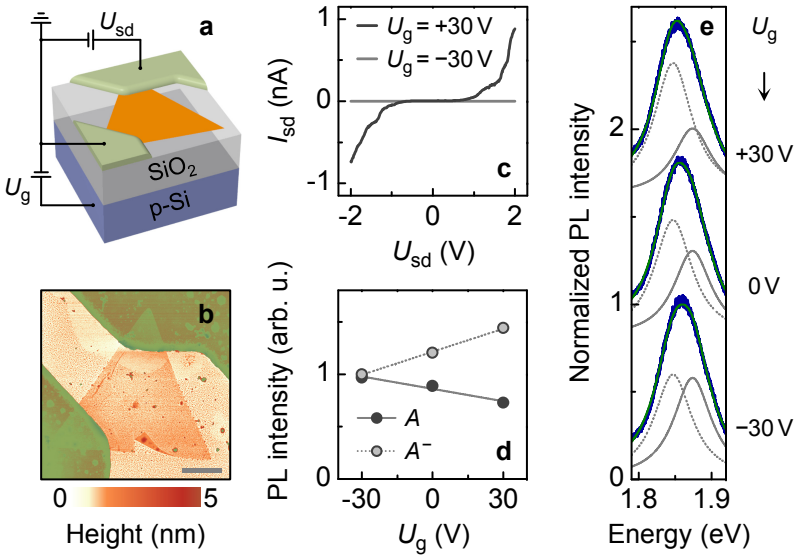

Figure 6.1: **a**, Schematic of a field effect transistor based on monolayer MoS_2 with source and drain contacts on top of p-doped Si substrate acting as back gate with 100 nm SiO_2 in between. **b**, Atomic force micrograph of the device (scale bar is 5 µm). **c**, Source-drain current (I_{sd}) through the flake as a function source-drain voltage (U_{sd}) for two gate voltages (U_g). **d**, A exciton and A^- trion photoluminescence excited by 532 nm laser as a function of U_g; solid and dotted lines are linear guides to the eye. **e**, Corresponding photoluminescence spectra (blue) with double-Lorentzian fits (green) allowing to extract A (solid gray) and A^- (dotted gray) contributions; traces were offset for clarity. Data in **c**–**e** were obtained at a temperature of 4.2 K.

is shown in Fig. 6.1b. The low temperature electrical functionality of the device was inspected by measurements of current-voltage characteristics between the source and drain contacts for different back gate voltages (Fig. 6.1c). Weak capacitive and leakage currents through the oxide between the back gate and the flake were averaged and subtracted from the recordings to obtain the residual current through the flake. The non-Ohmic dependence of the source-drain current as a feature of thermally unannealed devices [181, 182] indicates to sizable Schottky barriers which hinder ideal carrier injection into the semiconducting layer. Regardless, the transistor exhibited n-type conductivity through the flake modulated by the back gate voltage.

The tunability of the free electron density was also manifested in the optical properties of the device. On SiO_2 neutral A excitons and negative A^- trions in TMD monolayers with a binding energy of $\sim$ 30 meV are simultaneously visible in PL spectroscopy [20, 21]. In Fig. 6.1d we present A and A^- PL intensities as a

function of the applied gate voltage for CW excitation with a 532 nm laser[2]. For zero gate bias the unbalanced intensities of A and A^- correspond to a charge carrier density on the order of $\sim 10^{12}$ cm^{-2} [183], a typical value for substrate-induced background doping of MoS_2 on SiO_2 [171, 184]. As the free electron density in the monolayer was increased for a gate voltage of 30 V we observed an increase of A^- accompanied by a simultaneous decrease of A PL. Whereas for a gate voltage of -30 V the opposite effect was measured in agreement with a reduced doping level. The data were derived from integrated Lorentzian fits of the A and A^- resonances separated by the trion binding energy, where the sum of the two fits closely matched the measured PL traces (Fig. 6.1e). For the applied gate voltage range we observed a constant trion binding energy.

6.3 Imaging excitons and trions in a chemically doped monolayer

Chemical doping provides another approach to tune PL and trion formation in monolayer TMDs [185]. The often accompanying intentional or unintentional local defect sites in layered semiconductors also entail exciton localization [170]. We expand our analysis by examining chemical doping of a previously studied MoS_2 single crystal (see former chapter) from the same CVD batch as the sample of Fig. 6.1, without incorporation in a field-effect device. By raster-scanning the sample with respect to diffraction-limited confocal excitation and detection spots PL of A and B excitons was collected for two-dimensional exciton imaging. At each pixel of the raster-scans PL intensities were decomposed into distinct exciton PL profiles. Best fits were obtained by sums of five Lorentzians accounting for the observed resonances. Four distributions with fixed energies and linewidths were used to fit A and B excitons and their trion counterparts A^- and B^- [172]. Lower energy localized excitons were accounted for by an additional Lorentzian with variable peak energy and linewidth parameters. Results for A and B-type excitons and trions are shown in Fig. 6.2a–d. Remarkably, we observed no indication for inhibited relaxation of B excitons into the energetically favored lower-lying A exciton states. This sizable out-of-equilibrium population of bright B exciton states indicates that relaxation pathways from the B to the A exciton manifold which require spin or valley flips of both electrons and holes [109] are slow as compared to the radiative B exciton recombination time. We conclude that inefficient spin-flip as well as intervalley scattering represent main relaxation bottlenecks for B excitons and trions in monolayer TMDs.

[2]CNI, MLL-III-532-50-1

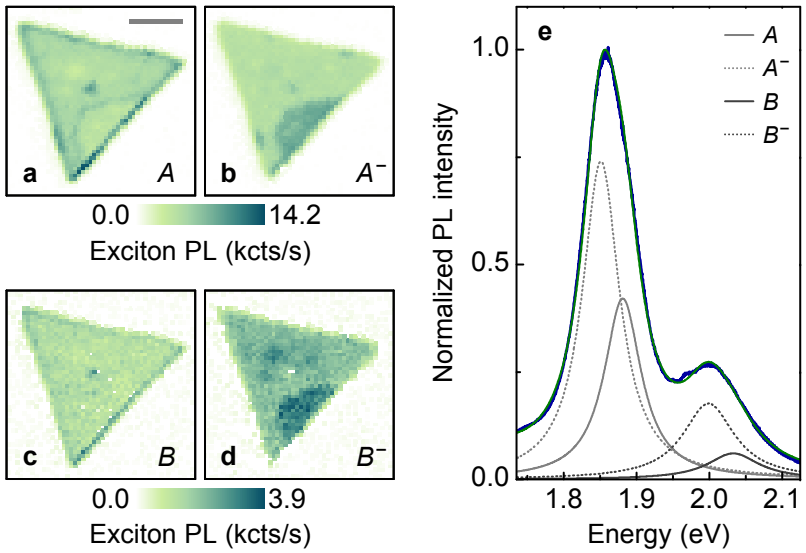

Figure 6.2: **a**, **b**, Exciton photoluminescence raster-scans of a representative MoS_2 flake for A excitons and A^- trions (scale bar is 5 µm). **c**, **d**, Same for B excitons and B^- trions. The images in **a**–**d** were constructed from respective fits of integrated Lorentzian contributions to measured spectrally-resolved photoluminescence traces; pixels with signal-to-noise ratios of less than ten were set to zero. **e**, Normalized photoluminescence spectrum (blue trace) with fits showing contributions from A and B-type excitons and trions (gray traces with inset labels). Localized excitons below $\sim$ 1.75 eV were considered with an additional Lorentzian; green trace shows the sum of all five Lorentzians. All data were measured at 3.1 K with 532 nm excitation.

Fig. 6.2e shows a representative spectrum with the described exciton contributions: A and B excitons at 1.88 eV and 2.03 eV with inhomogeneously broadened FWHM linewidths of 60 meV and 85 meV, respectively, the redshifted trions shared their linewidths with the corresponding excitons. Our analysis suggests that the B^- negatively charged trion counterpart to A^- is also stable with a slightly larger trion binding energy of 34 meV. The small difference in the trion binding implies similar extends of electron and hole wavefunctions for A and B excitons. Our findings add the theoretically predicted negatively charged B^- trion [172] to the class of luminescent exciton transitions in MoS_2 and complement the observation of B^- trions in reflectance contrast measurements in WS_2 [186], a related TMD material.

6.3.1 Characterization of local strain fields

Apart from charge doping, opto-electronic properties of layered semiconductors are also known to be sensitive to strain fields. Previous reports have shown band-gap energy reductions of 48 meV per percent of applied uniaxial strain in monolayer

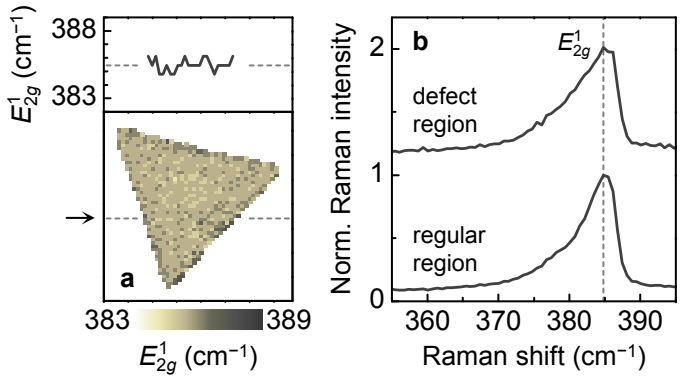

Figure 6.3: a, Raman shift map of the E^1_{2g} mode for the MoS_2 crystal shown in Fig. 6.2 (bottom panel); line-scan of the E^1_{2g} peak frequency across the direction indicated by the arrow (top panel). The mode assignment corresponds to common bulk notation in MoS_2 at the Γ point of the Brillouin zone. **b**, Normalized Raman spectra of the E^1_{2g} mode for representative regular (bottom) and defect-doped (top) monolayer flake positions. The traces were vertically offset for clarity and the dashed line is a guide to the eye. All data were recorded with single-mode laser excitation at 639 nm. The sample temperature was 3.1 K.

MoS_2 [187–189]. Thus, spectral signatures of A and B-type excitons in strained and doped TMD monolayers may appear similar. To exclude the influence of local strain fields applied through potential contact variations in the interface between the sample and the underlying substrate, we inspected the crystal structure of the MoS_2 flake discussed in Fig. 6.2 by means of Raman spectroscopy.

Vibrational modes in TMDs such as the E^1_{2g} mode describe deformations in the plane of layered semiconductors and are the ones most affected by strain. In the limit of a monolayer the Raman wavenumber of the E^1_{2g} mode is known to shift with a rate of -2.1 cm^{-1} per percent of uniaxial strain [190] without dependence on the charge doping concentration [191]. Fig. 6.3a maps the Raman shift of E^1_{2g} for the studied MoS_2 crystal using near-resonant single-mode laser[3] excitation at 639 nm. The homogenous profile within the resolution limit of our setup (~ 0.6 cm^{-1}) suggests strain variations across the crystal of at most $\sim 0.3\%$. These variations could only account for exciton redshifts of less than half of the measured binding energies of A^- and B^- trions. In fact, high signal-to-noise Raman spectra at representative chemically doped positions of the flake and regular monolayer positions revealed identical wavenumbers for the E^1_{2g} mode (Fig. 6.3b). We therefore conclude that the MoS_2 monolayer is locally doped and not substantially strained.

[3]New Focus, Velocity TLB-6704

6.3.2 Characterization of charge doping profiles

In the following, we qualitatively discuss local charge variations in the chemically doped MoS_2 monolayer using the ratio of densities of charged to neutral excitons. To this end we compute charge doping profiles in terms of exciton PL intensities as $A^-/(A+A^-)$ for the ground state excitons and $B^-/(B+B^-)$ for the spin-orbit split excitons (Fig. 6.4a and b, respectively). The profiles highlight in red specific regions with higher electron concentration, among them the surface-contaminated puddle at the lower edge of the crystal, and in blue areas with low electron doping, such as the edges of the triangle. Under the assumption of trion formation exclusively via exciton-electron Coulomb interactions on timescales fast compared to the exciton recombination time, such profiles provide a quantitative means to image the local doping level by employing the mass action model [21]. However, this simplification implies negligible populations of either neutral excitons or free electrons in steady-state at cryogenic temperatures of a few Kelvin, where the available thermal energy is two orders of magnitude smaller than the trion binding energy. Our measurements of the CVD-grown sample suggest that A^- and B^- trion formation competes on comparable timescales with the population decay of their neutral A and B counterparts, which decay within a few picoseconds [161, 192]. This is in accord with measured A^- trion formation times of $\sim$ 1 ps in MoS_2 [193] and $\sim$ 2 ps in $MoSe_2$ [194] monolayers. The similarity of the maps in Fig. 6.4a and b additionally shows that the trion photogeneration dynamics of A^- and B^- are not too distinct.

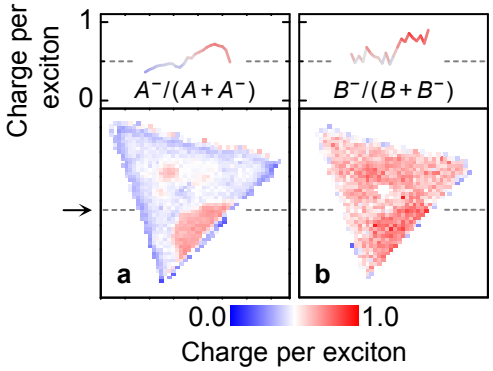

Figure 6.4: a, Charge doping profile in units of one electron charge per exciton for the MoS_2 flake from Fig. 6.2 (bottom panel) and corresponding line-scan across the direction indicated by the arrow (top panel). The map was computed as $A^-/(A+A^-)$, where A (A^-) are the exciton (trion) photoluminescence intensities. **b**, Analogous doping profile (bottom) and line-scan (top) for B-type excitons, computed as $B^-/(B+B^-)$ with B excitons and B^- trions. Pixels with signal-to-noise ratios of less than 40 in **a** and 20 in **b** were set to zero. All data were acquired at 3.1 K with 532 nm excitation.

6.4 Conclusions

In summary, our findings reveal variations of the charge carrier doping profile for TMD monolayers in uncontrolled environments. Doping variation was observed in a field effect transistor based on CVD-grown monolayer MoS_2 in form of a spectral weight shift between neutral exciton and negative trion PL. For a similar monolayer without electrical contacts, inhomogeneous distributions of trions due to local unintentional chemical doping were identified using the combination of two-dimensional exciton and Raman mapping. Apart from the lower energy A^- trions, our excitonic landscapes expose the formation of stable B^- trions with similar trion binding energies of 34 meV. Moreover, the demonstrated imaging method provides a non-invasive means for qualitative studies of charge doping levels in two-dimensional TMDs.

Chapter 7

Summary and perspectives

In the context of this thesis, optical properties of low-dimensional condensed matter systems were explored using extensive spectroscopic methods at ambient conditions, cryogenic temperatures down to 3.1 K, or high magnetic fields up to 9 T. The presented results were to a large extent realized in home-built experimental setups. One of the addressed materials were nanoscale quantum emitters embedded in polymer matrices consisting of PMMA as a widespread experimental setting for fundamental spectroscopic studies. Surprisingly, the samples exhibited localized fluorescent hotspot emission in the visible spectral range even without purposely deposited nanoemitters, and thus signified optical contamination as an easily overseen circumstance [195] in otherwise optically inactive polymers. Using two-dimensional confocal FL imaging and vibrationally resolved spectroscopy, the studies revealed polymer solvent-specific fluorescent molecules as the main source of contamination and could not confirm previous assignments to intrinsic defects in silica substrates [54]. Depending on the solvent, the spectral signatures of the aromatic hydrocarbons exhibited prominent features of rylene dye molecules composed of naphthalene units as well as dyes derived from acene chains such as alizarin with different relative intensities. The projected surface densities of the emitters in all samples were similar with ~ 0.1 molecules per μm^2 for matrix thicknesses of ~ 200 nm, corresponding to over a million PMMA molecules and orders of magnitude more solvent molecules for every fluorescent contaminant. Given the restrictions imposed by the technological advancement of ultrapure polymer solvents, it will presumably remain a challenging task to completely remove all contamination.

Apart from identifying the FL origin, the findings contribute to the clarification of misinterpretations of spectral features to the ever-increasing family of nanoscale emitters [53, 70]. Moreover, the stable quantum light emission of the contaminants, without blinking or bleaching effects on hour timescales under CW excitation, represents a reliable and cheap alternative to more sophisticated single photon sources.

The FL quantum yield of the molecular emitters, as a key parameter for the conversion of absorbed photons into the emitted photons, was modest but not negligible with estimated values of $\sim 5\%$ at room temperature rising up to 30% at cryogenic temperatures.

The second focus of this thesis was directed towards single-layered molybdenum disulfide grown by CVD, as a representative direct band gap semiconductor within the class of atomically thin TMDs. The opto-electronic properties of these materials are dominated by excitonic effects at the two inequivalent K and K' valleys, which are coupled by time-reversal symmetry and described by valley pseudospins [25]. In analogy to spin-based operations [196], the binary valley pseudospin provides an additional quantum degree of freedom to encode, process, or store quantum information. Even though the idea to manipulate the valley pseudospin for valleytronic applications is not new, its applicability has been rather limited in conventional systems with useful electronic valleys until the emergence of graphene-like materials with broken inversion symmetry [26]. Due to strong spin-orbit interactions, the valley pseudospin optics in these hexagonal crystals can be addressed selectively to generate valley polarization [131–133] or coherently to create valley coherence [134] using circularly or linearly polarized light, respectively.

Using this ideal interface, a novel two-dimensional spectropolarimetric approach was pioneered to image spatial variations of optically-generated valley quantum states in terms of valley-specific PL for extended monolayer crystals. This opto-valleytronic imaging enabled direct visualization of multilayer formation with restored inversion symmetry and low valley polarization, as well as sites of crystalline disorder including edges, grain boundaries, or surface contaminants which cause valley decoherence. The comprehensive studies were based on two types of cryogenic polarimetry: raster-scan spectropolarimetry, where full spectral information of the PL polarization is tagged to each image pixel, and wide-field polarimetric imaging in a limited spectral band. While the first method provided full spectral information to establish scientifically meaningful image interpretation, the second mode enabled significant reduction in the image acquisition time for exciton-specific spectral bands. Scaled from microscopic to macroscopic length scales the developed imaging technique will allow both fast and efficient inspection of wafer-sized atomically thin semiconductors with opto-valleytronic functionalities [197].

The hyperspectral capabilities of the experiment furthermore enabled possibilities to directly image local charge doping profiles, computed from relative spatial distributions of excitons and trions, and strain landscapes using two-dimensional Raman raster-mapping. In terms of charge doping, the simplicity of the method paired with its non-invasive nature may provide a qualitatively viable imaging tool for molybdenum-based TMD semiconductors, where the ground states are spin-

bright excitons. In particular for MoS_2 monolayers, it will be most effective for well-separated and long-lived excitons and trions hosted by highest quality systems at cryogenic temperatures that are encapsulated in hexagonal boron nitride [198] or treated by a superacid [176, 199].

The aptitude of the developed imaging techniques as instruments for the characterization of atomically thin TMDs critically relies on finite populations of bright excitonic states, which govern the material quantum efficiency for light emission. At the same time, bright excitons with finite center-of-mass momenta are however particularly susceptible to valley depolarization through long-range electron-hole exchange interaction [200, 201]. This mechanism couples two bright excitons with opposite valley pseudospins without the involvement of free carrier spin-flip scattering or intervalley scattering, which would require phonons with large momentum or atomic-scale impurities. For spin-dark excitons, on the other hand, exchange coupling is orders of magnitude lower [202] or zero for pure spin states [201]. On the example of a representative MoS_2 monolayer, valley depolarization dynamics were explored by modeling opto-valleytronic PL data in external magnetic fields perpendicular to the crystal plane with rate equation analysis. This strategy, based on the K and K' degeneracy breaking through the valley Zeeman effect, unveiled direct access to exciton-specific longitudinal valley lifetimes of at most ~ 80 ps for delocalized excitons and three times as much for defect-bound excitons. In both cases, the valley depolarization times were considerably longer than the radiative lifetimes of the excitons of less than ten picoseconds, signifying the likely involvement of long-lived dark states. Despite this complexity, intervalley exchange coupling seems to limit opto-valleytronic manipulations of luminescent monolayer excitons, with finite wavevectors within the light cone, to picosecond timescales.

An attractive perspective to prolong the valley depolarization timescale could be supplied by type-II TMD heterobilayers such as $MoSe_2$-WSe_2, where the lowest energy excitons are interlayer excitons with electrons and holes in the $MoSe_2$ and WSe_2 layers, respectively. For such interlayer excitons exchange coupling is greatly reduced owed to a smaller overlap of the electron and hole wavefunctions, therefore, they can feature longitudinal valley lifetimes of tens of nanoseconds [203]. This value can be further increased to the microsecond range through feeding by intralayer dark excitons with suppressed valley mixing in an external out-of-plane magnetic field [204]. Another interesting aspect for future opto-valleytronic technologies could be the use of material defects in TMDs to manipulate or engineer valley properties. For instance, in the present work it was shown that defect-bound excitons in Zeeman-split valleys of an extended MoS_2 monolayer can exhibit either thermal or non-thermal optically-induced valley populations. Further, since defects localize excitons

in real space, they also offer a large momentum uncertainty and could potentially enable the realization of a valley switching mechanism, which can flip the valley index of a target quantum state.

Appendix A

Sample fabrication

MoS_2 samples

MoS_2 crystals studied in this thesis were grown using CVD by H. Yamaguchi with support from A. D. Mohite at the Los Alamos National Laboratory, USA. As described in the Supplementary Information of Ref. P2, SiO_2/Si substrates with MoO_3 seeding particles were placed in a quartz furnace in the presence of sulfur powder. The furnace was heated to ~ 900°C for 15 min with a flow of inert gases (N_2 and Ar) under atmospheric pressure. After cooling down to room temperature, synthesized MoS_2 crystals were transferred onto p-doped SiO_2/Si substrates with a conventional PMMA transfer method [205]. The PMMA was removed by rinsing the resulting sample with MoS_2 on SiO_2/Si in an acetone bath for three cycles of 15 min. Optical and AFM images of typical MoS_2 monolayer flakes after transfer onto SiO_2/Si are shown in Fig. A.1 (reproduced from the Supplementary Information of Ref. P2).

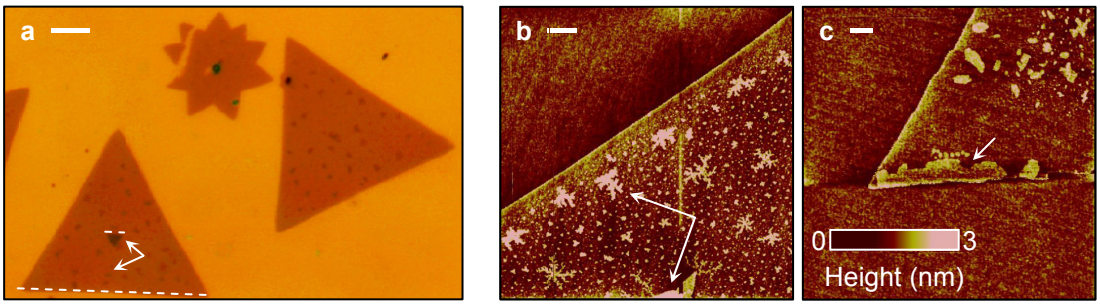

Figure A.1: **a**, Optical image and **b**, **c**, atomic force micrographs of monolayer MoS_2 grown by chemical vapor deposition. The scale bars are 10 μm in **a**, and 2 μm in **b** and **c**. Arrows indicate seeds of bilayer formation on top of monolayer flakes in **a** and **b**. Note the 180° misorientation of the large monolayer and the small bilayer triangles characteristic of ideal Bernal stacking indicated by the white dashed lines in **a**. An example of an extended region of surface contamination of a single-crystal triangle is indicated by the arrow in **c**.

Dielectric substrates and PMMA samples

The samples in Chapter 3 were prepared in a clean room environment. Unless stated otherwise, substrates were cleaned by initial sonication in acetone (Technic, acetone Micropur VLSI) for 5 min, followed by isopropanol (Technic, propan-2-ol Micropur VLSI) for 5 min, and finally exposed for 1 min to oxygen plasma. Polymer covered samples were prepared by spin-coating $\sim$ 10 µl of PMMA onto oxygen plasma-treated fused silica (CrysTec) and other dielectric substrates (quartz and sapphire). An ellipsometer was used to adjust the spin-coating parameters for a film thickness of 200 nm. The films were obtained from commercial PMMA formulated in anisole with a molecular weight of 950K (MicroChem, 950PMMA A4 resist for electron-beam lithography). The spin-coated PMMA film was left to dry at ambient conditions. Optionally, the samples were baked at 180°C for 90 s on a hot plate. For freely suspended PMMA, a perforated silicon nitride membrane (PELCO) was drop-casted and baked to ensure mechanical stability. Control experiments were carried out with 4% of 450K PMMA resin (DuPont, Elvacite 2041) diluted in 96% of chlorobenzene (Merck, 801791), methyl isobutyl ketone (Technic, MIBK Micropur VLSI), or toluene (Sigma-Aldrich, 179418).

References

[1] M. Bass, C. DeCusatis, J. Enoch, V. Lakshminarayanan, G. Li, C. Macdonald, V. Mahajan, and E. Van Stryland. *Handbook of Optics, Third Edition Volume II: Design, Fabrication and Testing, Sources and Detectors, Radiometry and Photometry* (McGraw-Hill, Inc., 2009).

[2] A. K. Geim. *Nobel Lecture: Random walk to graphene*. Rev. Mod. Phys. **83**, 851–862 (2011).

[3] K. S. Novoselov. *Nobel Lecture: Graphene: Materials in the Flatland*. Rev. Mod. Phys. **83**, 837–849 (2011).

[4] K. S. Novoselov, D. Jiang, F. Schedin, T. J. Booth, V. V. Khotkevich, S. V. Morozov, and A. K. Geim. *Two-dimensional atomic crystals*. Proc. Natl. Acad. Sci. USA **102**, 10451–10453 (2005).

[5] F. Xia, H. Wang, D. Xiao, M. Dubey, and A. Ramasubramaniam. *Two-dimensional material nanophotonics*. Nat. Photonics **8**, 899–907 (2014).

[6] L. Britnell, R. M. Ribeiro, A. Eckmann, R. Jalil, B. D. Belle, A. Mishchenko, Y.-J. Kim, R. V. Gorbachev, T. Georgiou, S. V. Morozov, A. N. Grigorenko, A. K. Geim, C. Casiraghi, A. H. Castro Neto, and K. S. Novoselov. *Strong Light-Matter Interactions in Heterostructures of Atomically Thin Films*. Science **340**, 1311–1314 (2013).

[7] A. K. Geim and I. V. Grigorieva. *Van der Waals heterostructures*. Nature **499**, 419–425 (2013).

[8] C. R. Dean, A. F. Young, I. Meric, C. Lee, L. Wang, S. Sorgenfrei, K. Watanabe, T. Taniguchi, P. Kim, K. L. Shepard, and J. Hone. *Boron nitride substrates for high-quality graphene electronics*. Nat. Nanotechnol. **5**, 722–726 (2010).

[9] A. Splendiani, L. Sun, Y. Zhang, T. Li, J. Kim, C.-Y. Chim, G. Galli, and F. Wang. *Emerging Photoluminescence in Monolayer MoS_2*. Nano Lett. **10**, 1271–1275 (2010).

[10] K. F. Mak, C. Lee, J. Hone, J. Shan, and T. F. Heinz. *Atomically Thin MoS_2: A New Direct-Gap Semiconductor*. Phys. Rev. Lett. **105**, 136805 (2010).

[11] K. S. Novoselov, A. K. Geim, S. V. Morozov, D. Jiang, Y. Zhang, S. V. Dubonos, I. V. Grigorieva, and A. A. Firsov. *Electric Field Effect in Atomically Thin Carbon Films*. Science **306**, 666–669 (2004).

[12] A. M. van der Zande, P. Y. Huang, D. A. Chenet, T. C. Berkelbach, Y. You, G.-H. Lee, T. F. Heinz, D. R. Reichman, D. A. Muller, and J. C. Hone. *Grains and grain boundaries in highly crystalline monolayer molybdenum disulphide*. Nat. Mater. **12**, 554–561 (2013).

[13] S. Najmaei, Z. Liu, W. Zhou, X. Zou, G. Shi, S. Lei, B. I. Yakobson, J.-C. Idrobo, P. M. Ajayan, and J. Lou. *Vapour phase growth and grain boundary structure of molybdenum disulphide atomic layers*. Nat. Mater. **12**, 754–759 (2013).

[14] Y. Zhang, T.-R. Chang, B. Zhou, Y.-T. Cui, H. Yan, Z. Liu, F. Schmitt, J. Lee, R. Moore, Y. Chen, H. Lin, H.-T. Jeng, S.-K. Mo, Z. Hussain, A. Bansil, et al. *Direct observation of the transition from indirect to direct bandgap in atomically thin epitaxial $MoSe_2$*. Nat. Nanotechnol. **9**, 111–115 (2014).

[15] K. He, N. Kumar, L. Zhao, Z. Wang, K. F. Mak, H. Zhao, and J. Shan. *Tightly Bound Excitons in Monolayer WSe_2*. Phys. Rev. Lett. **113**, 026803 (2014).

[16] A. Chernikov, T. C. Berkelbach, H. M. Hill, A. Rigosi, Y. Li, O. B. Aslan, D. R. Reichman, M. S. Hybertsen, and T. F. Heinz. *Exciton Binding Energy and Nonhydrogenic Rydberg Series in Monolayer WS_2*. Phys. Rev. Lett. **113**, 076802 (2014).

[17] Z. Ye, T. Cao, K. O'Brien, H. Zhu, X. Yin, Y. Wang, S. G. Louie, and X. Zhang. *Probing excitonic dark states in single-layer tungsten disulphide*. Nature **513**, 214–218 (2014).

[18] M. M. Ugeda, A. J. Bradley, S.-F. Shi, F. H. da Jornada, Y. Zhang, D. Y. Qiu, W. Ruan, S.-K. Mo, Z. Hussain, Z.-X. Shen, F. Wang, S. G. Louie, and M. F. Crommie. *Giant bandgap renormalization and excitonic effects in a monolayer transition metal dichalcogenide semiconductor*. Nat. Mater. **13**, 1091–1095 (2014).

[19] G. Wang, X. Marie, I. Gerber, T. Amand, D. Lagarde, L. Bouet, M. Vidal, A. Balocchi, and B. Urbaszek. *Giant Enhancement of the Optical Second-Harmonic Emission of WSe_2 Monolayers by Laser Excitation at Exciton Resonances*. Phys. Rev. Lett. **114**, 097403 (2015).

[20] K. F. Mak, K. He, C. Lee, G. H. Lee, J. Hone, T. F. Heinz, and J. Shan. *Tightly bound trions in monolayer MoS_2*. Nat. Mater. **12**, 207–211 (2013).

[21] J. S. Ross, S. Wu, H. Yu, N. J. Ghimire, A. M. Jones, G. Aivazian, J. Yan, D. G. Mandrus, D. Xiao, W. Yao, and X. Xu. *Electrical control of neutral and charged excitons in a monolayer semiconductor*. Nat. Commun. **4**, 1474 (2013).

[22] Y. You, X.-X. Zhang, T. C. Berkelbach, M. S. Hybertsen, D. R. Reichman, and T. F. Heinz. *Observation of biexcitons in monolayer WSe_2*. Nat. Phys. **11**, 477–481 (2015).

[23] E. J. Sie, A. J. Frenzel, Y.-H. Lee, J. Kong, and N. Gedik. *Intervalley biexcitons and many-body effects in monolayer MoS_2*. Phys. Rev. B **92**, 125417 (2015).

[24] M. Sidler, P. Back, O. Cotlet, A. Srivastava, T. Fink, M. Kroner, E. Demler, and A. Imamoglu. *Fermi polaron-polaritons in charge-tunable atomically thin semiconductors*. Nat. Phys. **13**, 255–261 (2017).

[25] X. Xu, W. Yao, D. Xiao, and T. F. Heinz. *Spin and pseudospins in layered transition metal dichalcogenides*. Nat. Phys. **10**, 343–350 (2014).

[26] J. R. Schaibley, H. Yu, G. Clark, P. Rivera, J. S. Ross, K. L. Seyler, W. Yao, and X. Xu. *Valleytronics in 2D materials*. Nat. Rev. Mater. **1**, 16055 (2016).

[27] K. F. Mak, K. L. McGill, J. Park, and P. L. McEuen. *The valley Hall effect in MoS_2 transistors*. Science **344**, 1489–1492 (2014).

[28] Y. J. Zhang, T. Oka, R. Suzuki, J. T. Ye, and Y. Iwasa. *Electrically Switchable Chiral Light-Emitting Transistor*. Science **344**, 725–728 (2014).

[29] W. Yang, J. Shang, J. Wang, X. Shen, B. Cao, N. Peimyoo, C. Zou, Y. Chen, Y. Wang, C. Cong, W. Huang, and T. Yu. *Electrically Tunable Valley-Light Emitting Diode (vLED) Based on CVD-Grown Monolayer WS_2*. Nano Lett. **16**, 1560–1567 (2016).

[30] S. W. Hell. *Far-Field Optical Nanoscopy*. Science **316**, 1153–1158 (2007).

[31] J. Berezovsky, O. Gywat, F. Meier, D. Battaglia, X. Peng, and D. D. Awschalom. *Initialization and read-out of spins in coupled core-shell quantum dots*. Nat. Phys. **2**, 831–834 (2006).

[32] J. Hwang, M. Pototschnig, R. Lettow, G. Zumofen, A. Renn, S. Götzinger, and V. Sandoghdar. *A single-molecule optical transistor*. Nature **460**, 76–80 (2009).

[33] I. Aharonovich, D. Englund, and M. Toth. *Solid-state single-photon emitters*. Nat. Photonics **10**, 631–641 (2016).

[34] C. Bradac, T. Gaebel, N. Naidoo, M. J. Sellars, J. Twamley, L. J. Brown, A. S. Barnard, T. Plakhotnik, A. V. Zvyagin, and J. R. Rabeau. *Observation and control of blinking nitrogen-vacancy centres in discrete nanodiamonds*. Nat. Nanotechnol. **5**, 345–349 (2010).

[35] N. Ai, W. Walden-Newman, Q. Song, S. Kalliakos, and S. Strauf. *Suppression of Blinking and Enhanced Exciton Emission from Individual Carbon Nanotubes*. ACS Nano **5**, 2664–2670 (2011).

[36] G. Kucsko, P. C. Maurer, N. Y. Yao, M. Kubo, H. J. Noh, P. K. Lo, H. Park, and M. D. Lukin. *Nanometre-scale thermometry in a living cell*. Nature **500**, 54–58 (2013).

[37] E. Rittweger, K. Y. Han, S. E. Irvine, C. Eggeling, and S. W. Hell. *STED microscopy reveals crystal colour centres with nanometric resolution*. Nat. Photonics **3**, 144–147 (2009).

[38] N. C. Seeman. *Nanomaterials Based on DNA*. Annu. Rev. Biochem. **79**, 65–87 (2010).

[39] A. P. Alivisatos. *Semiconductor Clusters, Nanocrystals, and Quantum Dots*. Science **271**, 933–937 (1996).

[40] Y. Yin and A. P. Alivisatos. *Colloidal nanocrystal synthesis and the organic-inorganic interface*. Nature **437**, 664–670 (2005).

[41] A. M. Smith and S. Nie. *Next-generation quantum dots*. Nat. Biotechnol. **27**, 732–733 (2009).

[42] E. H. Sargent. *Colloidal quantum dot solar cells*. Nat. Photonics **6**, 133–135 (2012).

[43] R. Osovsky, D. Cheskis, V. Kloper, A. Sashchiuk, M. Kroner, and E. Lifshitz. *Continuous-Wave Pumping of Multiexciton Bands in the Photoluminescence Spectrum of a Single CdTe-CdSe Core-Shell Colloidal Quantum Dot*. Phys. Rev. Lett. **102**, 197401 (2009).

[44] L. Biadala, Y. Louyer, P. Tamarat, and B. Lounis. *Direct Observation of the Two Lowest Exciton Zero-Phonon Lines in Single CdSe/ZnS Nanocrystals.* Phys. Rev. Lett. **103**, 037404 (2009).

[45] G. E. Cragg and A. L. Efros. *Suppression of Auger Processes in Confined Structures.* Nano Lett. **10**, 313–317 (2010).

[46] O. Chen, J. Zhao, V. P. Chauhan, J. Cui, C. Wong, D. K. Harris, H. Wei, H.-S. Han, D. Fukumura, R. K. Jain, and M. G. Bawendi. *Compact high-quality CdSe-CdS core-shell nanocrystals with narrow emission linewidths and suppressed blinking.* Nat. Mater. **12**, 445–451 (2013).

[47] A. A. Cordones and S. R. Leone. *Mechanisms for charge trapping in single semiconductor nanocrystals probed by fluorescence blinking.* Chem. Soc. Rev. **42**, 3209–3221 (2013).

[48] H. Htoon, A. V. Malko, D. Bussian, J. Vela, Y. Chen, J. A. Hollingsworth, and V. I. Klimov. *Highly Emissive Multiexcitons in Steady-State Photoluminescence of Individual "Giant" CdSe/CdS Core/Shell Nanocrystals.* Nano Lett. **10**, 2401–2407 (2010).

[49] C. Galland, Y. Ghosh, A. Steinbrück, M. Sykora, J. A. Hollingsworth, V. I. Klimov, and H. Htoon. *Two types of luminescence blinking revealed by spectroelectrochemistry of single quantum dots.* Nature **479**, 203–207 (2011).

[50] M. Nirmal, B. O. Dabbousi, M. G. Bawendi, J. J. Macklin, J. K. Trautman, T. D. Harris, and L. E. Brus. *Fluorescence intermittency in single cadmium selenide nanocrystals.* Nature **383**, 802–804 (1996).

[51] P. Frantsuzov, M. Kuno, B. Janko, and R. A. Marcus. *Universal emission intermittency in quantum dots, nanorods and nanowires.* Nat. Phys. **4**, 519–522 (2008).

[52] T. Basché, S. Kummer, and C. Bräuchle. *Direct spectroscopic observation of quantum jumps of a single molecule.* Nature **373**, 132–134 (1995).

[53] X. Wang, X. Ren, K. Kahen, M. A. Hahn, M. Rajeswaran, S. Maccagnano-Zacher, J. Silcox, G. E. Cragg, A. L. Efros, and T. D. Krauss. *Retraction: Non-blinking semiconductor nanocrystals.* Nature **527**, 544–544 (2015).

[54] F. T. Rabouw, N. M. B. Cogan, A. C. Berends, W. v. d. Stam, D. Vanmaekelbergh, A. F. Koenderink, T. D. Krauss, and C. d. M. Donega. *Non-blinking single-photon emitters in silica.* Sci. Rep. **6**, 21187 (2016).

[55] T. Basché, W. E. Moerner, M. Orrit, and U. P. Wild, eds. *Single-Molecule Optical Detection, Imaging and Spectroscopy* (VCH Verlagsgesellschaft mbH, 1997).

[56] I. Aharonovich, A. D. Greentree, and S. Prawer. *Diamond photonics.* Nat. Photonics **5**, 397–405 (2011).

[57] V. I. Klimov, S. A. Ivanov, J. Nanda, M. Achermann, I. Bezel, J. A. McGuire, and A. Piryatinski. *Single-exciton optical gain in semiconductor nanocrystals.* Nature **447**, 441–446 (2007).

[58] S. Ithurria, M. D. Tessier, B. Mahler, R. P. S. M. Lobo, B. Dubertret, and A. L. Efros. *Colloidal nanoplatelets with two-dimensional electronic structure.* Nat. Mater. **10**, 936–941 (2011).

[59] A. Srivastava, M. Sidler, A. V. Allain, D. S. Lembke, A. Kis, and A. Imamoğlu. *Optically active quantum dots in monolayer WSe_2*. Nat. Nanotechnol. **10**, 491–496 (2015).

[60] Y.-M. He, G. Clark, J. R. Schaibley, Y. He, M.-C. Chen, Y.-J. Wei, X. Ding, Q. Zhang, W. Yao, X. Xu, C.-Y. Lu, and J.-W. Pan. *Single quantum emitters in monolayer semiconductors*. Nat. Nanotechnol. **10**, 497–502 (2015).

[61] M. Koperski, K. Nogajewski, A. Arora, V. Cherkez, P. Mallet, J.-Y. Veuillen, J. Marcus, P. Kossacki, and M. Potemski. *Single photon emitters in exfoliated WSe_2 structures*. Nat. Nanotechnol. **10**, 503–506 (2015).

[62] C. Chakraborty, L. Kinnischtzke, K. M. Goodfellow, R. Beams, and A. N. Vamivakas. *Voltage-controlled quantum light from an atomically thin semiconductor*. Nat. Nanotechnol. **10**, 507–511 (2015).

[63] M. C. Weidman, M. Seitz, S. D. Stranks, and W. A. Tisdale. *Highly Tunable Colloidal Perovskite Nanoplatelets through Variable Cation, Metal, and Halide Composition*. ACS Nano **10**, 7830–7839 (2016).

[64] A. L. Efros, M. Rosen, M. Kuno, M. Nirmal, D. J. Norris, and M. Bawendi. *Band-edge exciton in quantum dots of semiconductors with a degenerate valence band: Dark and bright exciton states*. Phys. Rev. B **54**, 4843–4856 (1996).

[65] X. Zhang, X.-F. Qiao, W. Shi, J.-B. Wu, D.-S. Jiang, and P.-H. Tan. *Phonon and Raman scattering of two-dimensional transition metal dichalcogenides from monolayer, multilayer to bulk material*. Chem. Soc. Rev. **44**, 2757–2785 (2015).

[66] M. D. Mason, G. M. Credo, K. D. Weston, and S. K. Buratto. *Luminescence of Individual Porous Si Chromophores*. Phys. Rev. Lett. **80**, 5405–5408 (1998).

[67] D. S. English, L. E. Pell, Z. Yu, P. F. Barbara, and B. A. Korgel. *Size Tunable Visible Luminescence from Individual Organic Monolayer Stabilized Silicon Nanocrystal Quantum Dots*. Nano Lett. **2**, 681–685 (2002).

[68] J. Martin, F. Cichos, F. Huisken, and C. von Borczyskowski. *Electron–Phonon Coupling and Localization of Excitons in Single Silicon Nanocrystals*. Nano Lett. **8**, 656–660 (2008).

[69] A. M. Chizhik, A. I. Chizhik, R. Gutbrod, A. J. Meixner, T. Schmidt, J. Sommerfeld, and F. Huisken. *Imaging and Spectroscopy of Defect Luminescence and Electron-Phonon Coupling in Single SiO_2 Nanoparticles*. Nano Lett. **9**, 3239–3244 (2009).

[70] X. Wang, X. Ren, K. Kahen, M. A. Hahn, M. Rajeswaran, S. Maccagnano-Zacher, J. Silcox, G. E. Cragg, A. L. Efros, and T. D. Krauss. *Non-blinking semiconductor nanocrystals*. Nature **459**, 686–689 (2009).

[71] K. Kůsová, O. Cibulka, K. Dohnalová, I. Pelant, J. Valenta, A. Fučíková, K. Žídek, J. Lang, J. Englich, P. Matějka, P. Štěpánek, and S. Bakardjieva. *Brightly Luminescent Organically Capped Silicon Nanocrystals Fabricated at Room Temperature and Atmospheric Pressure*. ACS Nano **4**, 4495–4504 (2010).

[72] T. Schmidt, A. I. Chizhik, A. M. Chizhik, K. Potrick, A. J. Meixner, and F. Huisken. *Radiative exciton recombination and defect luminescence observed in single silicon nanocrystals*. Phys. Rev. B **86**, 125302 (2012).

[73] J. K. Trautman, J. J. Macklin, L. E. Brus, and E. Betzig. *Near-field spectroscopy of single molecules at room temperature*. Nature **369**, 40–42 (1994).

[74] J. J. Macklin, J. K. Trautman, T. D. Harris, and L. E. Brus. *Imaging and Time-Resolved Spectroscopy of Single Molecules at an Interface*. Science **272**, 255–258 (1996).

[75] M. Orrit and T. Basché. *Steady Light from Quantum Dots, at Last. But How?* Chem. Phys. Chem. **10**, 2383–2385 (2009).

[76] K. Puschkarsky. *Realization and applications of a tunable high-transmission optical etalon*. Master's thesis, Ludwig-Maximilians-Universität München (2014).

[77] R. Kettner, J. Tittel, T. Basché, and C. Bräuchle. *Optical Spectroscopy and Spectral Diffusion of Single Dye Molecules in Amorphous Spin-Coated Polymer Films*. J. Phys. Chem. **98**, 6671–6674 (1994).

[78] B. Kozankiewicz, J. Bernard, and M. Orrit. *Single molecule lines and spectral hole burning of terrylene in different matrices*. J. Chem. Phys. **101**, 9377–9383 (1994).

[79] A. Walser, A. Renn, S. Götzinger, and V. Sandoghdar. *Lifetime-limited zero-phonon spectra of single molecules in methyl methacrylate*. Chem. Phys. Lett. **472**, 44–47 (2009).

[80] F. P. Diehl, C. Roos, H.-C. Jankowiak, R. Berger, A. Köhn, G. Diezemann, and T. Basché. *Combined Experimental and Theoretical Study of the Vibronic Spectra of Perylenecarboximides*. J. Phys. Chem. B **114**, 1638–1647 (2010).

[81] P. Tchénio, A. B. Myers, and W. Moerner. *Vibrational analysis of the dispersed fluorescence from single molecules of terrylene in polyethylene*. Chem. Phys. Lett. **213**, 325–332 (1993).

[82] A. B. Myers, P. Tchénio, M. Z. Zgierski, and W. E. Moerner. *Vibronic Spectroscopy of Individual Molecules in Solids*. J. Phys. Chem. **98**, 10377–10390 (1994).

[83] A. Walser, G. Zumofen, A. Renn, S. Götzinger, and V. Sandoghdar. *Spectral dynamics and spatial localization of single molecules in a polymer*. Mol. Phys. **107**, 1897–1909 (2009).

[84] P. Tchénio, A. B. Myers, and W. E. Moerner. *Dispersed fluorescence spectra of single molecules of pentacene in p-terphenyl*. J. Phys. Chem. **97**, 2491–2493 (1993).

[85] A. P. Green and A. R. Buckley. *Solid state concentration quenching of organic fluorophores in PMMA*. Phys. Chem. Chem. Phys. **17**, 1435–1440 (2015).

[86] T. Basché, W. E. Moerner, M. Orrit, and H. Talon. *Photon antibunching in the fluorescence of a single dye molecule trapped in a solid*. Phys. Rev. Lett. **69**, 1516–1519 (1992).

[87] B. Lounis and W. E. Moerner. *Single photons on demand from a single molecule at room temperature*. Nature **407**, 491–493 (2000).

[88] W. E. Moerner and L. Kador. *Optical detection and spectroscopy of single molecules in a solid*. Phys. Rev. Lett. **62**, 2535–2538 (1989).

[89] W. Helfrich and F. R. Lipsett. *Fluorescence and Defect Fluorescence of Anthracene at 4.2°K*. J. Chem. Phys. **43**, 4368–4376 (1965).

[90] F. Jelezko and J. Wrachtrup. *Single defect centres in diamond: A review*. Phys. Status Solidi A **203**, 3207–3225 (2006).

[91] T.-L. Wee, Y.-K. Tzeng, C.-C. Han, H.-C. Chang, W. Fann, J.-H. Hsu, K.-M. Chen, and Y.-C. Yu. *Two-photon Excited Fluorescence of Nitrogen-Vacancy Centers in Proton-Irradiated Type Ib Diamond*. J. Phys. Chem. A **111**, 9379–9386 (2007).

[92] I. B. Berlman. *Handbook of Fluorescence Spectra of Aromatic Molecules*. 2nd ed. (Academic Press, 1971).

[93] Q. H. Wang, K. Kalantar-Zadeh, A. Kis, J. N. Coleman, and M. S. Strano. *Electronics and optoelectronics of two-dimensional transition metal dichalcogenides*. Nat. Nanotechnol. **7**, 699–712 (2012).

[94] G.-B. Liu, D. Xiao, Y. Yao, X. Xu, and W. Yao. *Electronic structures and theoretical modelling of two-dimensional group-VIB transition metal dichalcogenides*. Chem. Soc. Rev. **44**, 2643–2663 (2015).

[95] K. F. Mak and J. Shan. *Photonics and optoelectronics of 2D semiconductor transition metal dichalcogenides*. Nat. Photonics **10**, 216–226 (2016).

[96] Y. Liu, N. O. Weiss, X. Duan, H.-C. Cheng, Y. Huang, and X. Duan. *Van der Waals heterostructures and devices*. Nat. Rev. Mater. **1**, 16042 (2016).

[97] M. Chhowalla, H. S. Shin, G. Eda, L.-J. Li, K. P. Loh, and H. Zhang. *The chemistry of two-dimensional layered transition metal dichalcogenide nanosheets*. Nat. Chem. **5**, 263–275 (2013).

[98] X. Qian, J. Liu, L. Fu, and J. Li. *Quantum spin Hall effect in two-dimensional transition metal dichalcogenides*. Science **346**, 1344–1347 (2014).

[99] Z. Fei, T. Palomaki, S. Wu, W. Zhao, X. Cai, B. Sun, P. Nguyen, J. Finney, X. Xu, and D. H. Cobden. *Edge conduction in monolayer WTe_2*. Nat. Phys. **13**, 677–682 (2017).

[100] S. Tang, C. Zhang, D. Wong, Z. Pedramrazi, H.-Z. Tsai, C. Jia, B. Moritz, M. Claassen, H. Ryu, S. Kahn, J. Jiang, H. Yan, M. Hashimoto, D. Lu, R. G. Moore, et al. *Quantum spin Hall state in monolayer 1T'-WTe_2*. Nat. Phys. **13**, 683–687 (2017).

[101] L. F. Mattheiss. *Band Structures of Transition-Metal-Dichalcogenide Layer Compounds*. Phys. Rev. B **8**, 3719–3740 (1973).

[102] T. Li and G. Galli. *Electronic Properties of MoS_2 Nanoparticles*. J. Phys. Chem. C **111**, 16192–16196 (2007).

[103] S. Tongay, J. Zhou, C. Ataca, K. Lo, T. S. Matthews, J. Li, J. C. Grossman, and J. Wu. *Thermally Driven Crossover from Indirect toward Direct Bandgap in 2D Semiconductors: $MoSe_2$ versus MoS_2*. Nano Lett. **12**, 5576–5580 (2012).

[104] W. Zhao, Z. Ghorannevis, L. Chu, M. Toh, C. Kloc, P.-H. Tan, and G. Eda. *Evolution of Electronic Structure in Atomically Thin Sheets of WS_2 and WSe_2*. ACS Nano **7**, 791–797 (2013).

[105] C. Ruppert, O. B. Aslan, and T. F. Heinz. *Optical Properties and Band Gap of Single- and Few-Layer $MoTe_2$ Crystals*. Nano Lett. **14**, 6231–6236 (2014).

[106] G.-B. Liu, W.-Y. Shan, Y. Yao, W. Yao, and D. Xiao. *Three-band tight-binding model for monolayers of group-VIB transition metal dichalcogenides*. Phys. Rev. B **88**, 085433 (2013).

[107] K. Kośmider, J. W. González, and J. Fernández-Rossier. *Large spin splitting in the conduction band of transition metal dichalcogenide monolayers*. Phys. Rev. B **88**, 245436 (2013).

[108] S. LaShell, B. A. McDougall, and E. Jensen. *Spin Splitting of an Au(111) Surface State Band Observed with Angle Resolved Photoelectron Spectroscopy*. Phys. Rev. Lett. **77**, 3419–3422 (1996).

[109] D. Xiao, G.-B. Liu, W. Feng, X. Xu, and W. Yao. *Coupled Spin and Valley Physics in Monolayers of MoS_2 and Other Group-VI Dichalcogenides*. Phys. Rev. Lett. **108**, 196802 (2012).

[110] A. Ramasubramaniam. *Large excitonic effects in monolayers of molybdenum and tungsten dichalcogenides*. Phys. Rev. B **86**, 115409 (2012).

[111] I. N. Levine. *Quantum Chemistry*. 7th ed. (Pearson, 2013).

[112] Z. Zhu, Y. Cheng, and U. Schwingenschlögl. *Giant spin-orbit-induced spin splitting in two-dimensional transition-metal dichalcogenide semiconductors*. Phys. Rev. B **84**, 153402 (2011).

[113] H. Ochoa and R. Roldán. *Spin-orbit-mediated spin relaxation in monolayer MoS_2*. Phys. Rev. B **87**, 245421 (2013).

[114] A. Kormányos, V. Zólyomi, N. D. Drummond, P. Rakyta, G. Burkard, and V. I. Fal'ko. *Monolayer MoS_2: Trigonal warping, the Γ valley, and spin-orbit coupling effects*. Phys. Rev. B **88**, 045416 (2013).

[115] G. Wang, C. Robert, A. Suslu, B. Chen, S. Yang, S. Alamdari, I. C. Gerber, T. Amand, X. Marie, S. Tongay, and B. Urbaszek. *Spin-orbit engineering in transition metal dichalcogenide alloy monolayers*. Nat. Commun. **6**, 10110 (2015).

[116] R. J. Elliott. *Theory of the Effect of Spin-Orbit Coupling on Magnetic Resonance in Some Semiconductors*. Phys. Rev. **96**, 266–279 (1954).

[117] J. M. Luttinger and W. Kohn. *Motion of Electrons and Holes in Perturbed Periodic Fields*. Phys. Rev. **97**, 869–883 (1955).

[118] R. Winkler. *Spin-Orbit Coupling Effects in Two-Dimensional Electron and Hole Systems* (Springer, 2003).

[119] G.-B. Liu, H. Pang, Y. Yao, and W. Yao. *Intervalley coupling by quantum dot confinement potentials in monolayer transition metal dichalcogenides*. New J. Phys. **16**, 105011 (2014).

[120] A. Kormányos, G. Burkard, M. Gmitra, J. Fabian, V. Zólyomi, N. D. Drummond, and V. Fal'ko. *$k\cdot p$ theory for two-dimensional transition metal dichalcogenide semiconductors*. 2D Mater. **2**, 022001 (2015).

[121] H. Rostami, A. G. Moghaddam, and R. Asgari. *Effective lattice Hamiltonian for monolayer MoS_2: Tailoring electronic structure with perpendicular electric and magnetic fields*. Phys. Rev. B **88**, 085440 (2013).

[122] F. Rose, M. O. Goerbig, and F. Piéchon. *Spin- and valley-dependent magneto-optical properties of MoS_2*. Phys. Rev. B **88**, 125438 (2013).

[123] A. Kormányos, V. Zólyomi, N. D. Drummond, and G. Burkard. *Spin-Orbit Coupling, Quantum Dots, and Qubits in Monolayer Transition Metal Dichalcogenides*. Phys. Rev. X **4**, 011034 (2014).

[124] Z. Li and J. P. Carbotte. *Longitudinal and spin-valley Hall optical conductivity in single layer MoS_2*. Phys. Rev. B **86**, 205425 (2012).

[125] H.-Z. Lu, W. Yao, D. Xiao, and S.-Q. Shen. *Intervalley Scattering and Localization Behaviors of Spin-Valley Coupled Dirac Fermions*. Phys. Rev. Lett. **110**, 016806 (2013).

[126] W.-Y. Shan, H.-Z. Lu, and D. Xiao. *Spin Hall effect in spin-valley coupled monolayers of transition metal dichalcogenides*. Phys. Rev. B **88**, 125301 (2013).

[127] T. Cai, S. A. Yang, X. Li, F. Zhang, J. Shi, W. Yao, and Q. Niu. *Magnetic control of the valley degree of freedom of massive Dirac fermions with application to transition metal dichalcogenides*. Phys. Rev. B **88**, 115140 (2013).

[128] W. Yao, D. Xiao, and Q. Niu. *Valley-dependent optoelectronics from inversion symmetry breaking*. Phys. Rev. B **77**, 235406 (2008).

[129] J. O. Dimmock. In *Semiconductors and Semimetals*. Vol. 3, pp. 259–319. Edited by R. K. Willardson and A. C. Beer (Academic Press, 1967).

[130] J. J. Sakurai and J. Napolitano. *Modern Quantum Mechanics*. 2nd ed. (Pearson, 2010).

[131] T. Cao, G. Wang, W. Han, H. Ye, C. Zhu, J. Shi, Q. Niu, P. Tan, E. Wang, B. Liu, and J. Feng. *Valley-selective circular dichroism of monolayer molybdenum disulphide*. Nat. Commun. **3**, 887 (2012).

[132] K. F. Mak, K. He, J. Shan, and T. F. Heinz. *Control of valley polarization in monolayer MoS_2 by optical helicity*. Nat. Nanotechnol. **7**, 494–498 (2012).

[133] H. Zeng, J. Dai, W. Yao, D. Xiao, and X. Cui. *Valley polarization in MoS_2 monolayers by optical pumping*. Nat. Nanotechnol. **7**, 490–493 (2012).

[134] A. M. Jones, H. Yu, N. J. Ghimire, S. Wu, G. Aivazian, J. S. Ross, B. Zhao, J. Yan, D. G. Mandrus, D. Xiao, W. Yao, and X. Xu. *Optical generation of excitonic valley coherence in monolayer WSe_2*. Nat. Nanotechnol. **8**, 634–638 (2013).

[135] G. Wang, C. Robert, M. M. Glazov, F. Cadiz, E. Courtade, T. Amand, D. Lagarde, T. Taniguchi, K. Watanabe, B. Urbaszek, and X. Marie. *In-Plane Propagation of Light in Transition Metal Dichalcogenide Monolayers: Optical Selection Rules*. Phys. Rev. Lett. **119**, 047401 (2017).

[136] J. P. Echeverry, B. Urbaszek, T. Amand, X. Marie, and I. C. Gerber. *Splitting between bright and dark excitons in transition metal dichalcogenide monolayers*. Phys. Rev. B **93**, 121107 (2016).

[137] M. V. Berry. *Quantal Phase Factors Accompanying Adiabatic Changes*. Proc. R. Soc. London, Ser. A **392**, 45–57 (1984).

[138] D. Xiao, M.-C. Chang, and Q. Niu. *Berry phase effects on electronic properties*. Rev. Mod. Phys. **82**, 1959–2007 (2010).

[139] M.-C. Chang and Q. Niu. *Berry phase, hyperorbits, and the Hofstadter spectrum: Semiclassical dynamics in magnetic Bloch bands*. Phys. Rev. B **53**, 7010–7023 (1996).

[140] D. Xiao, W. Yao, and Q. Niu. *Valley-Contrasting Physics in Graphene: Magnetic Moment and Topological Transport*. Phys. Rev. Lett. **99**, 236809 (2007).

[141] Y. Yafet. In *Solid State Physics*. Vol. 14, pp. 1–98. Edited by F. Seitz and D. Turnbull (Academic Press, 1963).

[142] Y. Li, J. Ludwig, T. Low, A. Chernikov, X. Cui, G. Arefe, Y. D. Kim, A. M. van der Zande, A. Rigosi, H. M. Hill, S. H. Kim, J. Hone, Z. Li, D. Smirnov, and T. F. Heinz. *Valley Splitting and Polarization by the Zeeman Effect in Monolayer $MoSe_2$*. Phys. Rev. Lett. **113**, 266804 (2014).

[143] D. MacNeill, C. Heikes, K. F. Mak, Z. Anderson, A. Kormányos, V. Zólyomi, J. Park, and D. C. Ralph. *Breaking of Valley Degeneracy by Magnetic Field in Monolayer $MoSe_2$*. Phys. Rev. Lett. **114**, 037401 (2015).

[144] G. Aivazian, Z. Gong, A. M. Jones, R.-L. Chu, J. Yan, D. G. Mandrus, C. Zhang, D. Cobden, W. Yao, and X. Xu. *Magnetic control of valley pseudospin in monolayer WSe_2*. Nat. Phys. **11**, 148–152 (2015).

[145] A. Srivastava, M. Sidler, A. V. Allain, D. S. Lembke, A. Kis, and A. Imamoğlu. *Valley Zeeman effect in elementary optical excitations of monolayer WSe_2*. Nat. Phys. **11**, 141–147 (2015).

[146] A. V. Stier, K. M. McCreary, B. T. Jonker, J. Kono, and S. A. Crooker. *Exciton diamagnetic shifts and valley Zeeman effects in monolayer WS_2 and MoS_2 to 65 Tesla*. Nat. Commun. **7**, 10643 (2016).

[147] A. Arora, R. Schmidt, R. Schneider, M. R. Molas, I. Breslavetz, M. Potemski, and R. Bratschitsch. *Valley Zeeman Splitting and Valley Polarization of Neutral and Charged Excitons in Monolayer $MoTe_2$ at High Magnetic Fields*. Nano Lett. **16**, 3624–3629 (2016).

[148] G. Wang, L. Bouet, M. M. Glazov, T. Amand, E. L. Ivchenko, E. Palleau, X. Marie, and B. Urbaszek. *Magneto-optics in transition metal diselenide monolayers*. 2D Mater. **2**, 034002 (2015).

[149] D. V. Rybkovskiy, I. C. Gerber, and M. V. Durnev. *Atomically inspired $k\cdot p$ approach and valley Zeeman effect in transition metal dichalcogenide monolayers*. Phys. Rev. B **95**, 155406 (2017).

[150] H. Rostami and R. Asgari. *Valley Zeeman effect and spin-valley polarized conductance in monolayer MoS_2 in a perpendicular magnetic field*. Phys. Rev. B **91**, 075433 (2015).

[151] H. Yu, X. Cui, X. Xu, and W. Yao. *Valley excitons in two-dimensional semiconductors*. Natl. Sci. Rev. **2**, 57–70 (2015).

[152] M. M. Glazov, E. L. Ivchenko, G. Wang, T. Amand, X. Marie, B. Urbaszek, and B. L. Liu. *Spin and valley dynamics of excitons in transition metal dichalcogenide monolayers*. Phys. Status Solidi B **252**, 2349–2362 (2015).

[153] D. Y. Qiu, F. H. da Jornada, and S. G. Louie. *Screening and many-body effects in two-dimensional crystals: Monolayer MoS_2*. Phys. Rev. B **93**, 235435 (2016).

[154] X. L. Yang, S. H. Guo, F. T. Chan, K. W. Wong, and W. Y. Ching. *Analytic solution of a two-dimensional hydrogen atom. I. Nonrelativistic theory*. Phys. Rev. A **43**, 1186–1196 (1991).

[155] D. Y. Qiu, F. H. da Jornada, and S. G. Louie. *Optical Spectrum of MoS_2: Many-Body Effects and Diversity of Exciton States*. Phys. Rev. Lett. **111**, 216805 (2013).

[156] O. Gunawan, E. P. De Poortere, and M. Shayegan. *AlAs two-dimensional electrons in an antidot lattice: Electron pinball with elliptical Fermi contours*. Phys. Rev. B **75**, 081304 (2007).

[157] D. Culcer, A. L. Saraiva, B. Koiller, X. Hu, and S. Das Sarma. *Valley-Based Noise-Resistant Quantum Computation Using Si Quantum Dots*. Phys. Rev. Lett. **108**, 126804 (2012).

[158] A. Rycerz, J. Tworzydło, and C. W. J. Beenakker. *Valley filter and valley valve in graphene*. Nat. Phys. **3**, 172–175 (2007).

[159] J. Kim, X. Hong, C. Jin, S.-F. Shi, C.-Y. S. Chang, M.-H. Chiu, L.-J. Li, and F. Wang. *Ultrafast generation of pseudo-magnetic field for valley excitons in WSe_2 monolayers*. Science **346**, 1205–1208 (2014).

[160] G. Sallen, L. Bouet, X. Marie, G. Wang, C. R. Zhu, W. P. Han, Y. Lu, P. H. Tan, T. Amand, B. L. Liu, and B. Urbaszek. *Robust optical emission polarization in MoS_2 monolayers through selective valley excitation*. Phys. Rev. B **86**, 081301 (2012).

[161] D. Lagarde, L. Bouet, X. Marie, C. R. Zhu, B. L. Liu, T. Amand, P. H. Tan, and B. Urbaszek. *Carrier and Polarization Dynamics in Monolayer MoS_2*. Phys. Rev. Lett. **112**, 047401 (2014).

[162] G. Wang, L. Bouet, D. Lagarde, M. Vidal, A. Balocchi, T. Amand, X. Marie, and B. Urbaszek. *Valley dynamics probed through charged and neutral exciton emission in monolayer WSe_2*. Phys. Rev. B **90**, 075413 (2014).

[163] S. Wu, J. S. Ross, G.-B. Liu, G. Aivazian, A. Jones, Z. Fei, W. Zhu, D. Xiao, W. Yao, D. Cobden, and X. Xu. *Electrical tuning of valley magnetic moment through symmetry control in bilayer MoS_2*. Nat. Phys. **9**, 149–153 (2013).

[164] A. M. Jones, H. Yu, J. S. Ross, P. Klement, N. J. Ghimire, J. Yan, D. G. Mandrus, W. Yao, and X. Xu. *Spin-layer locking effects in optical orientation of exciton spin in bilayer WSe_2*. Nat. Phys. **10**, 130–134 (2014).

[165] B. Zhu, H. Zeng, J. Dai, Z. Gong, and X. Cui. *Anomalously robust valley polarization and valley coherence in bilayer WS_2*. Proc. Natl. Acad. Sci. USA **111**, 11606–11611 (2014).

[166] F. Meier and B. P. Zakharchenya, eds. *Optical Orientation* (Elsevier Science Publishers B.V., 1984).

[167] M. Z. Maialle, E. A. de Andrada e Silva, and L. J. Sham. *Exciton spin dynamics in quantum wells*. Phys. Rev. B **47**, 15776–15788 (1993).

[168] M. M. Glazov, T. Amand, X. Marie, D. Lagarde, L. Bouet, and B. Urbaszek. *Exciton fine structure and spin decoherence in monolayers of transition metal dichalcogenides*. Phys. Rev. B **89**, 201302 (2014).

[169] T. Yu and M. W. Wu. *Valley depolarization due to intervalley and intravalley electron-hole exchange interactions in monolayer MoS_2*. Phys. Rev. B **89**, 205303 (2014).

[170] S. Tongay, J. Suh, C. Ataca, W. Fan, A. Luce, J. S. Kang, J. Liu, C. Ko, R. Raghunathanan, J. Zhou, F. Ogletree, J. Li, J. C. Grossman, and J. Wu. *Defects activated photoluminescence in two-dimensional semiconductors: interplay between bound, charged, and free excitons*. Sci. Rep. **3**, 2657 (2013).

[171] N. Scheuschner, O. Ochedowski, A.-M. Kaulitz, R. Gillen, M. Schleberger, and J. Maultzsch. *Photoluminescence of freestanding single- and few-layer MoS_2*. Phys. Rev. B **89**, 125406 (2014).

[172] T. C. Berkelbach, M. S. Hybertsen, and D. R. Reichman. *Theory of neutral and charged excitons in monolayer transition metal dichalcogenides*. Phys. Rev. B **88**, 045318 (2013).

[173] K. Gołasa, M. Grzeszczyk, P. Leszczyński, C. Faugeras, A. A. L. Nicolet, A. Wysmołek, M. Potemski, and A. Babiński. *Multiphonon resonant Raman scattering in MoS_2*. Appl. Phys. Lett. **104**, 092106 (2014).

[174] M. Staiger, R. Gillen, N. Scheuschner, O. Ochedowski, F. Kampmann, M. Schleberger, C. Thomsen, and J. Maultzsch. *Splitting of monolayer out-of-plane A_1' Raman mode in few-layer WS_2*. Phys. Rev. B **91**, 195419 (2015).

[175] Z. Gong, G.-B. Liu, H. Yu, D. Xiao, X. Cui, X. Xu, and W. Yao. *Magnetoelectric effects and valley-controlled spin quantum gates in transition metal dichalcogenide bilayers*. Nat. Commun. **4**, 2053 (2013).

[176] F. Cadiz, S. Tricard, M. Gay, D. Lagarde, G. Wang, C. Robert, P. Renucci, B. Urbaszek, and X. Marie. *Well separated trion and neutral excitons on superacid treated MoS_2 monolayers*. Appl. Phys. Lett. **108**, 251106 (2016).

[177] T. Karzig, C.-E. Bardyn, N. H. Lindner, and G. Refael. *Topological Polaritons*. Phys. Rev. X **5**, 031001 (2015).

[178] A. E. Almand-Hunter, H. Li, S. T. Cundiff, M. Mootz, M. Kira, and S. W. Koch. *Quantum droplets of electrons and holes*. Nature **506**, 471–475 (2014).

[179] M. T. Portella-Oberli, J. Berney, L. Kappei, F. Morier-Genoud, J. Szczytko, and B. Deveaud-Plédran. *Dynamics of Trion Formation in $In_xGa_{1-x}As$ Quantum Wells*. Phys. Rev. Lett. **102**, 096402 (2009).

[180] M. Nutz. *Optoelectronic Studies of Molybdenum Disulfide Field-Effect Devices*. Master's thesis, Ludwig-Maximilians-Universität München (2014).

[181] B. Radisavljevic, A. Radenovic, J. Brivio, V. Giacometti, and A. Kis. *Single-layer MoS_2 transistors*. Nat. Nanotechnol. **6**, 147–150 (2011).

[182] M. Buscema, M. Barkelid, V. Zwiller, H. S. J. van der Zant, G. A. Steele, and A. Castellanos-Gomez. *Large and Tunable Photothermoelectric Effect in Single-Layer MoS_2*. Nano Lett. **13**, 358–363 (2013).

[183] C.-H. Lee, G.-H. Lee, A. M. van der Zande, W. Chen, Y. Li, M. Han, X. Cui, G. Arefe, C. Nuckolls, T. F. Heinz, J. Guo, J. Hone, and P. Kim. *Atomically thin p-n junctions with van der Waals heterointerfaces*. Nat. Nanotechnol. **9**, 676–681 (2014).

[184] K. Dolui, I. Rungger, and S. Sanvito. *Origin of the n-type and p-type conductivity of MoS_2 monolayers on a SiO_2 substrate*. Phys. Rev. B **87**, 165402 (2013).

[185] S. Mouri, Y. Miyauchi, and K. Matsuda. *Tunable Photoluminescence of Monolayer MoS_2 via Chemical Doping*. Nano Lett. **13**, 5944–5948 (2013).

[186] A. Chernikov, A. M. van der Zande, H. M. Hill, A. F. Rigosi, A. Velauthapillai, J. Hone, and T. F. Heinz. *Electrical Tuning of Exciton Binding Energies in Monolayer WS_2*. Phys. Rev. Lett. **115**, 126802 (2015).

[187] K. He, C. Poole, K. F. Mak, and J. Shan. *Experimental Demonstration of Continuous Electronic Structure Tuning via Strain in Atomically Thin MoS_2*. Nano Lett. **13**, 2931–2936 (2013).

[188] H. J. Conley, B. Wang, J. I. Ziegler, R. F. Haglund, S. T. Pantelides, and K. I. Bolotin. *Bandgap Engineering of Strained Monolayer and Bilayer MoS_2*. Nano Lett. **13**, 3626–3630 (2013).

[189] C. R. Zhu, G. Wang, B. L. Liu, X. Marie, X. F. Qiao, X. Zhang, X. X. Wu, H. Fan, P. H. Tan, T. Amand, and B. Urbaszek. *Strain tuning of optical emission energy and polarization in monolayer and bilayer MoS_2*. Phys. Rev. B **88**, 121301 (2013).

[190] C. Rice, R. J. Young, R. Zan, U. Bangert, D. Wolverson, T. Georgiou, R. Jalil, and K. S. Novoselov. *Raman-scattering measurements and first-principles calculations of strain-induced phonon shifts in monolayer MoS_2*. Phys. Rev. B **87**, 081307 (2013).

[191] B. Chakraborty, A. Bera, D. V. S. Muthu, S. Bhowmick, U. V. Waghmare, and A. K. Sood. *Symmetry-dependent phonon renormalization in monolayer MoS_2 transistor*. Phys. Rev. B **85**, 161403 (2012).

[192] M. Palummo, M. Bernardi, and J. C. Grossman. *Exciton Radiative Lifetimes in Two-Dimensional Transition Metal Dichalcogenides*. Nano Lett. **15**, 2794–2800 (2015).

[193] C. H. Lui, A. J. Frenzel, D. V. Pilon, Y.-H. Lee, X. Ling, G. M. Akselrod, J. Kong, and N. Gedik. *Trion-Induced Negative Photoconductivity in Monolayer MoS_2*. Phys. Rev. Lett. **113**, 166801 (2014).

[194] A. Singh, G. Moody, K. Tran, M. E. Scott, V. Overbeck, G. Berghäuser, J. Schaibley, E. J. Seifert, D. Pleskot, N. M. Gabor, J. Yan, D. G. Mandrus, M. Richter, E. Malic, X. Xu, et al. *Trion formation dynamics in monolayer transition metal dichalcogenides*. Phys. Rev. B **93**, 041401 (2016).

[195] C. Würth, M. Grabolle, J. Pauli, M. Spieles, and U. Resch-Genger. *Relative and absolute determination of fluorescence quantum yields of transparent samples*. Nat. Protoc. **8**, 1535–1550 (2013).

[196] S. A. Wolf, D. D. Awschalom, R. A. Buhrman, J. M. Daughton, S. von Molnár, M. L. Roukes, A. Y. Chtchelkanova, and D. M. Treger. *Spintronics: A Spin-Based Electronics Vision for the Future*. Science **294**, 1488–1495 (2001).

[197] K. Kang, S. Xie, L. Huang, Y. Han, P. Y. Huang, K. F. Mak, C.-J. Kim, D. Muller, and J. Park. *High-mobility three-atom-thick semiconducting films with wafer-scale homogeneity*. Nature **520**, 656–660 (2015).

[198] F. Cadiz, E. Courtade, C. Robert, G. Wang, Y. Shen, H. Cai, T. Taniguchi, K. Watanabe, H. Carrere, D. Lagarde, M. Manca, T. Amand, P. Renucci, S. Tongay, X. Marie, et al. *Excitonic Linewidth Approaching the Homogeneous Limit in MoS_2-Based van der Waals Heterostructures*. Phys. Rev. X **7**, 021026 (2017).

[199] M. Amani, D.-H. Lien, D. Kiriya, J. Xiao, A. Azcatl, J. Noh, S. R. Madhvapathy, R. Addou, S. KC, M. Dubey, K. Cho, R. M. Wallace, S.-C. Lee, J.-H. He, J. W. Ager, et al. *Near-unity photoluminescence quantum yield in MoS_2*. Science **350**, 1065–1068 (2015).

[200] H. Yu, G.-B. Liu, P. Gong, X. Xu, and W. Yao. *Dirac cones and Dirac saddle points of bright excitons in monolayer transition metal dichalcogenides*. Nat. Commun. **5**, 3876 (2014).

[201] D. Y. Qiu, T. Cao, and S. G. Louie. *Nonanalyticity, Valley Quantum Phases, and Lightlike Exciton Dispersion in Monolayer Transition Metal Dichalcogenides: Theory and First-Principles Calculations*. Phys. Rev. Lett. **115**, 176801 (2015).

[202] A. O. Slobodeniuk and D. M. Basko. *Spin-flip processes and radiative decay of dark intravalley excitons in transition metal dichalcogenide monolayers*. 2D Mater. **3**, 035009 (2016).

[203] P. Rivera, K. L. Seyler, H. Yu, J. R. Schaibley, J. Yan, D. G. Mandrus, W. Yao, and X. Xu. *Valley-polarized exciton dynamics in a 2D semiconductor heterostructure*. Science **351**, 688–691 (2016).

[204] C. Jiang, W. Xu, A. Rasmita, Z. Huang, K. Li, Q. Xiong, and W.-b. Gao. *Microsecond dark-exciton valley polarization memory in 2D heterostructures*. ArXiv e-prints (2017). arXiv:1703.03133.

[205] A. Reina, H. Son, L. Jiao, B. Fan, M. S. Dresselhaus, Z. Liu, and J. Kong. *Transferring and Identification of Single- and Few-Layer Graphene on Arbitrary Substrates*. J. Phys. Chem. C **112**, 17741–17744 (2008).

Acknowledgments

First and foremost, I would like to thank my supervisor Alexander Högele for guiding me through my dissertation and entrusting me with numerous exciting projects. I deeply appreciate your advice and support, the time you have invested in our discussions, as well as the freedom you gave me to pursue and implement my ideas in the lab. Your honest approach to scientific research with a dash of optimism was always inspiring and kept me motivated especially at tough times. I am also grateful to you for keeping me funded throughout the years and for providing me with opportunities to attend various international conferences.

I am thankful to Jörg Kotthaus for establishing the friendly and productive working environment in the nanophysics group, and for sharing his wealth of scientific knowledge. Furthermore, I would like to thank Thomas Weitz for kindly accepting to review this thesis.

The success of this thesis relied heavily on scientific collaborations. Therefore, I am especially grateful to Hisato Yamaguchi for synthesizing invaluable samples of atomically thin transition metal dichalcogenides. Many thanks to Tim Liedl as well as his group members Tao Zhang and Robert Schreiber for introducing me to the world of DNA origami nanostructures. I also thank Efrat Lifshitz together with her group members Jenya Tilchin and Georgy Maikov for the cooperation on the spectroscopic studies of colloidal quantum dots.

I was very fortunate to closely work with Jessica Lindlau who without doubt had a major impact on me and on this thesis. I greatly benefited from your dedication and enthusiastic approach to all of our joint projects. The time we spent trying to resolve daily challenges over a cup of tea always brightened my day. I am also indebted to you for proofreading every part of this thesis. Thank you.

Thanks to Léo Colombier for his assistance with time-resolved streak camera measurements, and for being a great lab colleague and friend. Going back in time, I thank Manuel Nutz who mastered laser lithography and prepared field effect transistors based on monolayered semiconductors. Also, thanks to Dominic Berchtold who helped with the colloidal quantum dot project at an early stage.

I would also like to express my gratitude to the other members, past and present, of the nanophotonics group for the constructive atmosphere, all the fun activities outside the labs, and for making every day at work pleasant and interesting.

Many thanks to Martina Edenhofer and Bert Lorenz for their administrative assistance, and to Anton Heindl and Reinhold Rath for their technical support. I am grateful to Philipp Altpeter for the assistance in the clean room and to Stephan Manus for the help with electronics of all sorts. The fabrication of countless mechanical components in the machine shop led by Jürgen Aust and Thomas Großhauser is also much appreciated.

Furthermore, thanks go to my good friends outside the university for helping me keep things in perspective. In a final remark, I would like to especially thank my mother Valentina for her unconditional support and encouragement in all my pursuits.